Dual Neural Extended Kalman Filtering Approach for Multirate Sensor Data Fusion with Industrial Applications

by

Jingyi Wang

A thesis submitted in partial fulfillment of the requirements for the degree of

Master of Science

in

Process Control

Department of Chemical and Materials Engineering
University of Alberta

Abstract

The Kalman filter algorithm and its variants have been widely applied to the multi-sensor data fusion problems to provide joint state estimation, which is more accurate than estimations from individual sensors. The performance of the Kalman filter based fusion relies on the accuracy of the models as well as process noise statistics. Deviations from correct system models and violations of noise assumptions may lead to unsatisfied sensor fusion results and even divergence. Two types of measurements are typically utilized to estimate process quality variables. One is frequent measurements, which are available at a fast and regular sampling rate, but suffer from lower accuracy and higher measurement noises. The other type is infrequent measurements that are available at a slower sampling rate. The infrequent measurements, such as lab analysis results, have less availability but higher accuracy, and are usually used as references to improve state estimation. The objective of this thesis is to develop new multirate sensor data fusion algorithms that can compensate for model inaccuracies and violations of noise assumption to improve the online sensor fusion performance. To fulfill this objective, a dual neural extended Kalman filter (DNEKF) algorithm is proposed by employing two neural networks to improve state estimation and output predictions. Using both frequent and infrequent measurements enables the DNEKF to provide more reliable training for the neural networks and hence to provide more robust and reliable sensor fusion results.

Additionally, infrequent measurements are usually subject to irregular sampling rate and time-varying time delays. To address these problems while preserving the estimation accuracy, a fusion method that fuses frequent DNEKF estimates with

infrequent estimates from the state model compensation NEKF (SNEKF) is proposed. In this approach, frequent and infrequent estimates are fused in the fusion center when the delayed infrequent measurements arrive. The weights and biases of the state model compensation neural network (SNN) are shared between the two synchronized estimation processes.

In the primary separation cell (PSC) used for oil sands bitumen extraction, the interface level estimation is based on various sensors. Image processing based computer vision system, which uses a camera to capture sight glass vision frames, is considered to be the most accurate among these sensors. Although the accuracy of computer vision interface level estimation is high, its qualities are influenced by abnormalities, such as vision blocking, stains, and level transition between sight glasses. Under such abnormal scenarios, a sensor fusion strategy, which adaptively updates the fusion parameters, is proposed and integrated with the image processing based computer vision system.

The performance of the proposed fault-tolerant multirate sensor fusion algorithms is demonstrated using numerical examples and case studies with industrial process data. The factory acceptance test (FAT) was conducted for the sensor fusion and computer vision integrated system in the computer process control (CPC) industrial research chair (IRC) lab under industrial environmental conditions and it demonstrated the improved estimation accuracy under various process abnormalities.

Acknowledgements

First and foremost, I would like to express my sincere gratitude to my supervisor Prof. Biao Huang for his continuous guidance, inspiration, and support during my M.Sc. research period. He provided precious opportunity for me to study the research topic I am interested in, and gave me the chances to participate in practical industrial projects. These experience integrated my understating of control theory with industrial practice. Without his insightful and patient instructions, a new graduate will not be able to explore the professional and interpersonal skills to this stage. Besides the academic achievements, his enthusiasm to work, his positive attitude to life, and his concern to students are all motivate me to walk further on the research road.

It has been such a great honor to be admitted into in the University of Alberta during my undergraduate study and then join the CPC group upon graduation of the my Bachelor's degree. I received endless help and directions from the graceful, talented group members. I would like to especially thank Dr. Yousef Alipouri for giving me detailed guidance and instructions when I doing my research and industrial projects. We used to had meetings every week to talk about my progresses as well as the problems I met. I learned how to think innovatively while rigorously from working and studying with him. He offered great help when I gave presentations to the industrial partners for the first time, and when I started writing academic papers. Without his support, it would be much harder to find the orientation I would like to work on.

Additionally, I would like to thank our current and previous group members: Agustin Vicente, Rahul Raveendran, Faraz Amjad, Oguzhan Dogru for helping me

during the PSC project simulations and implementations. I much appreciate Dr. Xunyuan Yin for giving me the chance to work as his teaching assistant for the process data analysis course. During this experience, I learned how to give seminars to undergraduate students and how to provide help with the course participants. A special thank to Dr. Jayaram Valluru for discussing the future work with me and providing me with lots of motivations to keep working. I truly enjoy the friendship with the CPC group members including but not limited to: Lei Fan, Mengqi Fang, Guoyang Yan, Yanjun Ma, Ruijing Han, Hareem Shafi, Yashas Mohankumar, David Scott, Alireza Memarian. I would also like to thank my boyfriend Mingfei Pan, who is a Ph.D. student at the University of Alberta. During the past one and half years, he provided me endless concern on my life and enabled me to better focus on my academic work.

The motivation of this thesis and a significant part of this thesis come from close collaborations with our industrial partners in oil sands industry, and their helps are highly appreciated.

Last but not least, I would like to express my greatest appreciation to my mother, Jirong Cheng, who support me to study at Canada by herself for more than six years. It is her spiritually and materially support that enable me to go that far in life and in academical study. She is always the person that I most admire. She is also the motivation that inspires me to go further.

Table of Contents

1 Introduction **1**

1.1 Motivation 1

1.2 Thesis Outline and Contributions 2

2 Multirate Sensor Data Fusion based on Dual Neural Extended Kalman Filter **6**

2.1 Introduction 6

2.2 EKF based Parallel Sensor Fusion 9

2.3 Problem Statement 11

2.4 DNEKF Approach for Multirate Sensor Data Fusion 12

2.4.1 DNEKF Procedure 12

2.4.2 Model Compensation Neural Network Structure and Output Computation 18

2.5 Case Studies 20

2.5.1 Numerical Examples 20

2.5.2 PSC Interface Level Estimation 24

2.6 Conclusions 29

3 Multirate Sensor Data Fusion in Presence of Delayed Irregular Measurements using Synchronized Neural Extended Kalman Filters **31**

3.1 Introduction 31

3.2 Problem Statement 34

3.3 DNEKF and SNEKF Synchronization Approach 36
3.3.1 DNEKF and SNEKF Estimations 36
3.3.2 Fusion Procedure 41
3.4 Case Studies 45
3.4.1 Numerical Examples 46
3.4.2 SRU Product Stream Concentration Estimation 51
3.5 Conclusions 55

4 Sensor Fusion and Computer Vision Integrated System for Primary Separation Cell Interface Level Estimation 57
4.1 Introduction 57
4.2 Image Processing based Computer Vision System and Problem Statement 59
4.3 Sensor Fusion Approach 61
4.3.1 Fusion Application with Quality and Reliability Status 61
4.3.2 Sensor Fusion Integration with Computer Vision System . . . 64
4.4 Conclusion 71

5 Conclusions 74
5.1 Summary of Thesis 74
5.2 Recommendations for Future Work 75

Bibliography 77

List of Tables

2.1 Performance comparison for different fusion methods with respect to MSE values. 28

3.1 MSE from different methods for the SRU product stream concentration estimation case study. 54

4.1 Correlations between the computer vision results and estimations from sensor fusion and individual sensors. 64

List of Figures

1.1 Schematic thesis structure. 3

2.1 Sampling time strategy for frequent and infrequent measurements. 12

2.2 Graphical illustration of the DNKEF approach. 15

2.3 Sample model compensation neural network structures. 19

2.4 Model inaccuracies compensation simulation result with infrequent measurements available for every 20 frequent sampling intervals. 23

2.5 Colored noise simulation result with infrequent measurements available for every 50 frequent sampling intervals. 25

2.6 Sample cross-sectional view of PSC. 26

2.7 Fusion performance from the EKF fusion, the SNEKF fusion, and the MNEKF fusion. 28

2.8 The DNEKF fusion with infrequent measurements available for every 250, 125, and 50 frequent sampling intervals. 29

2.9 The DNEKF fusion with infrequent measurements available for every 20 frequent sampling intervals, and the weights and biases for SNN and MNN. 30

3.1 Process sampling strategy for regular frequent measurements and irregular infrequent measurements with time-varying time delays. 34

3.2 Frequent and infrequent estimations in presence of irregular and infrequent sampling rate and time-varying time delays. 36

3.3 Multirate sensor data fusion based on the DNEKF and SNEKF synchronization approach. 37

3.4 Graphical illustration of the DNKEF and SNEKF synchronization approach. 41
3.5 State propagation procedure and fusion process for the DNEKF and SNEKF synchronization approach to multirate sensor fusion in presence of delayed infrequent measurements. 43
3.6 Flow chart of the DNEKF and SNEKF synchronization approach for multirate sensor fusion in presence of irregular and infrequent sampling rate and time-varying time delays. 45
3.7 The EKF estimation results vs. the DNEKF and SNEKF synchronization fusion results for numerical example with model inaccuracies. 50
3.8 The EKF estimation results vs. the DNEKF and SNEKF synchronization fusion results for numerical example with colored noise. 52
3.9 The EKF estimation results vs. the DNEKF and SNEKF synchronization fusion results for numerical example with colored noise. 53
3.10 Frequent soft sensor measurements vs. the DNEKF and SNEKF synchronization fusion results for SRU product stream concentration estimation during period 1. 55
3.11 Frequent soft sensor measurement vs. the DNEKF and SNEKF synchronization fusion results for SRU product stream concentration estimation during period 2. 56

4.1 Sample sight glass visions of PSC. 59
4.2 Illustration of sight glass stains and operator blocking condition. . . . 60
4.3 GUI for image processing based computer vision system for interface level estimation. 61
4.4 Sample one-month computer vision results. 62
4.5 Sample 10-hour sensor fusion interface level estimation with corresponding computer vision and DP cell results. 65

4.6 Sample 10-hour sensor fusion interface level estimation with corresponding computer vision and DP cell results. 66
4.7 Sample sensor fusion and computer vision integrated system GUI. 66
4.8 The updated implementation architecture of sensor fusion and computer vision integrated system. 67
4.9 Industrial environment simulation setup in the CPC IRC lab at the University of Alberta. 68
4.10 Simulation example with sight glass blocking and transition region problems. 69
4.11 Sensor fusion and computer vision integrated system GUI displays under the low-quality (transition region) condition. 70
4.12 Sensor fusion and computer vision integrated system GUI displays under the low-reliability (operator maintenance) condition. 71
4.13 Simulation example with sight glass stains. 72
4.14 Sensor fusion and computer vision integrated system GUI displays under the low-quality (stains) condition. 73

Chapter 1

Introduction

1.1 Motivation

Multisensor data fusion techniques are widely applied in process industry to improve reliability, robustness, and integrity of quality variable estimation. The extended Kalman filter (EKF) is a commonly used technique to perform sensor fusion. However, accuracy of the EKF fusion might be degraded by low-quality state and output models. The model deficiencies need to be compensated during the online estimation processes to prevent the errors from being accumulated, leading to unsatisfactory fusion performance. Furthermore, even though the EKF algorithm handles process randomness effectively, it assumes that in its state space formulation, process states and measurements are contaminated by white noises, so that colored noises can lead to poor estimation accuracy and even divergence of the EKF estimates. Model inaccuracies and deviations from noise assumption are difficult to model. Therefore, data-driven models, such as artificial neural network, have been applied to describe complex nonlinear relationships [1]. As an example, the neural EKF (NEKF) [2] was proposed to utilize a neural network to improve the state prediction, and the neural network parameters were estimated through the EKF. However, the NEKF only compensates either state or output model deficiency but not both, and are limited to single-rate samplings.

Generally, two types of measurements are commonly utilized in industrial pro-

cesses. Frequent measurements, which are available at a fast and regular sampling rate, usually have lower accuracy and larger noise. Infrequent measurements, which are expensive and time-consuming to collect, typically have higher accuracy and smaller noise. When performing the EKF based multirate sensor fusion, effective compensation of model inaccuracies and violations of noise assumption during online implementation can help achieve more robust and reliable state estimation. Usually, the infrequent measurements are subject to irregular sampling rate and time-varying time delays, which need to be considered while performing multirate sensor fusion.

In the oil sands extraction process, the primary separation cell (PSC) is used to separate bitumen from oil sands slurry. The interface level between froth and middlings layers inside the PSC is a critical control variable related to bitumen recovery. Different types of sensors are utilized to measure this quality variable. Generally, among all the sensors, the image processing based computer vision system, which uses a camera to capture sight glass visions, is considered to be the most accurate. However, its performance highly depends on qualities of captured visions, which are easily affected by visual blocking, stains, and sight glass transition regions, etc. When computer vision results are not reliable, fusion of the measurements from other sensors can be utilized to continuously providing alternative interface level estimation.

In this thesis, model inaccuracies and violations of noise assumption are addressed for the EKF based multirate sensor data fusion. Besides, irregular sampling rate and time-varying time delays in infrequent measurements are considered. At last, a compatible and simpler version of sensor fusion approaches for image processing based computer vision system is applied for practical implementation and has successfully passed factory acceptance test.

1.2 Thesis Outline and Contributions

This thesis is devoted to providing improved multirate sensor fusion methods based on the traditional EKF algorithm combined with neural networks. The irregular

and infrequent measurements with time-varying time delays are also considered in this thesis. A sensor fusion approach, which continuously providing reliable froth-middlings interface level estimation when the computer vision system is unreliable, is proposed and implemented in industry. The overall problem objectives, current methods, proposed algorithms, and case studies are summarized in Figure 1.1.

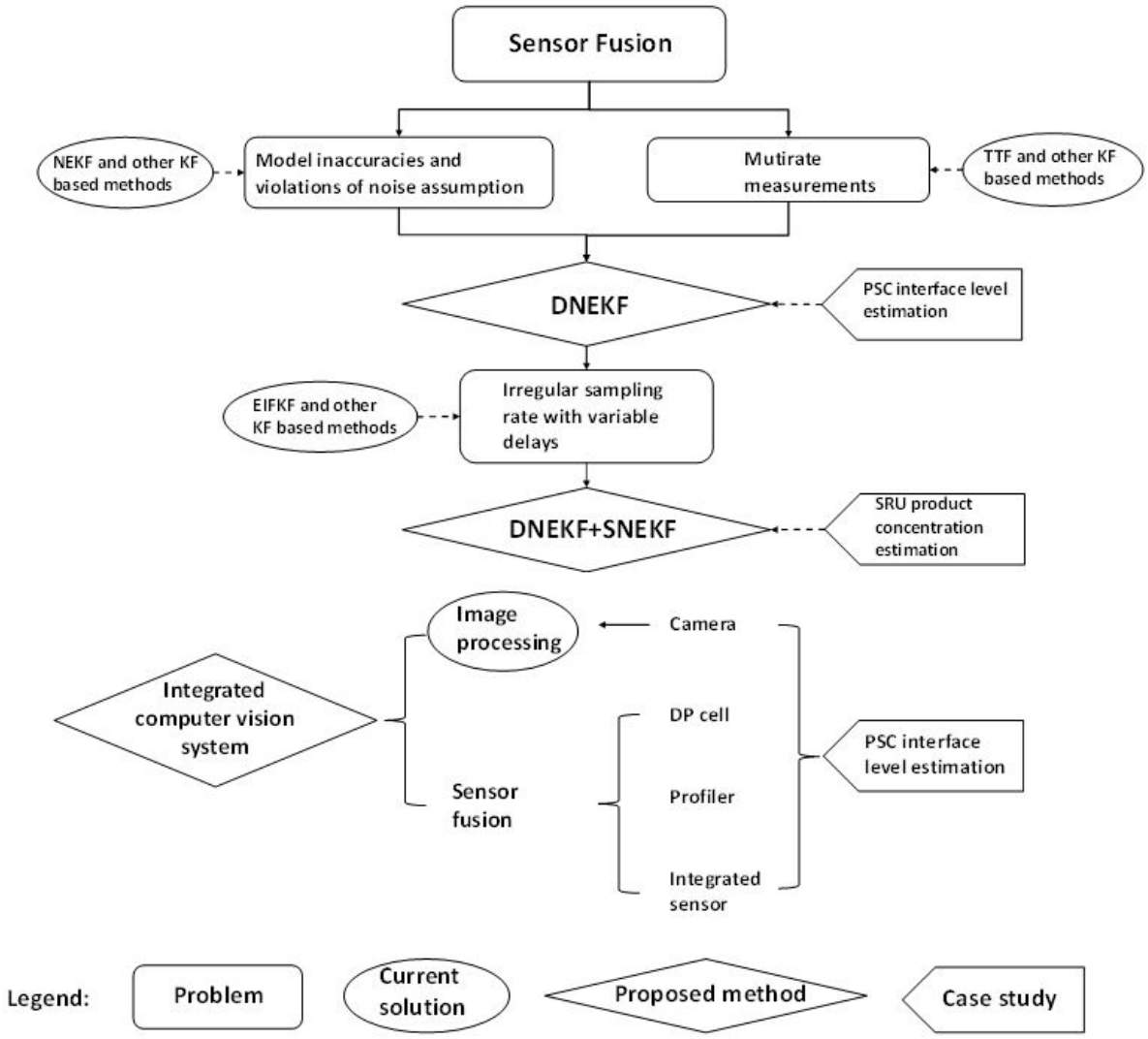

Figure 1.1: Schematic thesis structure.

In Chapter 2, the dual neural extended Kalman filter (DNKEF) algorithm is proposed. This approach employs two neural networks to enhance state estimation and output measurement predictions, and also fuses frequent and infrequent mea-

surements to improve the online sensor fusion accuracy. The two neural networks are named as state model compensation neural network (SNN) and measurement model compensation neural network (MNN), respectively. In the DNEKF, the EKF is employed to estimate process state and train neural networks simultaneously. The weights and biases of neural networks are estimated online through state vector augmentation. A multirate parameter update strategy is proposed in the DNEKF, using frequent and infrequent measurements to calibrate the weights and biases of MNN and SNN, respectively, and hence to provide more effective neural network training.

In chapter 3, based on the proposed DNEKF approach, a general situation, where the infrequent measurements are irregularly sampled and have time-varying time delays, is considered. The EKF based parallel fusion is on longer applicable in this condition due to the measurement time delays. To address the irregular sampling rate and time-varying time delays in infrequent measurements, estimations with different sampling rates are performed. Their estimates are fused in the fusion center when the infrequent measurements arrive. In this approach, regular frequent estimation and irregular infrequent estimation are proceeded synchronously using the DNEKF and the state model compensation NEKF (SNEKF), respectively. The weights and biases of SNN are shared between the two estimation processes.

In Chapter 4, an introduction to the image processing based computer vision system for PSC interface level estimation is first provided. Other available sensors, such as differential pressure (DP) cell, profiler, and an integrated sensor do not rely on sight glass visions, and their measurements can be fused to provide alternative interface level estimation. The computer vision system provides indications of reliability and quality of its estimation of the interface level. Based on the available sensors, a simplified version of sensor fusion approaches, which recursively updates the fusion parameters, is proposed and integrated with the computer vision system to improve the interface level estimation. When the computer vision results are reliable and of high-quality, the fusion parameters are recursively calibrated. If the computer vision

results are not reliable or of low-quality, instead of holding the latest estimates, the fusion parameters remain the same as the last updated values to continuously providing interface level estimation. Industrial environment simulations are conducted at the computer process control (CPC) industrial research chair (IRC) lab at the University of Alberta, demonstrating improvement of the estimation robustness and accuracy of the sensor fusion and computer vision integrated system.

Chapter 2

Multirate Sensor Data Fusion based on Dual Neural Extended Kalman Filter

2.1 Introduction

The extended Kalman filter (EKF) has been widely applied to solving multisensor data fusion problems. This algorithm uses the newly received measurements to correct last predicted states while considering process noises during online estimation [3]. In the EKF based sensor fusion process, fusion accuracy depends on the precision of state and output models that are used to describe the system dynamics. The model inaccuracies need to be compensated during online operation to prevent inaccurate fusion results [4]. Furthermore, even though the EKF algorithm handles process randomness effectively, it assumes that in its state space formulation, process states and measurements are contaminated by white noises, and violations of this assumption may cause the EKF estimates to be inaccurate or even divergent [5, 6].

To address the above problems, much work has been conducted. In [7], the Kalman filtering-based robust state estimation was proposed to deal with deterministic errors caused by sensor calibration problems, measuring instrument failures, and sensor accuracy limitations. However, this method requires to derive error models in advance, and optimal state estimates are obtained only after an iterative process. A decentral-

ized, two-layer, Kalman filter based fusion structure was designed in [8] to compensate for sensor failures. This fusion filter is tolerant to failures from some of the sensors, while resulting in a poor precision when all sensors have some types of defectiveness. Xu *et al.* [9] put forward the idea of using a first-order Gauss-Markov process to compensate for inaccurately modeled accelerations in the Kalman filter-based orbit determination. However, this method is limited to solving specific orbit determination problems. In [10], the problem of colored noise instead of white noise was considered for sensor fusion using the Kalman filter. The adaptive fuzzy logic system (AFLS) was applied to prevent Kalman filter estimates from diverging. Lee and Johnson [11] proposed using Gaussian process (GP) regression models to estimate the state of colored noise systems. The GPs learn through the output residuals between GP models and parametric models to characterize the distribution of the differences. In [12], an innovation-based adaptive estimation (IAE) method was proposed to update the noise covariance based on a remodification algorithm according to measurement reliability specifications. However, the above methods that compensate for violations of noise assumption are not applicable to solving model inaccuracy problems. Overall, these errors are difficult to capture using simple linear time-invariant models. An effective online compensation technique for model inaccuracy and violations of noise assumption is desirable to ensure the fusion results to be accurate and reliable.

In [2], a combination of the EKF algorithm and artificial neural network was proposed as the neural EKF (NEKF) technique for online model compensation and adjustment. In [13–15], the NEKFs were used for online target tracking and improving the state estimation accuracy in the feedback loop. In [16] and [17], the NEKFs were used for online sensor calibration and sensor modeling. However, the NEKF only has either state or output measurement model compensated by an artificial neural network but not both, and is divided into state model compensation NEKF (SNEKF) and measurement model compensation NEKF (MNEKF). The neural networks utilized by the NEKFs are named as state model compensation neural network (SNN) and mea-

surement model compensation neural network (MNN) accordingly. If both state and output measurement models have model-plant mismatches, the NEKF approach will be inadequate. Additionally, the above mentioned noise assumption compensation and model calibration approaches assume all sensors have the same sampling rate. In reality, infrequent measurements, such as lab analysis, are commonly employed to provide more accurate measurements for quality variables. Online measurements that are frequently sampled and inexpensive to obtain, usually lack precision. Taking advantage of both frequent and infrequent measurements can help increase fusion accuracies [18], [19].

When applying multirate sensor fusion, compensations for model deficiencies and violations of noise assumption are desirable as they achieve more robust and reliable real-time state estimation. To fulfill this objective, in this chapter, the dual NEKF (DNKEF) approach is proposed. The DNEKF uses multirate measurements to compensate for inadequate process knowledge through simultaneous state and parameter estimations. The existing NEKFs are limited to single-rate samplings and use frequent measurement residuals to train both SNN and MNN. This training approach will not be effective when the frequent measurements are inaccurate. In the DNEFK, however, a multirate parameter update strategy is proposed, where MNN is trained using frequent measurement residuals and SNN is trained according to infrequent measurements. Involving infrequent but accurate measurements enables the DNEKF to calculate differences between predicted states and reliable measurements, which in turn allows the DNEKF to provide a more effective neural network training than the NEKF algorithm. When infrequent measurements are not available, the weights and biases of SNN remain unchanged. Meanwhile, the state estimate is used as input to SNN to continuously providing compensated outputs.

The organization of this chapter is as follows. Section 2.2 introduces the EKF based parallel sensor fusion algorithm. Section 2.3 explains the problems caused by model inaccuracies and violations of noise assumption when applying the EKF based

sensor fusion. Section 2.4 provides a detail description of the DNEKF approach. In section 2.5, the DNEKF fusion technique is applied to two numerical examples as well as one industrial primary separation cell (PSC) interface level estimation problem to demonstrate its advantages over the traditional EKF based fusion and the NEKF algorithm. Finally, section 2.6 concludes this chapter.

2.2 EKF based Parallel Sensor Fusion

Measurements from different sensors can be fused in parallel using the Kalman filter algorithm by augmenting the output vector to provide fusion results for quality variables [20], [21]. Two steps are involved in the Kalman filter algorithm, namely, prediction and correction. The EKF linearizes the nonlinear models around the current state to make the linear Kalman filter applicable [22]. Consider a nonlinear process:

$$x_t = f(x_{t-1}) + w_{t-1} \tag{2.1}$$

$$y_t = h(x_t) + v_t \tag{2.2}$$

where $f(\cdot)$ and $h(\cdot)$ represent the nonlinear state and output models, x_t is state, and y_t denotes measurements from different sensors. Process and measurement noises are denoted as w_t and v_t, which are assumed to be zero-mean, uncorrelated, Gaussian white noises. Their corresponding covariance matrices are Q and R, respectively. Then the following procedures are performed according to the EKF based parallel fusion algorithm [23].

Prediction :

$$\hat{x}_t^- = f(\hat{x}_{t-1}) \tag{2.3}$$

$$P_t^- = F_{t-1} P_{t-1} F_{t-1}^T + Q \tag{2.4}$$

where $\hat{x}_{t-1}$ and $\hat{x}_t^-$ are posterior and prior estimation of the state, and P_{t-1} and P_t^- represent corrected and prior state estimation error covariance. The Jacobian

matrix, F_{t-1}, is obtained through linearization of the nonlinear state model, $f(\cdot)$, at $\hat{x}_{t-1}$, namely, $F_{t-1} = \frac{\partial f}{\partial x}|_{\hat{x}_{t-1}}$.

Correction :

In correction steps, the Kalman gain is computed as:

$$K_t = P_t^- H_t^T (H_t P_t^- H_t^T + R)^{-1} \tag{2.5}$$

where H_t is the Jacobian matrix representing linearization of nonlinear output model, $h(\cdot)$, at $\hat{x}_t^-$, and it is calculated as $H_t = \frac{\partial h}{\partial x}|_{\hat{x}_t^-}$. Then the posterior state estimation, $\hat{x}_t$, is computed as:

$$\hat{x}_t = \hat{x}_t^- + K_t(y_t - \hat{y}_t) \tag{2.6}$$

where y_t represents actual measurements, and $\hat{y}_t$ denotes model predicted output values, which can be calculated as:

$$\hat{y}_t = h(\hat{x}_t^-) \tag{2.7}$$

Then the corrected state estimation error covariance is

$$P_t = (I - K_t H_t) P_t^- \tag{2.8}$$

During multiple sensor data fusion process, each sensor has its own output measurement model. If m sensors are utilized, then m measurements are given by:

$$\begin{aligned} y_{1,t} &= h_1(x_t) + v_{1,t} \\ y_{2,t} &= h_2(x_t) + v_{2,t} \\ &\vdots \\ y_{m,t} &= h_m(x_t) + v_{m,t} \end{aligned} \tag{2.9}$$

The corresponding predictions can be obtained as:

$$\begin{aligned} \hat{y}_{1,t} &= h_1(\hat{x}_t^-) \\ \hat{y}_{2,t} &= h_2(\hat{x}_t^-) \\ &\vdots \\ \hat{y}_{m,t} &= h_m(\hat{x}_t^-) \end{aligned} \tag{2.10}$$

The Jacobian matrix, H_t, can be calculated as:

$$H_t = \begin{bmatrix} \frac{\partial h_1}{\partial x}\Big|_{\hat{x}_t^-} \\ \frac{\partial h_2}{\partial x}\Big|_{\hat{x}_t^-} \\ \vdots \\ \frac{\partial h_m}{\partial x}\Big|_{\hat{x}_t^-} \end{bmatrix} \tag{2.11}$$

Then the standard EKF procedure can be applied to perform sensor fusion through matrix augmentation [23]. Accordingly, predicted measurements, $\hat{y}_t$, and corresponding covariance matrix, R, become:

$$\hat{y}_t = \begin{bmatrix} \hat{y}_{1,t} \\ \hat{y}_{2,t} \\ \vdots \\ \hat{y}_{m,t} \end{bmatrix} \text{ and } R = \begin{bmatrix} R_1 & 0 & \dots & 0 \\ 0 & R_2 & & 0 \\ \vdots & \vdots & \ddots & \vdots \\ 0 & 0 & \dots & R_m \end{bmatrix}$$

2.3 Problem Statement

The EKF algorithm has been widely applied to finding the fusion criterion in solving multisensor data fusion problems. The inaccurate process models and noise assumptions can degrade the accuracy of the EKF estimates. Consider a nonlinear system in equation (2.1) and (2.2), with slightly different model notations:

$$x_t = f_{true}(x_{t-1}) + w_{t-1} \tag{2.12}$$

$$y_t = h_{true}(x_t) + v_t \tag{2.13}$$

where $f_{true}(\cdot)$ and $h_{true}(\cdot)$ indicate the true process state and output models. Several reasons can lead to model mismatches. First, inadequate process knowledge may cause large deviations between models and actual processes. Besides, process condition changes such as seasonal shifts can result in deviation of the current system dynamics from the previous. Moreover, the EKF algorithm is developed based on the white noise assumptions in the state space model. Colored state or measurement noise can lead to the inaccurate state estimation or even divergence [5, 6].

Typically, two types of measurements are utilized in industrial processes. Comparing with frequent measurements, infrequent measurements normally have less availability but have higher accuracy. In Figure 2.1, the small ticks represent the frequent sampling instant, t, and the squares represent the infrequent sampling instant, s. The infrequent measurement, y_i, is available at regular multiple of the frequent sampling intervals. The objective is to design an online multirate sensor data fusion algorithm

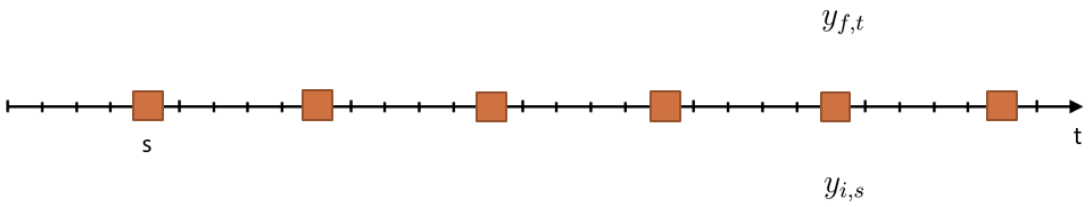

Figure 2.1: Sampling time strategy for frequent and infrequent measurements.

that is able to compensate for model inaccuracies and violations of noise assumption.

2.4 DNEKF Approach for Multirate Sensor Data Fusion

2.4.1 DNEKF Procedure

The proposed DNEKF approach is an extension of the NEKF approach and it is applied to solving multirate sensor fusion problems. The DNEKF employs both SNN and MNN simultaneously to improve state estimation and output predictions using multirate measurements. The violations of noise assumption are also handled by the DNEKF method. As mentioned in section 2.3, several reasons can lead to the inaccuracies of system models. The relations between predictions and actual values with inaccurate state and output models may be written as:

$$\begin{aligned} x_t &= f(\hat{x}_{t-1}) + d_{t-1} \\ &= \hat{x}_{d,t}^- + d_{t-1} \end{aligned} \tag{2.14}$$

$$\begin{aligned} y_t &= h(\hat{x}_t^-) + l_t \\ &= \hat{y}_{d,t} + l_t \end{aligned} \tag{2.15}$$

where $\hat{x}_{t-1}$ and $\hat{x}_t^-$ are posterior and prior state estimation from the EKF algorithm, $f(\cdot)$ and $h(\cdot)$ represent inaccurate state and output models, which result in the inaccurate predictions, $\hat{x}_{d,t}^-$ and $\hat{y}_{d,t}$, respectively. The deviations between inaccurate predictions of state and outputs and their corresponding true values, are denoted as d_t and l_t, respectively. These deviations can also include errors caused by violations of noise assumption. To compensate for the inaccuracies, neural networks, which do not require the pre-defined model structure, are utilized. The modified predictions become

$$\hat{x}_t^- = f(\hat{x}_{t-1}) + NN_x(\hat{x}_{t-1}, \hat{\phi}_{x,t-1}) \tag{2.16}$$

$$\hat{y}_t = h(\hat{x}_t^-) + NN_y(\hat{x}_t^-, \hat{\phi}_{y,t}^-) \tag{2.17}$$

where $\hat{x}_t^-$ and $\hat{y}_t$ are the modified state and output predictions. NN_x and NN_y are the outputs from SNN and MNN, with posterior state estimate, $\hat{x}_{t-1}$, and modified prior state estimate, $\hat{x}_t^-$, as their inputs, respectively. $\hat{\phi}_x$ and $\hat{\phi}_y$ are weights and biases of SNN and MNN, respectively. The relations between modified predictions and actual values are:

$$x_t = \hat{x}_t^- + \varepsilon_{t-1} \tag{2.18}$$

$$y_t = \hat{y}_t + \mu_t \tag{2.19}$$

where ε_t and μ_t are the prediction deviations after adding NN_x and NN_y compensations. Comparing with $\hat{x}_{d,t}^-$ and $\hat{y}_{d,t}$, the modified predictions, $\hat{x}_t^-$ and $\hat{y}_t$, are expected to have smaller differences from the accurate process states and measurements as they are compensated by the neural network models, namely, $\|\varepsilon_t\| \ll \|d_t\|$, $\|\mu_t\| \ll \|l_t\|$. The structure of SNN and MNN can be chosen as feed-forward neural networks with user-defined activation functions.

The DNEKF first uses a SNN to compensate for state prediction inaccuracy, then uses a MNN to improve frequent output predictions. To obtain accurate compensated

results, proper weights and biases need to be trained for the two neural networks. The DNEKF estimates process states and neural network parameters simultaneously through state vector augmentation, and updates the weights and biases for SNN and MNN through a multirate strategy. In the NEKF method, single sampling rate measurement residuals are used to provide neural network training references. However, using the frequent measurement residuals to train SNN will usually not be as reliable and accurate as that for MNN. As aforementioned, the frequent measurements are of lower accuracy and models can have significant mismatches. Reducing the frequent measurement residuals cannot ensure smaller state prediction errors. Without proper references, the parameters of SNN cannot converge to correct values, and its predictions will not be accurate. In the DNEKF approach, a multirate parameter update strategy is proposed to update ϕ_x and ϕ_y using respective measurement residuals. Frequent measurement residuals are used to train MNN parameters, while the training of SNN is according to infrequent measurements. In the DNEKF, the state vector is augmented as $\bar{x} = \begin{bmatrix} x & \phi_x & \phi_y \end{bmatrix}^T$. During online implementation, ϕ_y is updated at frequent sampling rate, while ϕ_x is updated only when the infrequent measurements arrive. In this thesis, since we are fusing multiple sensor estimations for a single quality variable, a single-dimension nonlinear state space equation with multi-dimension nonlinear output equation is considered, but the proposed algorithm can be easily extended to higher dimensional state space equations. The DNEKF procedure is illustrated in Figure 2.2.

The similar name convention as in [24, 25] is adopted in this thesis, that is, *minor instants* mean the time instants when only frequent measurements are available, and *major instants* are the time instants when both types of measurements become available. At *minor instants*, infrequent accurate measurements are unavailable. The neural network parameters, ϕ_x and ϕ_y, are treated as states to be estimated, and remain unchanged in the prediction step. Then the state and output predictions are

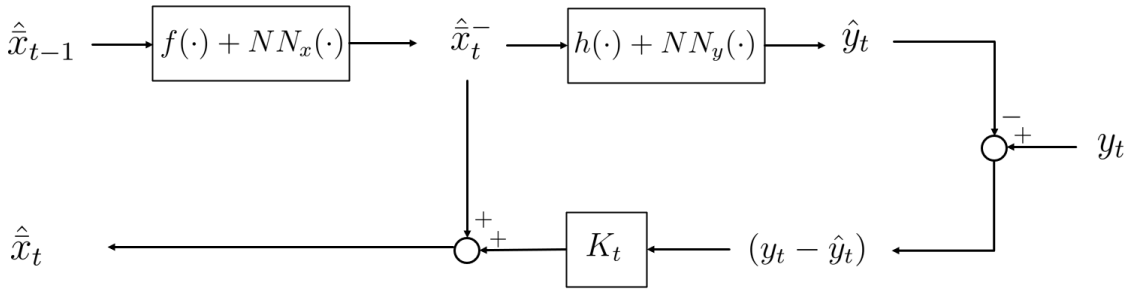

Figure 2.2: Graphical illustration of the DNKEF approach.

obtained as:

$$\hat{\bar{x}}_t^- = \begin{bmatrix} f(\hat{x}_{t-1}) + NN_x(\hat{x}_{t-1}, \hat{\phi}_{x,t-1}) \\ \hat{\phi}_{x,t-1} \\ \hat{\phi}_{y,t-1} \end{bmatrix} \tag{2.20}$$

$$\hat{y}_t = h(\hat{x}_t^-) + NN_y(\hat{x}_t^-, \hat{\phi}_{y,t}^-) \tag{2.21}$$

where $\hat{\bar{x}}_t^-$ is augmented prior state estimation. As neural network parameters are not updated in prediction, $\hat{\phi}_t^- = \hat{\phi}_{t-1}$. The predicted outputs from m frequent sensors are $\hat{y} = \begin{bmatrix} \hat{y}_{1,t} & \hat{y}_{2,t} & \dots & \hat{y}_{m,t} \end{bmatrix}^T$. The state estimation error covariance in equation (2.4) is

$$P_t^- = \bar{F}_{t-1} P_{t-1} \bar{F}_{t-1}^T + Q \tag{2.22}$$

where $\bar{F}_{t-1}$ is the augmented Jacobian matrix [26], which is calculated as:

$$\begin{aligned}
\bar{F}_{t-1} &= \begin{bmatrix} \frac{\partial(f+NN_x)}{\partial x}\Big|_{\hat{x}_{t-1}} & \frac{\partial(f+NN_x)}{\partial \phi_x}\Big|_{\hat{\phi}_{x,t-1}} & \frac{\partial(f+NN_x)}{\partial \phi_y}\Big|_{\hat{\phi}_{y,t-1}} \\ \mathbf{0} & I_{\phi_x} & \mathbf{0} \\ \mathbf{0} & \mathbf{0} & I_{\phi_y} \end{bmatrix} \\
&= \begin{bmatrix} F_{t-1} + \frac{\partial NN_x}{\partial x}\Big|_{\hat{x}_{t-1}} & \frac{\partial NN_x}{\partial \phi_x}\Big|_{\hat{\phi}_{x,t-1}} & \frac{\partial NN_x}{\partial \phi_y}\Big|_{\hat{\phi}_{y,t-1}} \\ \mathbf{0} & I_{\phi_x} & \mathbf{0} \\ \mathbf{0} & \mathbf{0} & I_{\phi_y} \end{bmatrix} \\
&= \begin{bmatrix} F_{t-1} + \frac{\partial NN_x}{\partial x}\Big|_{\hat{x}_{t-1}} & \mathbf{0} & \mathbf{0} \\ \mathbf{0} & I_{\phi_x} & \mathbf{0} \\ \mathbf{0} & \mathbf{0} & I_{\phi_y} \end{bmatrix}_{(\phi_x+\phi_y+1)\times(\phi_x+\phi_y+1)}
\end{aligned} \tag{2.23}$$

In equation (2.23), $\frac{\partial NN_x}{\partial \phi_x}\Big|_{\hat{\phi}_{x,t-1}} = \frac{\partial NN_x}{\partial \phi_y}\Big|_{\hat{\phi}_{y,t-1}} = 0$ since weights and biases of SNN and MNN are not updated when infrequent measurements are not available. Posterior state estimation, $\hat{x}_t$, is used as input to SNN to continuously modifying state predictions at *minor instants*. The Kalman gain matrix in equation (2.5) is

$$K_t = P_t^- \bar{H}_t^T (\bar{H}_t P_t^- \bar{H}_t^T + R)^{-1} \tag{2.24}$$

where the augmented Jacobian matrix, $\bar{H}_t$, is

$$\begin{aligned}
\bar{H}_t &= \begin{bmatrix} \frac{\partial(h+NN_y)}{\partial x}\Big|_{\hat{x}_t^-} & \frac{\partial(h+NN_y)}{\partial \phi_x}\Big|_{\hat{\phi}_{x,t}^-} & \frac{\partial(h+NN_y)}{\partial \phi_y}\Big|_{\hat{\phi}_{y,t}^-} \end{bmatrix} \\
&= \begin{bmatrix} H_t + \frac{\partial NN_y}{\partial x}\Big|_{\hat{x}_t^-} & \frac{\partial NN_y}{\partial \phi_x}\Big|_{\hat{\phi}_{x,t}^-} & \frac{\partial NN_y}{\partial \phi_y}\Big|_{\hat{\phi}_{y,t}^-} \end{bmatrix} \\
&= \begin{bmatrix} H_t + \frac{\partial NN_y}{\partial x}\Big|_{\hat{x}_t^-} & \mathbf{0} & \frac{\partial NN_y}{\partial \phi_y}\Big|_{\hat{\phi}_{y,t}^-} \end{bmatrix}_{m\times(\phi_x+\phi_y+1)}
\end{aligned} \tag{2.25}$$

In equation (2.25), the derivative of NN_y with respect to the weights and biases of SNN can be computed as:

$$\begin{aligned}
\frac{\partial NN_y}{\partial \phi_x} &= \frac{\partial NN_y}{\partial \hat{x}_t^-} \frac{\partial \hat{x}_t^-}{\partial \phi_x} \\
&= \frac{\partial NN_y}{\partial \hat{x}_t^-} \frac{\partial (f(\hat{x}_{t-1}) + NN_x)}{\partial \phi_x} \\
&= \frac{\partial NN_y}{\partial \hat{x}_t^-} \frac{\partial NN_x}{\partial \phi_x}
\end{aligned}$$

In correction step, state estimation and estimation error covariance are updated using following equations:

$$\hat{\bar{x}}_t = \hat{\bar{x}}_t^- + K_t(y_t - \hat{y}_t) \tag{2.26}$$

$$P_t = (I - K_t \bar{H}_t) P_t^- \tag{2.27}$$

where measurement residual, $y_t - \hat{y}_t$, is

$$y_t - \hat{y}_t = \begin{bmatrix} y_{1,t} - \hat{y}_{1,t} \\ y_{2,t} - \hat{y}_{2,t} \\ \vdots \\ y_{m,t} - \hat{y}_{m,t} \end{bmatrix} = \begin{bmatrix} y_{1,t} & -\Big(h_1(\hat{x}_t^-) + NN_{y,1}(\hat{x}_t^-, \hat{\phi}_{y,t}^-)\Big) \\ y_{2,t} & -\Big(h_2(\hat{x}_t^-) + NN_{y,2}(\hat{x}_t^-, \hat{\phi}_{y,t}^-)\Big) \\ \vdots & \\ y_{m,t} & -\Big(h_m(\hat{x}_t^-) + NN_{y,m}(\hat{x}_t^-, \hat{\phi}_{y,t}^-)\Big) \end{bmatrix} \tag{2.28}$$

At *major instants*, infrequent but accurate measurements are available, and the DNEKF steps are the same as those at *minor instants*. However, dimensions and elements for some matrices are different. The state prediction equation is the same as equation (2.20). While with availability of infrequent measurements, the output predictions are further augmented as:

$$\begin{aligned} \hat{y}_{1,t} &= h_1(\hat{x}_t^-) + NN_{y,1}(\hat{x}_t^-, \hat{\phi}_{y,t}^-) \\ \hat{y}_{2,t} &= h_2(\hat{x}_t^-) + NN_{y,2}(\hat{x}_t^-, \hat{\phi}_{y,t}^-) \\ &\vdots \\ \hat{y}_{m,t} &= h_m(\hat{x}_t^-) + NN_{y,m}(\hat{x}_t^-, \hat{\phi}_{y,t}^-) \\ \hat{y}_{i,s} &= h_i(\hat{x}_s^-) \end{aligned} \tag{2.29}$$

where $\hat{y}_i$ is infrequent measurement, and since it is considered as accurate measurement, $h_i(\hat{x}_s^-) = \hat{x}_s^-$. The Jacobian matrix, $\bar{F}_{t-1}$, in equation (2.22) becomes

$$\bar{F}_{t-1} = \begin{bmatrix} F_{t-1} + \frac{\partial NN_x}{\partial x}\Big|_{\hat{x}_{t-1}} & \frac{\partial NN_x}{\partial \phi_x}\Big|_{\hat{\phi}_{x,t-1}} & \mathbf{0} \\ \mathbf{0} & I_{\phi_x} & \mathbf{0} \\ \mathbf{0} & \mathbf{0} & I_{\phi_y} \end{bmatrix}_{(\phi_x+\phi_y+1)\times(\phi_x+\phi_y+1)} \tag{2.30}$$

Furthermore, the Jacobian matrix, $\bar{H}_t$, in equation (2.24) is

$$\begin{aligned}\bar{H}_t &= \begin{bmatrix} \frac{\partial(h+NN_y)}{\partial x}\Big|_{\hat{x}_t^-} & \frac{\partial(h+NN_y)}{\partial \phi_x}\Big|_{\hat{\phi}_{x,t}^-} & \frac{\partial(h+NN_y)}{\partial \phi_y}\Big|_{\hat{\phi}_{y,t}^-} \\ 1 & \mathbf{0} & \mathbf{0} \end{bmatrix} \\ &= \begin{bmatrix} H_t + \frac{\partial NN_y}{\partial x}\Big|_{\hat{x}_t^-} & \frac{\partial NN_y}{\partial \phi_x}\Big|_{\hat{\phi}_{x,t}^-} & \frac{\partial NN_y}{\partial \phi_y}\Big|_{\hat{\phi}_{y,t}^-} \\ 1 & \mathbf{0} & \mathbf{0} \end{bmatrix}_{(m+1)\times(\phi_x+\phi_y+1)}\end{aligned} \tag{2.31}$$

The last row of $\bar{H}_t$ in equation (2.31) corresponds to infrequent but accurate measurements. In correction step, the measurement residual is augmented into:

$$y_t - \hat{y}_t = \begin{bmatrix} y_{1,t} - \hat{y}_{1,t} \\ y_{2,t} - \hat{y}_{2,t} \\ \vdots \\ y_{m,t} - \hat{y}_{m,t} \\ y_{i,s} - \hat{x}_s^- \end{bmatrix} \tag{2.32}$$

where $\hat{x}_s^- = f(\hat{x}_{s-1}) + NN_x(\hat{x}_{s-1}, \hat{\phi}_{x,s-1})$ at *major instants*. The differences between the accurate measurements, $y_{i,s}$, and the model predicted states, $f(\hat{x}_{s-1})$, provide the more accurate references for NN_x, and hence SNN can be trained effectively using infrequent measurements in the DNEKF procedure.

2.4.2 Model Compensation Neural Network Structure and Output Computation

Compensation neural networks can be selected as single-hidden-layer, feed-forward neural networks. Sample neural network structures for SNN and MNN are illustrated in Figure 2.3 for a single quality variable with m sensors. Assign n_x and n_y hidden nodes in the hidden layers of SNN and MNN, respectively. The input to SNN is the posterior state estimation from the last step, and input to MNN is the modified prior state estimation at current step. Choosing *tanh* as the activation function of each node, then SNN output value, NN_x, can be calculated as [27]:

$$NN_x = tanh\left(w_x^{(3)T} \cdot tanh\left(w_x^{(2)} \cdot \hat{x}_t + b_x^{(2)}\right) + b_x^{(3)}\right) \tag{2.33}$$

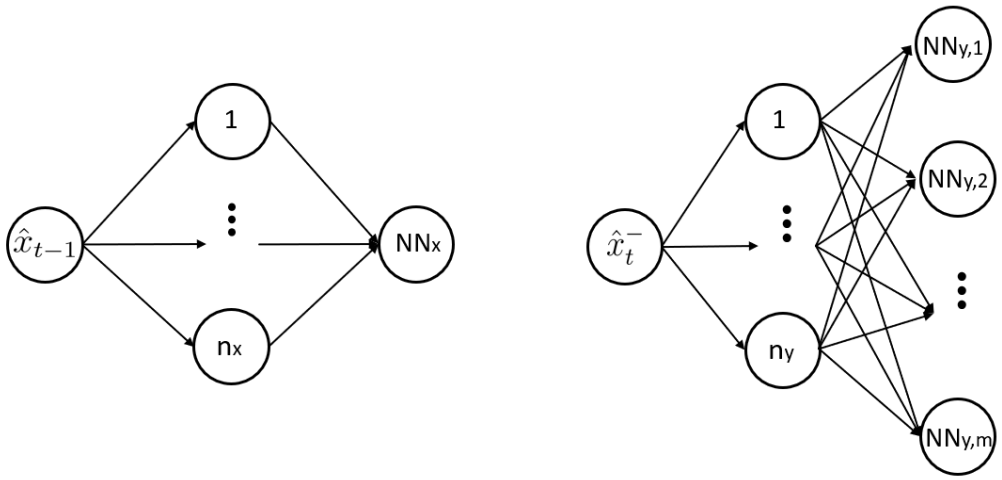

$$\hat{x}_t^- = f(\hat{x}_{t-1}) + NN_x(\hat{x}_{t-1}, \hat{\phi}_{x,t-1}) \qquad \hat{y}_t = h(\hat{x}_t^-) + NN_y(\hat{x}_t^-, \hat{\phi}_{y,t}^-)$$

Figure 2.3: Sample model compensation neural network structures.

where

$$w_x^{(2)} = \begin{bmatrix} w_{1,1}^{(2)} \\ w_{2,1}^{(2)} \\ \vdots \\ w_{n_x,1}^{(2)} \end{bmatrix} b_x^{(2)} = \begin{bmatrix} b_1^{(2)} \\ b_2^{(2)} \\ \vdots \\ b_{n_x}^{(2)} \end{bmatrix} w_x^{(3)} = \begin{bmatrix} w_{1,1}^{(3)} \\ w_{1,2}^{(3)} \\ \vdots \\ w_{1,n_x}^{(3)} \end{bmatrix}, b_x^{(3)} = \begin{bmatrix} b_1^{(3)} \end{bmatrix}$$

The superscript of weights, w, represents the destination layer number. The first number of subscript represents the destination neuron number, while the second number of subscript indicates the departure neural number [28]. As an example, $w_{1,2}^{(3)}$ means this weight is from the second neuron of the second layer towards the first neuron of the third layer. The superscript of biases, b, represents its location layer, and the subscript indicates the number of neuron where this bias locates. For example, $b_n^{(2)}$ is the bias of the n^{th} neuron in the second layer. Similarly, NN_y can be written as:

$$NN_y = tanh\left(\begin{bmatrix} w_{1,1}^{(3)} & \cdots & w_{1,n_y}^{(3)} \\ w_{2,1}^{(3)} & \cdots & w_{2,n_y}^{(3)} \\ \vdots & \ddots & \vdots \\ w_{m,1}^{(3)} & \cdots & w_{m,n_y}^{(3)} \end{bmatrix} \cdot tanh\left(w_y^{(2)} \cdot \hat{x}_t^- + b_y^{(2)}\right) + b_y^{(3)}\right) \tag{2.34}$$

Under the same conventional notation, $w_y^{(2)}$, $b_y^{(2)}$, $w_y^{(3)}$, and $b_y^{(3)}$ in equation (2.34) are

$$w_y^{(2)} = \begin{bmatrix} w_{1,1}^{(2)} \\ w_{2,1}^{(2)} \\ \vdots \\ w_{n_y,1}^{(2)} \end{bmatrix} \; b_y^{(2)} = \begin{bmatrix} b_1^{(2)} \\ b_2^{(2)} \\ \vdots \\ b_{n_y}^{(2)} \end{bmatrix} \; w_y^{(3)} = \begin{bmatrix} w_{1,1}^{(3)} \\ \vdots \\ w_{1,n_y}^{(3)} \\ \vdots \\ w_{m,1}^{(3)} \\ \vdots \\ w_{m,n_y}^{(3)} \end{bmatrix} \; b_y^{(3)} = \begin{bmatrix} b_1^{(3)} \\ b_2^{(3)} \\ \vdots \\ b_m^{(3)} \end{bmatrix}$$

During the DNEKF fusion process, the state prediction is first improved by NN_x, and the modified state estimation is input to the output model as well as the MNN. Then NN_y compensates for frequent output measurement predictions. The weights and biases of neural networks are updated through a multirate strategy in correction steps of the DNEKF.

2.5 Case Studies

In this section, the proposed DNEKF approach is evaluated through two numerical examples and one industrial case study. In the first numerical example, both state and output models are inaccurate and are compensated using the DNEKF approach. In the second numerical example, colored process and measurements noises are adopted to check compensation capacity of the proposed method. In the industrial case study, linear time-invariant models are utilized, and the DNEKF approach is applied for online model inaccuracy compensation.

2.5.1 Numerical Examples

2.5.1.1 Model Inaccuracies Compensation

The key objective of the DNEKF approach is to compensate for model inaccuracies. In this example, accurate models are unknown, and defective models are utilized for predictions to test model inaccuracy compensation ability of the DNEKF. The true

state and output models are given as follows:

$$\begin{aligned} x_t &= f_{true}(x_{t-1}) + w_{t-1} \\ &= 3sin^2(x_{t-1}) - 5cos(x_{t-1}) + w_{t-1} \end{aligned} \tag{2.35}$$

and

$$\begin{aligned} y_t &= h_{true}(x_t) + v_t \\ &= \begin{bmatrix} x_t^2 + v_{1,t} \\ 3cos(x_t) + v_{2,t} \end{bmatrix} \end{aligned} \tag{2.36}$$

where $w \sim N(0, 1 \times 10^{-4})$, and $v \sim N(0, R)$ with $R = diag\left\{4 \times 10^{-4}, 4 \times 10^{-4}\right\}$. The inaccurate state and output models are

$$\begin{aligned} \hat{x}_t^- &= f(\hat{x}_{t-1}) \\ &= 2sin^2(\hat{x}_{t-1}) - 3cos(\hat{x}_{t-1}) \end{aligned} \tag{2.37}$$

and

$$\begin{aligned} \hat{y}_t &= h(\hat{x}_t^-) \\ &= \begin{bmatrix} 2\hat{x}_t^- \\ 5cos(\hat{x}_t^-) \end{bmatrix} \end{aligned} \tag{2.38}$$

Applying DNEKF algorithm, the state predictions are

$$\hat{\bar{x}}_t^- = \begin{bmatrix} 2sin^2(\hat{x}_{t-1}) - 3cos(\hat{x}_{t-1}) + NN_x(\hat{x}_{t-1}, \hat{\phi}_{x,t-1}) \\ \hat{\phi}_{x,t-1} \\ \hat{\phi}_{y,t-1} \end{bmatrix} \tag{2.39}$$

The output predictions are

$$\hat{y}_t = \begin{bmatrix} 2\hat{x}_t^- + NN_{y,1}(\hat{x}_t^-, \hat{\phi}_{y,t}^-) \\ 5cos(\hat{x}_t^-) + NN_{y,2}(\hat{x}_t^-, \hat{\phi}_{y,t}^-) \end{bmatrix} \tag{2.40}$$

In this case study, *tanh* is used as activation function. Since single-hidden-layer neural network is utilized for both SNN and MNN, 1-3-1 and 1-3-2 are selected as neural network structures. The number of elements of ϕ_x and ϕ_y are 10 and 14, respectively. Then total number of elements of augmented state vector, $\bar{x}$, is 25. During fusion process, NN_x and NN_y can be evaluated as:

$$NN_x = tanh\left(w_x^{(3)T} \cdot tanh\left(w_x^{(2)} \cdot \hat{x}_t + b_x^{(2)}\right) + b_x^{(3)}\right) \tag{2.41}$$

$$NN_y = tanh\left(\begin{bmatrix} w_{1,1}^{(3)} & w_{1,2}^{(3)} & w_{1,3}^{(3)} \\ w_{2,1}^{(3)} & w_{2,2}^{(3)} & w_{2,3}^{(3)} \end{bmatrix} \cdot tanh\left(w_y^{(2)} \cdot \hat{x}_t^- + b_y^{(2)}\right) + b_y^{(3)}\right) \tag{2.42}$$

At *major instants*, the Jacobian matrices, $\bar{F}_{t-1}$ and $\bar{H}_t$, are

$$\bar{F}_{t-1} = \begin{bmatrix} 4sin(\hat{x}_{t-1})cos(\hat{x}_{t-1}) + 3sin(\hat{x}_{t-1}) + \frac{\partial NN_x}{\partial x}\Big|_{\hat{x}_{t-1}} & \frac{\partial NN_x}{\partial \phi_x}\Big|_{\hat{\phi}_{x,t-1}} & \mathbf{0} \\ \mathbf{0} & I_{\phi_x} & \mathbf{0} \\ \mathbf{0} & \mathbf{0} & I_{\phi_y} \end{bmatrix}_{25\times 25} \tag{2.43}$$

and

$$\bar{H}_t = \begin{bmatrix} 2 + \frac{\partial NN_{y,1}}{\partial x}\Big|_{\hat{x}_t^-} & \frac{\partial NN_{y,1}}{\partial \phi_x}\Big|_{\hat{\phi}_{x,t}^-} & \frac{\partial NN_{y,1}}{\partial \phi_y}\Big|_{\hat{\phi}_{y,t}^-} \\ -5sin(\hat{x}_t^-) + \frac{\partial NN_{y,2}}{\partial x}\Big|_{\hat{x}_t^-} & \frac{\partial NN_{y,2}}{\partial \phi_x}\Big|_{\hat{\phi}_{x,t}^-} & \frac{\partial NN_{y,2}}{\partial \phi_y}\Big|_{\hat{\phi}_{y,t}^-} \\ 1 & \mathbf{0} & \mathbf{0} \end{bmatrix}_{3\times 25} \tag{2.44}$$

The measurement noise covariance matrix, $R = diag\left\{4\times 10^{-4}, 4\times 10^{-4}, 1\times 10^{-4}\right\}$. At *minor instants*, only frequent measurements are available, and the corresponding Jacobian matrices are

$$\bar{F}_{t-1} = \begin{bmatrix} 4sin(\hat{x}_{t-1})cos(\hat{x}_{t-1}) + 3sin(\hat{x}_{t-1}) + \frac{\partial NN_x}{\partial x}\Big|_{\hat{x}_{t-1}} & \mathbf{0} & \mathbf{0} \\ \mathbf{0} & I_{\phi_x} & \mathbf{0} \\ \mathbf{0} & \mathbf{0} & I_{\phi_y} \end{bmatrix}_{25\times 25} \tag{2.45}$$

and

$$\bar{H}_t = \begin{bmatrix} 2 + \frac{\partial NN_{y,1}}{\partial x}\Big|_{\hat{x}_t^-} & \mathbf{0} & \frac{\partial NN_{y,1}}{\partial \phi_y}\Big|_{\hat{\phi}_{y,t}^-} \\ -5sin(\hat{x}_t^-) + \frac{\partial NN_{y,2}}{\partial x}\Big|_{\hat{x}_t^-} & \mathbf{0} & \frac{\partial NN_{y,2}}{\partial \phi_y}\Big|_{\hat{\phi}_{y,t}^-} \end{bmatrix}_{2\times 25} \tag{2.46}$$

Assuming infrequent accurate measurements are available for every 20 frequent sampling intervals, the simulation results are shown in Figure 2.4. For comparison, mean squared error (MSE) is used, which is defined as:

$$MSE = \frac{1}{n}\sum_{t=1}^{n}\left(x_t - \hat{x}_t\right)^2 \tag{2.47}$$

where n is number of frequent samples. With compensation of both state and output models, the MSE is calculated as 4.8580 from DNEKF, which is smaller than 12.0226 from standard EKF fusion, hence fusion accuracy is improved.

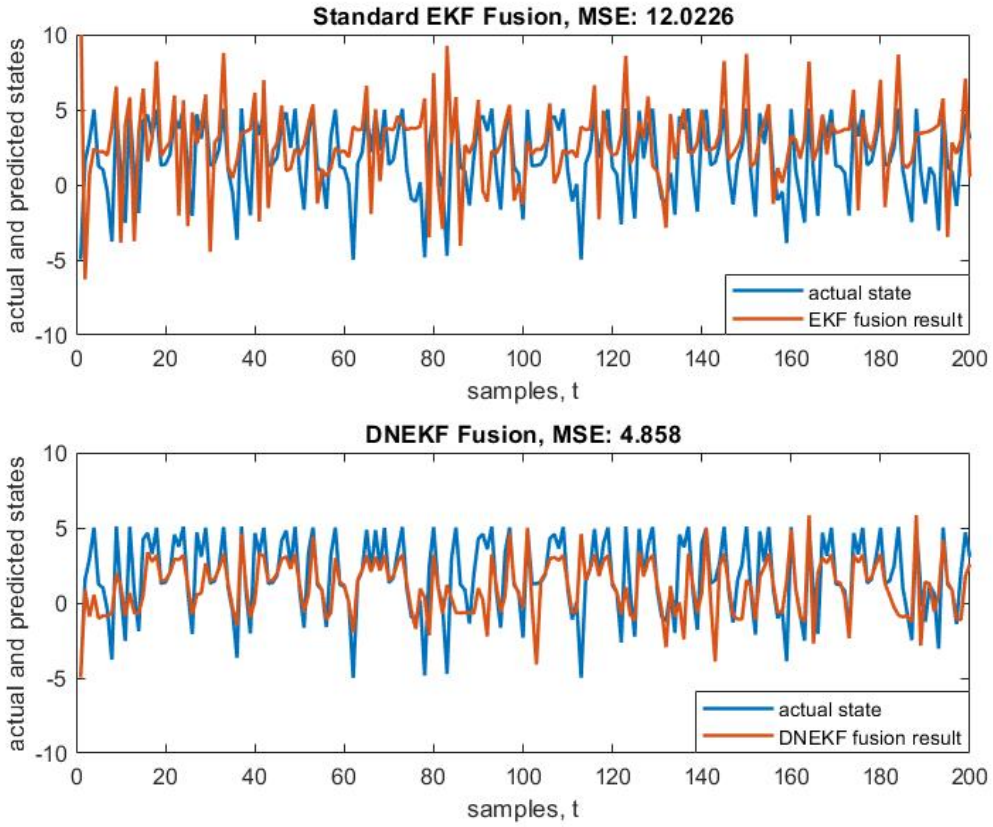

Figure 2.4: Model inaccuracies compensation simulation result with infrequent measurements available for every 20 frequent sampling intervals.

2.5.1.2 Colored Noises Compensation

In this example, the actual models are available and colored noise are applied to both process state and measurements, but white noises are assumed in the nominal models. Red noise, which has zero mean, constant variance, and is correlated along time is generated for simulation using the following equations [29]:

$$\begin{aligned} p_1 &= w_1 \\ p_t &= rp_{t-1} + (1-r^2)^{1/2} w_t \end{aligned} \tag{2.48}$$

where w_t is Gaussian white noise, and r is the correlation between red noise, p_{t+1} and p_t, and $r = 0.6$ in this simulation. The state and output predictions are

$$\hat{\hat{x}}_t^- = \begin{bmatrix} 3sin^2(\hat{x}_{t-1}) - 5cos(\hat{x}_{t-1}) + NN_x(\hat{x}_{t-1}, \hat{\phi}_{x,t-1}) \\ \hat{\phi}_{x,t-1} \\ \hat{\phi}_{y,t-1} \end{bmatrix} \tag{2.49}$$

and

$$\hat{y}_t = \begin{bmatrix} \hat{x}_t^{2-} + NN_{y,1}(\hat{x}_t^-, \hat{\phi}_{y,t}^-) \\ 3cos(\hat{x}_t^-) + NN_{y,2}(\hat{x}_t^-, \hat{\phi}_{y,t}^-) \end{bmatrix} \tag{2.50}$$

In this example, infrequent accurate measurements are available for every 50 frequent sampling intervals. The simulation results are shown in Figure 2.5. The MSE from the DNEKF is calculated as 2.5768 comparing with 30.6740 from the standard EKF fusion, indicating that even if accurate models are available, violations of noise assumption will also decrease the EKF fusion performance. The DNEKF approach is able to compensate for violations of noise assumption and provide more accurate state estimation than the tradition EKF fusion.

2.5.2 PSC Interface Level Estimation

Primary Separation Cell (PSC) is used to separate bitumen from oil sands slurry through a water-based gravity separation process [30]. The typical cross-section view of PSC is shown in Figure 2.6. The oil sands slurry in PSC is divided into three layers: the froth layer, middlings layer, and tailings layer. The exact location of froth-middlings interface is critical to bitumen recovery rate control [31]. The common measurement instruments of interface level are nuclear density profiler, differential pressure (DP) cell, and an integrated sensor with same sampling rate as others. A less common applied technique is the image processing based computer vision system, which relies on a camera mounted on the PSC sight glasses to provide vision frames to estimate the interface level [32], [33]. Owing to its increasing accuracy and decreasing cost, computer vision that utilizes image processing technique is becoming

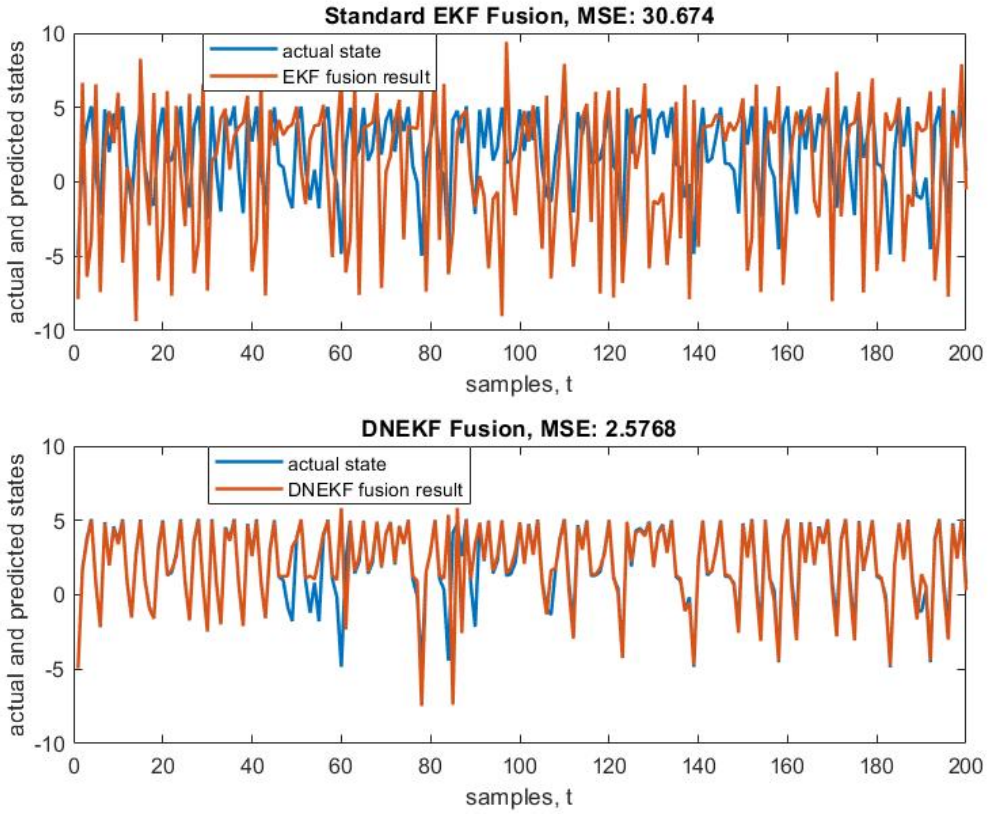

Figure 2.5: Colored noise simulation result with infrequent measurements available for every 50 frequent sampling intervals.

more popular. In this case study, all the industrial data has been normalized for proprietary reason. The DP cell, integrated sensor, and profiler measurements are considered as frequent but less accurate measurements, and computer vision results are treated as infrequent accurate measurements since in reality, image processing calculation may not be able to perform normally for various reasons [33]. The DNEKF multirate sensor data fusion approach is applied to the PSC system to provide a more precise estimation of the froth-middlings interface level. The estimation performance is compared with the EKF, the SNEKF, and the MNEKF fusion results to show the improvements. In this case study, 1-3-1 and 1-4-3 structures are utilized for SNN and MNN, respectively.

Linear time-invariant state and output models are used to describe the process.

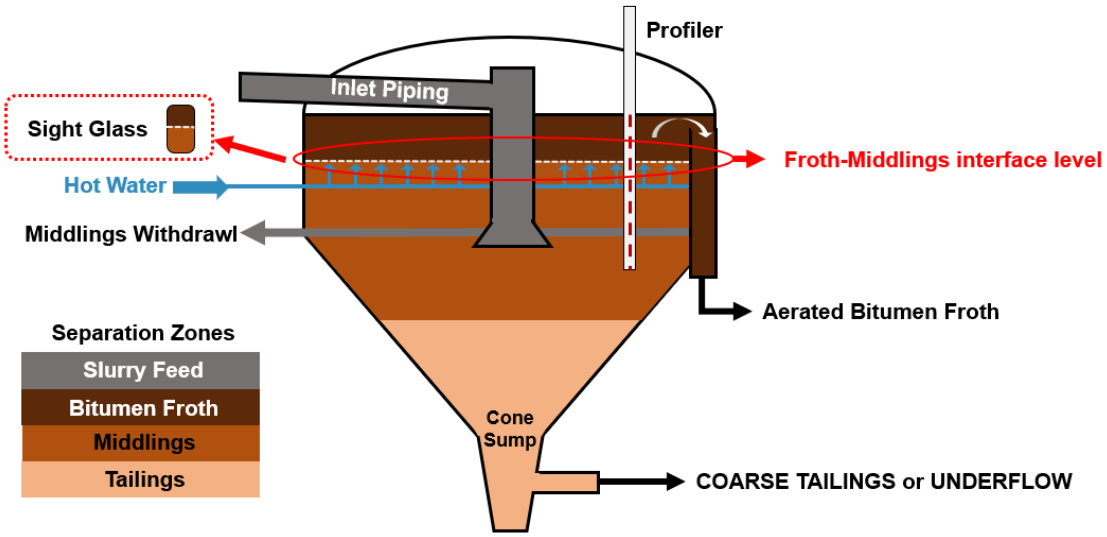

Figure 2.6: Sample cross-sectional view of PSC.

Then state and output predictions are written as:

$$\hat{\bar{x}}_t^- = \begin{bmatrix} F \cdot \hat{x}_{t-1} + NN_x(\hat{x}_{t-1}, \hat{\phi}_{x,t-1}) \\ \hat{\phi}_{x,t-1} \\ \hat{\phi}_{y,t-1} \end{bmatrix} \tag{2.51}$$

and

$$\hat{y}_t = H \cdot \hat{x}_t^- + NN_y(\hat{x}_t^-, \hat{\phi}_{y,t}^-) \tag{2.52}$$

where $x(\%)$ is the froth-middlings interface level. The number of elements of ϕ_x is 10 and that of ϕ_y is 23. After adding one state, total elements of $\bar{x}$ is 34. The initial values of ϕ_x and ϕ_y are random numbers that are close to zero. The output model is

$$H = \begin{cases} \begin{bmatrix} H_{DPcell} & H_{integrated\ sensor} & H_{profiler} & H_{camera} \end{bmatrix}^T, & \text{major instants} \\ \begin{bmatrix} H_{DPcell} & H_{integrated\ sensor} & H_{profiler} \end{bmatrix}^T, & \text{minor instants} \end{cases}$$

where $H_{camera} = 1$. The corresponding measurement noise covariance matrix is

$$R = \begin{cases} diag\left\{ R_{DPcell}, R_{integrated\ sensor}, R_{profiler}, R_{camera} \right\}, & \text{major instants} \\ diag\left\{ R_{DPcell}, R_{integrated\ sensor}, R_{profiler} \right\}, & \text{minor instants} \end{cases}$$

At *major instants*, the Jacobian matrices, $\bar{F}_{t-1}$ and $\bar{H}_t$, are

$$\bar{F}_{t-1} = \begin{bmatrix} F + \frac{\partial NN_x}{\partial x}\Big|_{\hat{x}_{t-1}} & \frac{\partial NN_x}{\partial \phi_x}\Big|_{\hat{\phi}_{x,t-1}} & \mathbf{0} \\ \mathbf{0} & I_{\phi_x} & \mathbf{0} \\ \mathbf{0} & \mathbf{0} & I_{\phi_y} \end{bmatrix}_{34\times 34} \tag{2.53}$$

and

$$\bar{H}_t = \begin{bmatrix} H + \frac{\partial (NN_y)}{\partial x}\Big|_{\hat{x}_t^-} & \frac{\partial (NN_y)}{\partial \phi_x}\Big|_{\hat{\phi}_{x,t}^-} & \frac{\partial (NN_y)}{\partial \phi_y}\Big|_{\hat{\phi}_{y,t}^-} \\ 1 & \mathbf{0} & \mathbf{0} \end{bmatrix}_{4\times 34} \tag{2.54}$$

At *minor instants*, the Jacobian matrices become

$$\bar{F}_{t-1} = \begin{bmatrix} F + \frac{\partial NN_x}{\partial x}\Big|_{\hat{x}_{t-1}} & \mathbf{0} & \mathbf{0} \\ \mathbf{0} & I_{\phi_x} & \mathbf{0} \\ \mathbf{0} & \mathbf{0} & I_{\phi_y} \end{bmatrix}_{34\times 34} \tag{2.55}$$

and

$$\bar{H}_t = \begin{bmatrix} H + \frac{\partial (NN_y)}{\partial x}\Big|_{\hat{x}_t^-} & \mathbf{0} & \frac{\partial (NN_y)}{\partial \phi_y}\Big|_{\hat{\phi}_{y,t}^-} \end{bmatrix}_{3\times 34} \tag{2.56}$$

Figure 2.7 shows fusion performance of the standard EKF, the SNEKF, and the MNEKF algorithms in terms of MSE. For the SNEKF, as aforementioned, without a reliable reference, SNN training is not reliable, hence NN_x of the SNEKF is not able to improve the fusion performance. The MSE for the SNEKF fusion is higher than that of the EKF fusion. For the MNEKF, as training process is more reliable, fusion accuracy is improved from the EKF method.

Figure 2.8 shows fusion performance for the DNEKF algorithm with different infrequent measurement sampling rates. From top to bottom, infrequent sampling intervals are 250, 125, and 50 frequent sampling intervals. With increased availability of infrequent reference measurements, the DNKEF fusion performance becomes better. The MSE values for different methods are presented in Table 2.1.

Figure 2.9 shows results for the DNKEF fusion with infrequent measurements available for every 20 frequent sampling intervals as well as the weights and biases

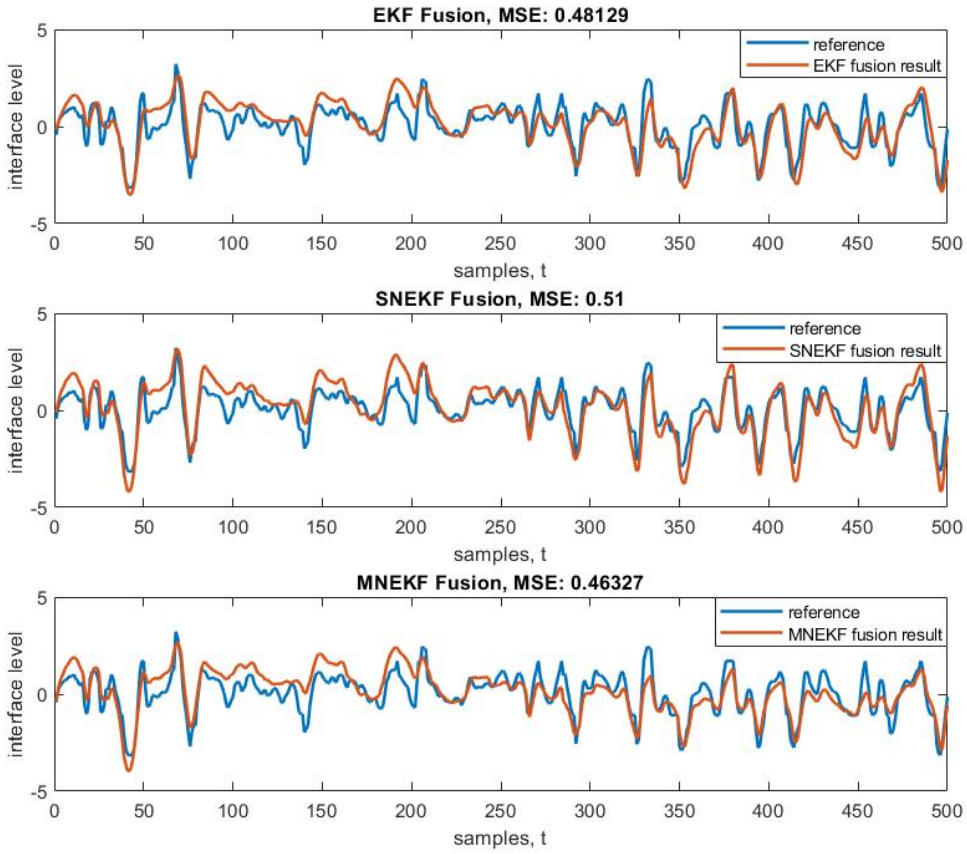

Figure 2.7: Fusion performance from the EKF fusion, the SNEKF fusion, and the MNEKF fusion.

Table 2.1: Performance comparison for different fusion methods with respect to MSE values.

Fusion methods	**Infrequent sampling intervals**	**MSE**
EKF	N/A	0.48129
SNEKF	N/A	0.51000
MNEKF	N/A	0.46327
DNEKF	250	0.42302
	125	0.37454
	50	0.34494

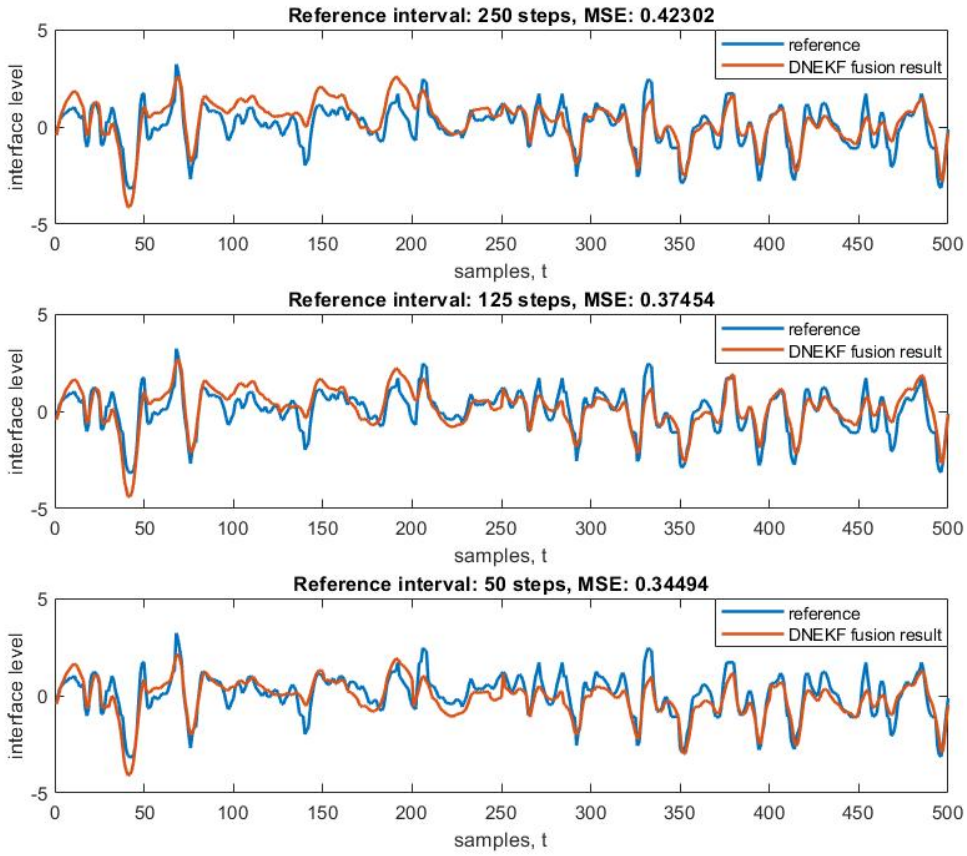

Figure 2.8: The DNEKF fusion with infrequent measurements available for every 250, 125, and 50 frequent sampling intervals.

for SNN and MNN. As can be seen from the middle subplot, the weights and biases for SNN change every 20 frequent sampling intervals with accurate computer vision results availability. As shown in the bottom subplot, the weights and biases for MNN change at frequent sampling rate.

2.6 Conclusions

In this chapter, the DNEKF approach for multirate sensor data fusion is proposed. The DNEKF estimates process states and neural network parameters simultaneously through state vector augmentation. While compensating for inadequate process knowledge, the DNEKF takes advantage of both frequent and infrequent measure-

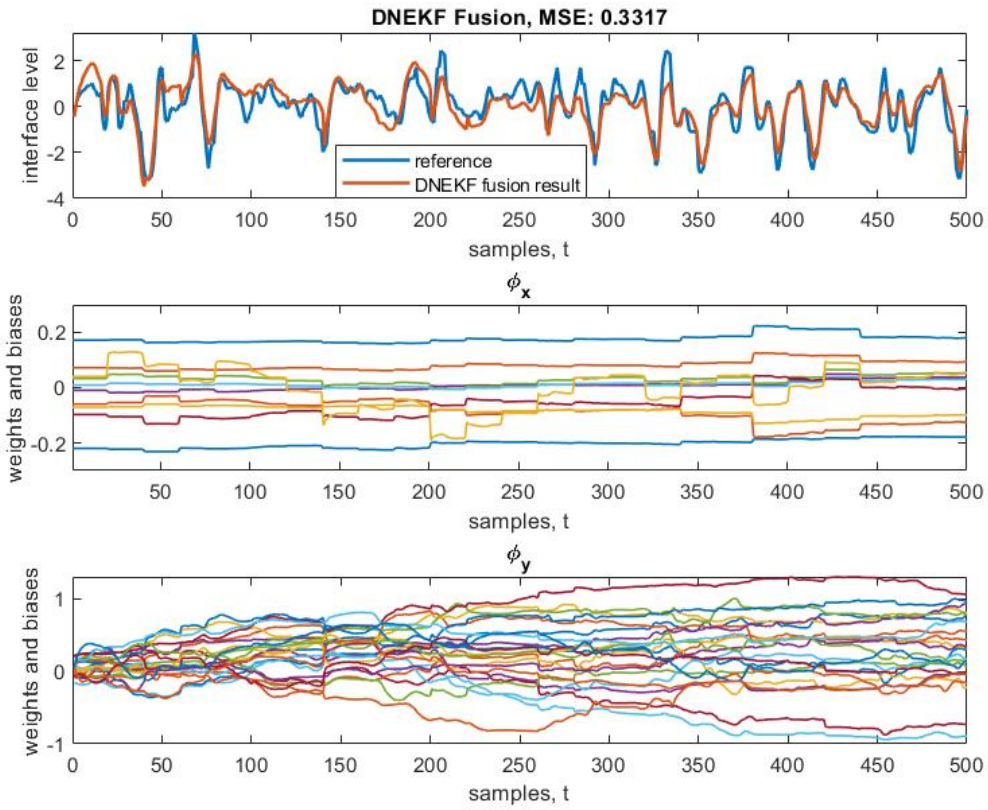

Figure 2.9: The DNEKF fusion with infrequent measurements available for every 20 frequent sampling intervals, and the weights and biases for SNN and MNN.

ments to update the weights and biases for MNN and SNN through a multirate strategy to improve the fusion robustness and accuracy. The effectiveness of the proposed approach is demonstrated through two numerical examples and one industrial application example. The simulation and industrial application results demonstrate that the DNEKF is robust to model inaccuracies and violations of noise assumption, and its performance can also be further improved by increasing the availability of infrequent accurate measurements.

Chapter 3

Multirate Sensor Data Fusion in Presence of Delayed Irregular Measurements using Synchronized Neural Extended Kalman Filters

3.1 Introduction

In Chapter 2, infrequent measurements are assumed to be available at a regular sampling rate without time delays. However, in reality, infrequent measurements usually have irregular sampling rate and time-varying time delays. As an example, lab technician usually collects samples irregularly and lab sample analysis requires time-consuming operations [34]. In this case, there are variable time delays between recorded sampling time and the time lab results become available, and such delays are usually unknown ahead of time. Therefore, the idea of the extended Kalman filter (EKF) based parallel fusion utilized in the dual neural EKF (DNEKF) is no longer applicable in this situation, when infrequent measurements have time-varying time delays [35].

To address the irregularity of infrequent measurements, track to track fusion (TTF), which fuses the Kalman filtering track estimation and covariances from different sensors, have been applied [36–38]. In [39], modified TTF (MTTF) was proposed to provide more advanced fusion techniques, which uses the fused results as common

predictions. The track fusion prediction (TFP) was also discussed in the same paper. In TFP algorithm, individual predictions from both Kalman filters are fused before correction steps, and then the two corrected estimates are fused to provide fusion results. Information matrix fusion (IMF) based TTF [40] was proposed as a high-level sensor data fusion architecture to guarantee a globally maintained track over time and demonstrated its improved fusion performance comparing with the cascaded Kalman filter based TTF. A modified adaptive TTF [41] was proposed to adopt cross-correlation between sensor-level track and global track to improve flexibility to react to the changes of sensor system. However, the above mentioned TTF based methods are limited to delay-free measurements. To address the measurement delays, back calculation fused Kalman filter (BFKF) method [42] was proposed, in which frequent Kalman filter calculations are repeated over the time delay period to incorporate the delayed infrequent measurements. This approach is applicable when only a few measurements are fused over the delay period or if the computational requirement of the filtering is not of problem. State augmentation based EKF [24] relies on augmenting current state with appropriate past information to fuse delayed measurements. However, it also suffers from the excessive computation problem. In [43], a Sigma-Point Kalman filter (SPKF) based time delayed sensor fusion approach was proposed, in which state vector is only augmented with state at the time instants when infrequent measurements are received. This approach assumes arrival time of infrequent measurements to be known in advance, which is usually not practical. To deal with multirate sensor fusion with irregular sampling rate and time-varying time delays, the modified delayed TTF (MDTTF) [44] and the exclusive information fusion Kalman filter (EIFKF) [25] were proposed. Both methods do not require to know availability time of the irregular infrequent measurements in advance. During fusion process, the MDTTF considers cross-covariances of frequent and infrequent measurements, while the EIFKF only fuses exclusive information of infrequent estimation with frequent estimation. The performance of the two methods was compared in [44].

Even though the EIFKF only fuses exclusive infrequent information with frequent estimation, it has comparable fusion performance as the MDTTF but with lower computational burden and hence has shorter average computational time (ACT).

As mentioned in Chapter 2, the state and output models may not be able to accurately describe the process dynamics. Model inaccuracies and violations of noise assumption have not been well investigated for multirate fusion in presence of delayed, irregular and infrequent measurements. In this Chapter, a DNEKF and state model compensation neural EKF (SNEKF) synchronization approach is proposed to address measurement irregularity and time-varying time delays while preserving estimation accuracy. In this proposed method, the DNEKF is applied to frequent estimation to compensate for both state and output model deficiencies. The irregular and infrequent measurements are considered to be accurate measurements, and as a result, infrequent model coefficient is considered as one. Therefore, the SNEKF is applied to infrequent estimation. The weights and biases of state model compensation neural network (SNN) are updated with infrequent measurements, and are shared between the DNEKF and the SNEKF procedures. Since the DNEKF approach increases computational cost comparing with the standard EKF, the fusion method proposed in the EIFKF is employed to reduce computational burden and improve fusion accuracy.

The remainder of this chapter is organized as follows. Section 3.2 explains the problems of irregular sampling rate and time-varying time delays in multirate sensor fusion process with inadequate process knowledge. Section 3.3 introduces the DNEKF and SNEKF synchronization approach to handle irregular infrequent measurements with time-varying time delays while compensating for model inaccuracy and violations of noise assumption. Then, two numerical examples and one industrial case study are provided in section 3.4 to demonstrate the advantages of the proposed approach. At last, section 3.5 concludes this chapter.

3.2 Problem Statement

In process industry, it is common to employ the lab analysis results to improve the quality variable estimation accuracy. However, such measurements are usually sampled at an infrequent and irregular rate and are obtained only after time-varying time delays. Therefore, regular and frequent online measurements, which have lower accuracy and do not have time delays, are commonly adopted as process measurements. To take advantage of all these sources, fusion of the two types of measurements is desired in order to provide frequent, high-performance quality variable estimation.

As illustrated in Figure 3.1, black ticks are frequent sampling instants denoted by t, and star represents infrequent sampling instants denoted by s. The infrequent measurement that corresponds to time s, $y_{i,s}$, is available at time ds, which is denoted by square. At time ds, the frequent measurement, $y_{f,ds}$, is available without time delay, and fusion is performed at this time instant. The intervals between time s and ds are time delays, d. In this study, both s and d are assumed to be multiple of t. The intervals between two sequential infrequent measurements are variable, and time delays, d, are also time-varying.

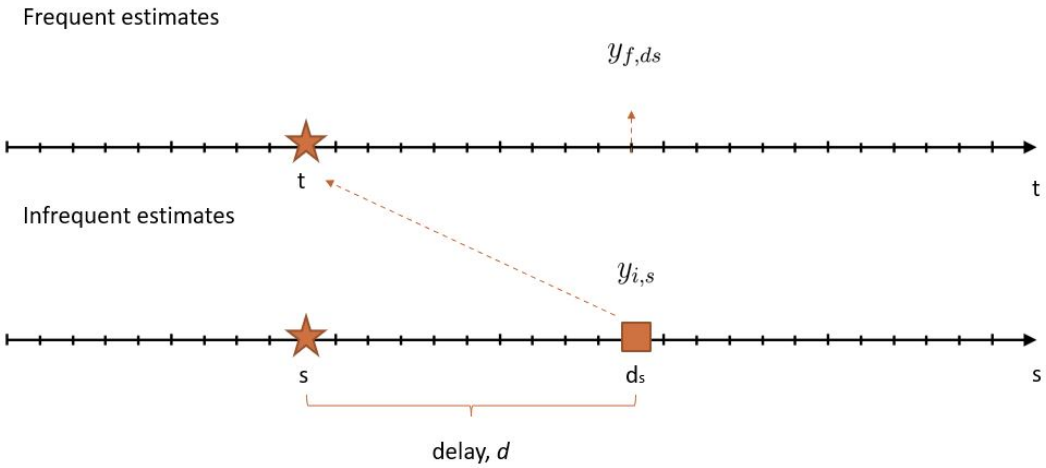

Figure 3.1: Process sampling strategy for regular frequent measurements and irregular infrequent measurements with time-varying time delays.

Considering the following nonlinear process with frequent and infrequent measure-

ments:

$$\begin{aligned} x_t &= f_{true}(x_{t-1}) + w_{t-1} \\ y_{f,t} &= h_{f,true}(x_t) + v_{f,t} \\ y_{i,ds} &= h_{i,true}(x_s) + v_{i,s} \end{aligned} \tag{3.1}$$

where $f_{true}(\cdot)$, $h_{f,true}(\cdot)$, and $h_{i,true}(\cdot)$ represent the true state model, frequent and infrequent output models. These models can be either linear or nonlinear. In this study, since infrequent measurements are considered to be accurate measurements, $h_{i,true}(x_s) = x_s$. The state, x, has w_t as its noise, and frequent and infrequent measurements are y_f and y_i, with $v_{f,t}$ and $v_{i,s}$ as their noises, respectively. The process noise and measurement noises, $w_t \sim N(0, Q)$, $v_{f,t} \sim N(0, R_f)$, and $v_{i,s} \sim N(0, R_i)$, are zero-mean, uncorrelated, Gaussian white noises. The multirate sensor data fusion accuracy heavily depends on accuracy of state and output models. Limited process knowledge and process condition changes can both lead to model-plant mismatches, and the assumption of white process noises can also be violated. When fusing regular frequent measurements with irregular infrequent measurements subject to time-varying time delays, model inaccuracies and violations of noise assumption should be considered. As shown in Figure 3.2, at time instant ds, frequent measurements, $y_{f,ds}$, arrive, then posterior frequent state estimate, $\hat{x}_{f,ds}$, is obtained. However, infrequent measurements arriving at time ds correspond to the sample that is taken at time s. Consequently, at time ds, posterior infrequent state estimate for time s, $\hat{x}_{i,s}$, is obtained, instead of at time ds. The time delay, d, is assumed to be unknown until at time ds. Therefore, to fuse frequent and infrequent estimates at time ds, predictions over the time delay period from time s to ds need to be made for infrequent estimation. Then at time ds, prior infrequent state estimate, $\hat{x}^-_{i,ds}$, and posterior frequent state estimate, $\hat{x}_{f,ds}$, are fused in the fusion center to obtain, $\hat{x}_{ds}$. The fusion results can be used as common initial estimates for predictions at the following time instants. In this scenario, model inaccuracies and violations of noise assumption will not only degrade the performance of frequent estimation but also affect predictions

over time delay period from time s to ds, where no corrections are available. When the state model has deficiency, errors will accumulate through these d-step predictions. The objective, therefore, is to compensate for model inaccuracies and violations of noise assumption while fusing regular frequent measurements and irregular infrequent measurements with time-varying time delays to improve the process state estimation accuracy.

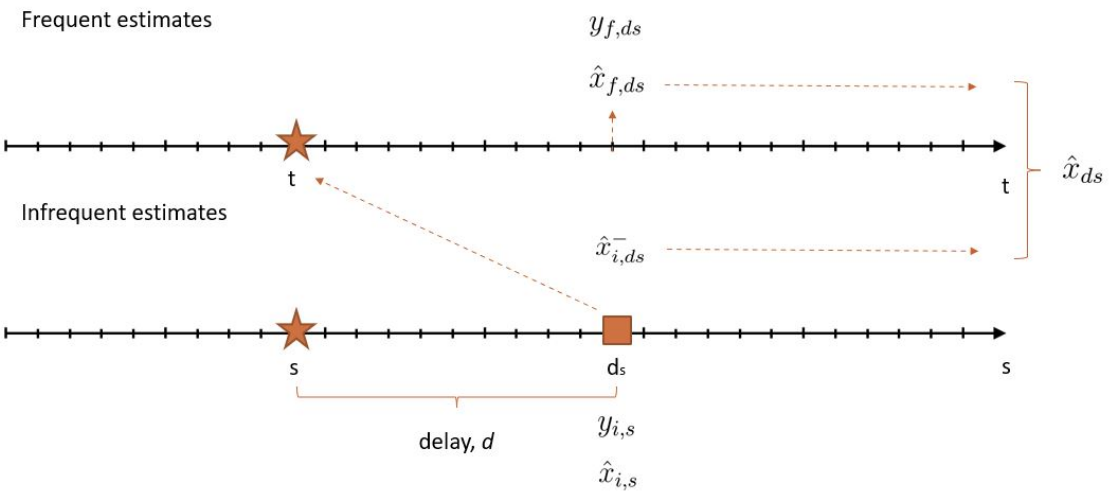

Figure 3.2: Frequent and infrequent estimations in presence of irregular and infrequent sampling rate and time-varying time delays.

3.3 DNEKF and SNEKF Synchronization Approach

3.3.1 DNEKF and SNEKF Estimations

While fusing multirate estimates in presence of irregular sampling rate and time-varying time delays, model inaccuracies and violations of noise assumption should be compensated. Due to the measurement time delays, the DNEKF approach, which is based on parallel fusion in Chapter 2, is no longer applicable. Two separate estimations can be employed synchronously to handle irregularity and time-varying time delays in infrequent measurements while improving the online quality variable estimation performance. In this section, the DNEKF and SNEKF synchronization

approach is proposed. As shown in Figure 3.3, the DNEKF is applied to frequent estimation and uses NN_x and NN_y values to compensate for model inaccuracies and violations of noise assumption. The SNEKF is applied to infrequent estimation to first improve state estimation at infrequent sampling instant, s, and then improve the predictions over time delay period from time s to ds. The SNN parameters are updated according to infrequent accurate measurements at time ds, and the weights and biases of SNN are shared between the DNEKF and the SNEKF estimations. Frequent and infrequent state estimations are fused in the fusion center to provide fused estimate, $\hat{x}_{ds}$, which is used as common initialization for predictions at the following time instants.

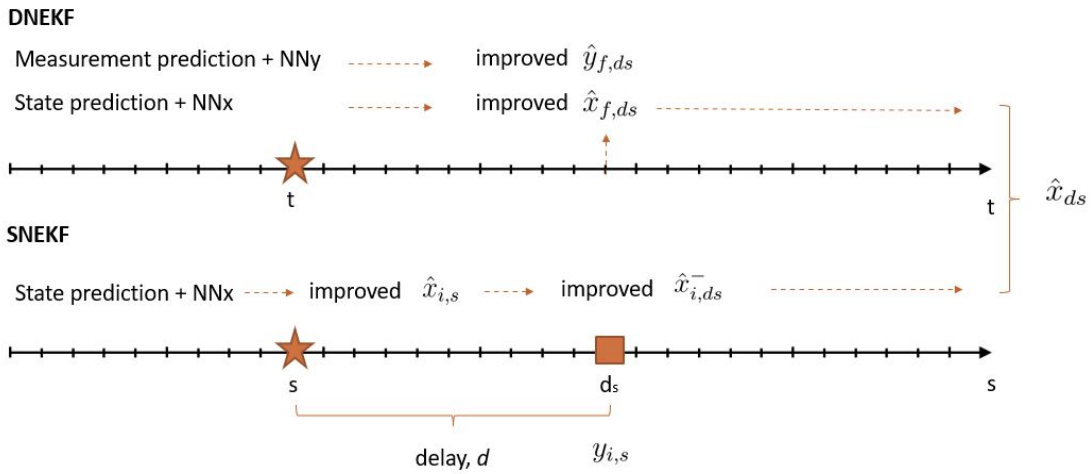

Figure 3.3: Multirate sensor data fusion based on the DNEKF and SNEKF synchronization approach.

The frequent DNEKF procedure is the same as that in Chapter 2 for *minor instants*, so frequent state and output predictions are

$$\hat{\bar{x}}^-_{f,t} = \begin{bmatrix} f(\hat{x}_{f,t-1}) + NN_x(\hat{x}_{f,t-1}, \hat{\phi}_{x,t-1}) \\ \hat{\phi}_{x,t-1} \\ \hat{\phi}_{y,t-1} \end{bmatrix} \tag{3.2}$$

$$\hat{y}_{f,t} = h_f(\hat{x}^-_{f,t}) + NN_y(\hat{x}^-_{f,t}, \hat{\phi}^-_{y,t}) \tag{3.3}$$

where $f(\cdot)$ and $h_f(\cdot)$ represent defective state and output models, which deviate from

$f_{true}(\cdot)$ and $h_{f,true}(\cdot)$ by model inaccuracies. The augmented frequent state vector is $\bar{x}_f = \begin{bmatrix} x_f & \phi_x & \phi_y \end{bmatrix}^T$, $\hat{x}_{f,t-1}$ is corrected state estimate and $\hat{y}_{f,t}$ is output prediction. The output from SNN is NN_x, with $\hat{x}_{f,t-1}$ as its input and $\hat{\phi}_x$ as the weights and biases. The MNN output is denoted as NN_y with $\hat{x}^-_{f,t}$ as its input and $\hat{\phi}_y$ as the weights and biases. In the prediction step, state estimation error covariance is calculated as:

$$P^-_{f,t} = \bar{F}_{f,t-1} P_{f,t-1} \bar{F}^T_{f,t-1} + Q \tag{3.4}$$

where $P_{f,t-1}$ is corrected frequent state estimation error covariance, and Q represents process noise covariance matrix. The frequent Jacobian matrix, $\bar{F}_{f,t-1}$ in equation (3.4), is

$$\begin{aligned} \bar{F}_{f,t-1} &= \begin{bmatrix} \frac{\partial (f+NN_x)}{\partial x}\Big|_{\hat{x}_{f,t-1}} & \frac{\partial (f+NN_x)}{\partial \phi_x}\Big|_{\hat{\phi}_{x,t-1}} & \frac{\partial (f+NN_x)}{\partial \phi_y}\Big|_{\hat{\phi}_{y,t-1}} \\ \mathbf{0} & I_{\phi_x} & \mathbf{0} \\ \mathbf{0} & \mathbf{0} & I_{\phi_y} \end{bmatrix} \\ &= \begin{bmatrix} F_{f,t-1} + \frac{\partial NN_x}{\partial x}\Big|_{\hat{x}_{t-1}} & \mathbf{0} & \mathbf{0} \\ \mathbf{0} & I_{\phi_x} & \mathbf{0} \\ \mathbf{0} & \mathbf{0} & I_{\phi_y} \end{bmatrix}_{(\phi_x+\phi_y+1)\times(\phi_x+\phi_y+1)} \end{aligned} \tag{3.5}$$

The Kalman gain matrix for frequent estimation is obtained as:

$$K_{f,t} = P^-_{f,t} \bar{H}^T_{f,t} (\bar{H}_{f,t} P^-_{f,t} \bar{H}^T_{f,t} + R_f)^{-1} \tag{3.6}$$

where R_f is frequent measurement noise covariance matrix, and the Jacobian matrix, $\bar{H}_{f,t}$, is calculated as:

$$\begin{aligned} \bar{H}_{f,t} &= \begin{bmatrix} \frac{\partial (h+NN_y)}{\partial x}\Big|_{\hat{x}^-_{f,t}} & \frac{\partial (h+NN_y)}{\partial \phi_x}\Big|_{\hat{\phi}^-_{x,t}} & \frac{\partial (h+NN_y)}{\partial \phi_y}\Big|_{\hat{\phi}^-_{y,t}} \end{bmatrix} \\ &= \begin{bmatrix} H_{f,t} + \frac{\partial NN_y}{\partial x}\Big|_{\hat{x}^-_{f,t}} & \mathbf{0} & \frac{\partial NN_y}{\partial \phi_y}\Big|_{\hat{\phi}^-_{y,t}} \end{bmatrix} \end{aligned} \tag{3.7}$$

In the correction step, both augmented state vector and state estimation error covariance are updated using frequent measurements, and the correction equations are

$$\hat{\bar{x}}_{f,t} = \hat{\bar{x}}^-_{f,t} + K_{f,t}(y_{f,t} - \hat{y}_{f,t}) \tag{3.8}$$

$$P_{f,t} = (I - K_{f,t}\bar{H}_{f,t})P_{f,t}^{-} \tag{3.9}$$

During the DNEKF procedure, ϕ_y is updated with frequent measurements, while ϕ_x remains unchanged.

Since delayed irregular and infrequent measurements are considered as accurate measurements, measurement model compensation neural network (MNN) does not need to be applied to the infrequent output prediction. Therefore, the SNEKF procedure is employed. The state and output predictions for the SNEKF procedure are

$$\hat{\bar{x}}_{i,s}^{-} = \begin{bmatrix} f(\hat{x}_{i,s-1}) + NN_x(\hat{x}_{i,s-1}, \hat{\phi}_{x,s-1}) \\ \hat{\phi}_{x,s-1} \end{bmatrix} \tag{3.10}$$

$$\hat{y}_{i,s} = h_i(\hat{x}_{i,s}^{-}) \tag{3.11}$$

where $\bar{x}_i = \begin{bmatrix} x_i & \phi_x \end{bmatrix}^T$ is augmented infrequent state vector, and $h_i(\hat{x}_{i,s}^{-}) = \hat{x}_{i,s}^{-}$, and $\hat{\bar{x}}_{i,s-1}$ is the corrected infrequent state estimation. Then estimation error covariance matrix is

$$P_{i,s}^{-} = \bar{F}_{i,s-1} P_{i,s-1} \bar{F}_{i,s-1}^{T} + Q \tag{3.12}$$

where $P_{i,s-1}$ is the corrected infrequent state estimation error covariance, and Q is process noise covariance matrix. The Jacobian matrix, $\bar{F}_{i,s-1}$, for infrequent estimation is calculated as:

$$\begin{aligned} \bar{F}_{i,s-1} &= \begin{bmatrix} \frac{\partial(f+NN_x)}{\partial x}\Big|_{\hat{x}_{i,s-1}} & \frac{\partial(f+NN_x)}{\partial \phi_x}\Big|_{\hat{\phi}_{x,s-1}} \\ \mathbf{0} & I_{\phi_x} \end{bmatrix} \\ &= \begin{bmatrix} F_{i,s-1} + \frac{\partial NN_x}{\partial x}\Big|_{\hat{x}_{i,s-1}} & \frac{\partial NN_x}{\partial \phi_x}\Big|_{\hat{\phi}_{x,s-1}} \\ \mathbf{0} & I_{\phi_x} \end{bmatrix}_{(\phi_x+1)\times(\phi_x+1)} \end{aligned} \tag{3.13}$$

The Kalman gain matrix is

$$K_{i,s} = P_{i,s}^{-} \bar{H}_{i,s}^{T} (\bar{H}_{i,s} P_{i,s}^{-} \bar{H}_{i,s}^{T} + R_i)^{-1} \tag{3.14}$$

where R_i is infrequent measurement noises covariance matrix, and the Jacobian matrix, $\bar{H}_{i,s}$, is

$$\begin{aligned}\bar{H}_{i,s} &= \begin{bmatrix} \frac{\partial h}{\partial x}\Big|_{\hat{x}^-_{i,s}} & \mathbf{0} \end{bmatrix} \\ &= \begin{bmatrix} H_{i,s} & \mathbf{0} \end{bmatrix}\end{aligned} \tag{3.15}$$

Finally, infrequent augmented state vector and state estimation error covariance are corrected as:

$$\hat{\bar{x}}_{i,s} = \hat{\bar{x}}^-_{i,s} + K_{i,s}(y_{i,s} - \hat{y}_{i,s}) \tag{3.16}$$

$$P_{i,s} = (I - K_{i,s}\bar{H}_{i,s})P^-_{i,s} \tag{3.17}$$

The irregular and infrequent measurements sampled at time instant s, become available at time ds, with relationship: $ds = s + d$. To fuse frequent and infrequent estimates in the fusion center, predictions over time delay period from time s to ds are made. Therefore, the infrequent estimation procedure includes additional prediction steps, which are specific to process state, x. The state prediction over the time delay period at frequent sampling rate is

$$\begin{aligned}\hat{x}^-_{i,s+1} &= f(\hat{x}_{i,s}) + NN_{x,s} \\ \hat{x}^-_{i,s+2} &= f(\hat{x}^-_{i,s+1}) + NN_{x,s+1} \\ &\vdots \\ \hat{x}^-_{i,ds} &= f(\hat{x}^-_{i,ds-1}) + NN_{x,ds-1}\end{aligned} \tag{3.18}$$

where $\hat{x}_{i,s}$ represents posterior infrequent state estimate at time s, which is obtained using irregular infrequent measurement received at time ds. The SNN output, NN_x, is applied to adjust predictions over the time delay period. During this procedure, corrections are not available, and the input to SNN changes from $\hat{x}_{i,s}$ to $\hat{x}^-_{i,ds-1}$, while ϕ_x remains unchanged. The predictions of estimation error covariance is also performed over the time delay period at frequent sampling rate, and can be calculated as:

$$\hat{P}^-_{i,ds} = \prod_{j=1}^{d-1}\left(\frac{\partial(f+NN_x)}{\partial x}\Big|_{\hat{x}^-_{i,s+j}}\right)\left(\frac{\partial(f+NN_x)}{\partial x}\Big|_{\hat{x}_{i,s}}\right)\hat{P}_{i,s}\left(\frac{\partial(f+NN_x)}{\partial x}\Big|_{\hat{x}_{i,s}}\right)^T\left(\prod_{j=1}^{d-1}\left(\frac{\partial(f+NN_x)}{\partial x}\Big|_{\hat{x}^-_{i,s+j}}\right)\right)^T + Q_{ds,s} \tag{3.19}$$

where $\hat{P}_i$ is estimation error covariance matrix corresponding to process state, and $Q_{ds,s}$ represents cumulative process state noise covariance from time s to ds, which can be computed as:

$$Q_{ds,s} = \sum_{j=1}^{d-1} \prod_{l=1}^{d-j} \left(\frac{\partial (f + NN_x)}{\partial x} \Big|_{\hat{x}^-_{i,s+l}} \right) \hat{Q} \left(\prod_{l=1}^{d-j} \left(\frac{\partial (f + NN_x)}{\partial x} \Big|_{\hat{x}^-_{i,s+l}} \right) \right)^T + \left(\frac{\partial (f + NN_x)}{\partial x} \Big|_{\hat{x}_{i,s}} \right) \hat{Q} \left(\frac{\partial (f + NN_x)}{\partial x} \Big|_{\hat{x}_{i,s}} \right)^T \tag{3.20}$$

where $\hat{Q}$ is process noise covariance corresponding to process state. The parameters of SNN are updated in the SNEKF procedure, and are shared with the DNEKF at time ds. The graphical illustration of the DNEKF and SNEKF synchronization approach is shown in Figure 3.4.

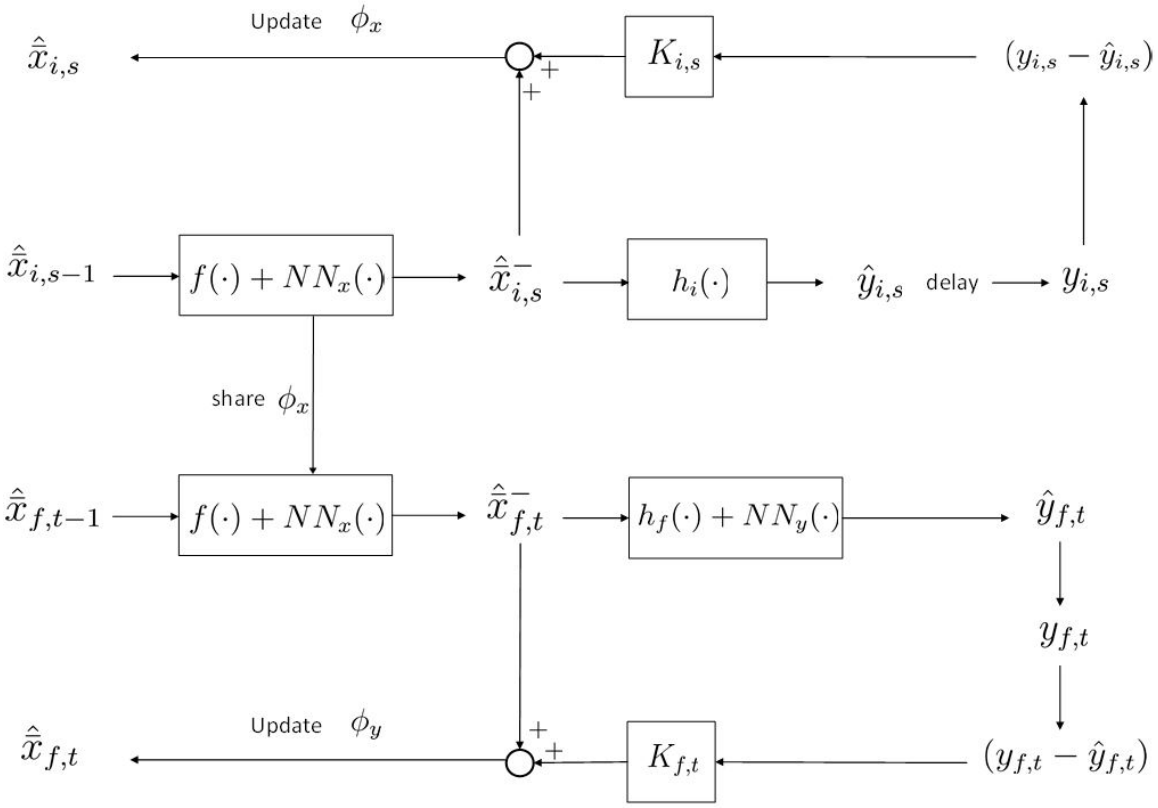

Figure 3.4: Graphical illustration of the DNKEF and SNEKF synchronization approach.

3.3.2 Fusion Procedure

After both frequent and infrequent estimates are obtained at time d_s, fusion can be performed in the fusion center. Recall that through state augmentation, $\bar{x}_f =$

$\begin{bmatrix} x_f & \phi_x & \phi_y \end{bmatrix}^T$ and $\bar{x}_i = \begin{bmatrix} x_i & \phi_x \end{bmatrix}^T$. Then ϕ_y is independent of $\bar{x}_i$, and ϕ_x is shared between the two estimations. Consequently, the fusion process focuses on process state, x, and its corresponding estimation error covariance, $\hat{P}$. A fusion method that fuses exclusive information of infrequent estimation with frequent estimation is proposed in the EIFKF approach [25], which is based on following Lemma:

Lemma 1. *Assume $\hat{x}_a$ and $\hat{x}_b$ are two unbiased, independent estimates of x, following Gaussian distributions, with P_a and P_b as their covariances, respectively. Then the optimal, unbiased fusion estimation $\hat{x}_c$ and its covariance matrix P_c in the sense of minimum mean-squared error can be calculated as*:

$$P_c = \left(P_a^{-1} + P_b^{-1}\right)^{-1} \tag{3.21}$$

$$\hat{x}_c = P_c \left(P_a^{-1}\hat{x}_a + P_b^{-1}\hat{x}_b\right) \tag{3.22}$$

The proof of this Lemma can be found in [45] and [46]. Lemma 1 is only applicable when two estimates are independent of each other. To apply this fusion technique, two unbiased independent estimates of $\hat{x}^-_{i,ds}$ are calculated through state predictions over time delay period from time s to ds. One of the estimates uses exclusive measurement information with frequent estimates and the other uses mutual measurement information. We name the two estimates as exclusive infrequent estimate, $\hat{z}^-_{ds}$, and mutual infrequent estimate, $\hat{x}^-_{ds}$, with $\hat{R}^-_{z,ds}$ and $\hat{P}^-_{ds}$ as their respective covariances. Then estimation error covariance of infrequent estimate at time ds can be written as:

$$\hat{P}^-_{i,ds} = \left(\left(\hat{P}^-_{ds}\right)^{-1} + \left(\hat{R}^-_{z,ds}\right)^{-1}\right)^{-1} \tag{3.23}$$

Rearrange equation (3.23), and $\hat{R}^-_{z,ds}$ can be obtained as:

$$\hat{R}^-_{z,ds} = \left(\left(\hat{P}^-_{i,ds}\right)^{-1} - \left(\hat{P}^-_{ds}\right)^{-1}\right)^{-1} \tag{3.24}$$

Following Lemma 1, infrequent state estimation are computed as:

$$\hat{x}^-_{i,ds} = \hat{P}^-_{i,ds}\left(\left(\hat{P}^-_{ds}\right)^{-1}\hat{x}^-_{ds} + \left(\hat{R}^-_{z,ds}\right)^{-1}\hat{z}^-_{ds}\right) \tag{3.25}$$

Then exclusive infrequent state estimation is

$$\hat{z}_{ds}^{-} = \hat{R}_{z,ds}^{-} \left(\left(\hat{P}_{i,ds}^{-} \right)^{-1} \hat{x}_{i,ds}^{-} - \left(\hat{P}_{ds}^{-} \right)^{-1} \hat{x}_{ds}^{-} \right) \tag{3.26}$$

The state propagation procedure and fusion procedure of the proposed DNEKF and SNEKF synchronization approach are shown in Figure 3.5. In this illustration, augmented state vectors $\hat{\bar{x}}_f$ and $\hat{\bar{x}}_i$ are propagated through time. However, only process state, x, participates in predictions over time delay period from time s to ds. In the fusion center, frequent state estimate, $\hat{x}_{f,ds}$, and exclusive infrequent state estimate, $\hat{z}_{ds}^{-}$, are fused to provide the fusion results, $\hat{x}_{ds}$.

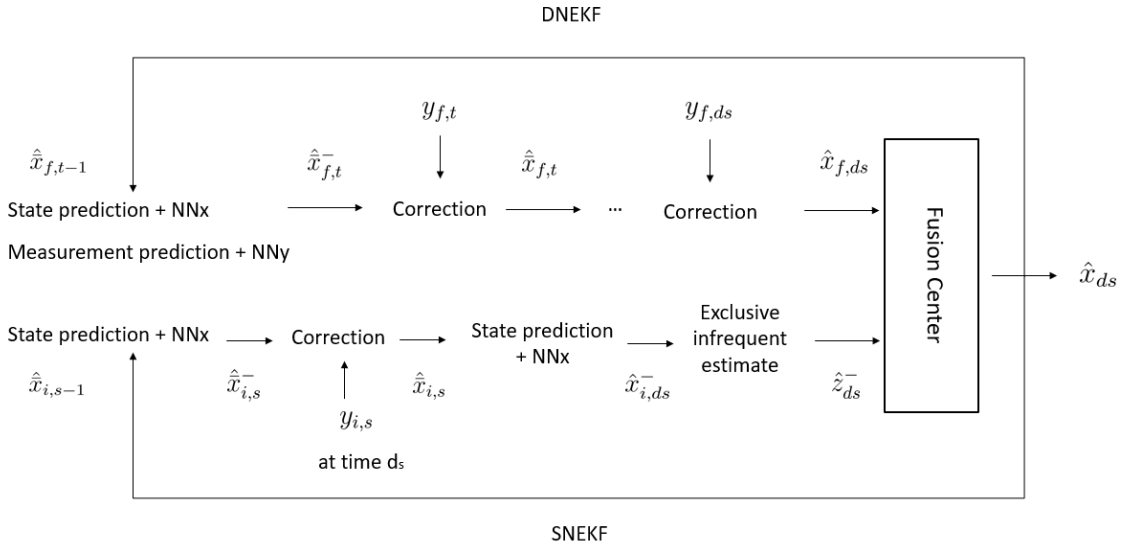

Figure 3.5: State propagation procedure and fusion process for the DNEKF and SNEKF synchronization approach to multirate sensor fusion in presence of delayed infrequent measurements.

In terms of the mutual information, at time s, the delayed infrequent measurements, $y_{i,s}$, are not available. Therefore, the common measurement information available at time s is used to provide mutual infrequent estimate from time s to ds, which

is calculated as:

$$\begin{aligned}
\hat{x}_{s+1}^{-} &= f(\hat{x}_{i,s}^{-}) + NN_{x,s} \\
\hat{x}_{s+2}^{-} &= f(\hat{x}_{s+1}^{-}) + NN_{x,s+1} \\
&\vdots \\
\hat{x}_{ds}^{-} &= f(\hat{x}_{ds-1}^{-}) + NN_{x,ds-1}
\end{aligned} \tag{3.27}$$

where $\hat{x}_{s+1}^{-}$ to $\hat{x}_{ds}^{-}$ represent state estimation using mutual measurement information over time delay period. Since the estimation is initialized with mutual information, $\hat{x}_{i,s}^{-}$ instead of $\hat{x}_{i,s}$, is used as the initial estimate, and the corresponding mutual infrequent state estimation error covariance is calculated as:

$$\hat{P}_{ds}^{-} = \prod_{j=1}^{d-1}\left(\frac{\partial(f+NN_x)}{\partial x}\Big|_{\hat{x}_{s+j}^{-}}\right)\left(\frac{\partial(f+NN_x)}{\partial x}\Big|_{\hat{x}_{i,s}^{-}}\right)\hat{P}_{i,s}^{-}\left(\frac{\partial(f+NN_x)}{\partial x}\Big|_{\hat{x}_{i,s}^{-}}\right)^{T}\left(\prod_{j=1}^{d-1}\left(\frac{\partial(f+NN_x)}{\partial x}\Big|_{\hat{x}_{s+j}^{-}}\right)\right)^{T} + Q_{ds,s}^{-} \tag{3.28}$$

where the estimation is initialized with $\hat{P}_{i,s}^{-}$ instead of $\hat{P}_{i,s}$ since only mutual measurement information is utilized. The corresponding mutual process noise covariance matrix, $Q_{ds,s}^{-}$, of the cumulative process state noise from s to ds is obtained as:

$$Q_{ds,s}^{-} = \sum_{j=1}^{d-1}\prod_{l=1}^{d-j}\left(\frac{\partial(f+NN_x)}{\partial x}\Big|_{\hat{x}_{s+l}^{-}}\right)\hat{Q}\left(\prod_{l=1}^{d-j}\left(\frac{\partial(f+NN_x)}{\partial x}\Big|_{\hat{x}_{s+l}^{-}}\right)\right)^{T} + \left(\frac{\partial(f+NN_x)}{\partial x}\Big|_{\hat{x}_{i,s}^{-}}\right)\hat{Q}\left(\frac{\partial(f+NN_x)}{\partial x}\Big|_{\hat{x}_{i,s}^{-}}\right)^{T} \tag{3.29}$$

After computing the mutual state estimate and its estimation error covariance, the exclusive infrequent state estimate and corresponding estimation error covariance at time ds, are calculated through equation (3.26) and equation (3.24). In the fusion center, only the exclusive infrequent information is fused with frequent estimation, and fusion can be performed based on Lemma 1 as follows:

$$\hat{P}_{ds} = \left(\hat{P}_{f,ds}^{-1} + \left(\hat{R}_{z,ds}^{-}\right)^{-1}\right)^{-1} \tag{3.30}$$

$$\hat{x}_{ds} = \hat{P}_{ds}\left(\hat{P}_{f,ds}^{-1}\hat{x}_{f,ds} + \left(\hat{R}_{z,ds}^{-}\right)^{-1}\hat{z}_{ds}^{-}\right) \tag{3.31}$$

The overall process of the DNEKF and SNEKF synchronization approach for multirate sensor fusion in presence of irregular and infrequent sampling rate and time-

varying time delays is illustrated in Figure 3.6. The exclusive infrequent state estimate and the corresponding estimation error covariance are fused with the frequent ones in the fusion center at time ds to provide more accurate fusion results, $\hat{x}_{ds}$ and $\hat{P}_{ds}$. These fused results can be used as initial values for frequent and infrequent estimations in the following sampling instants.

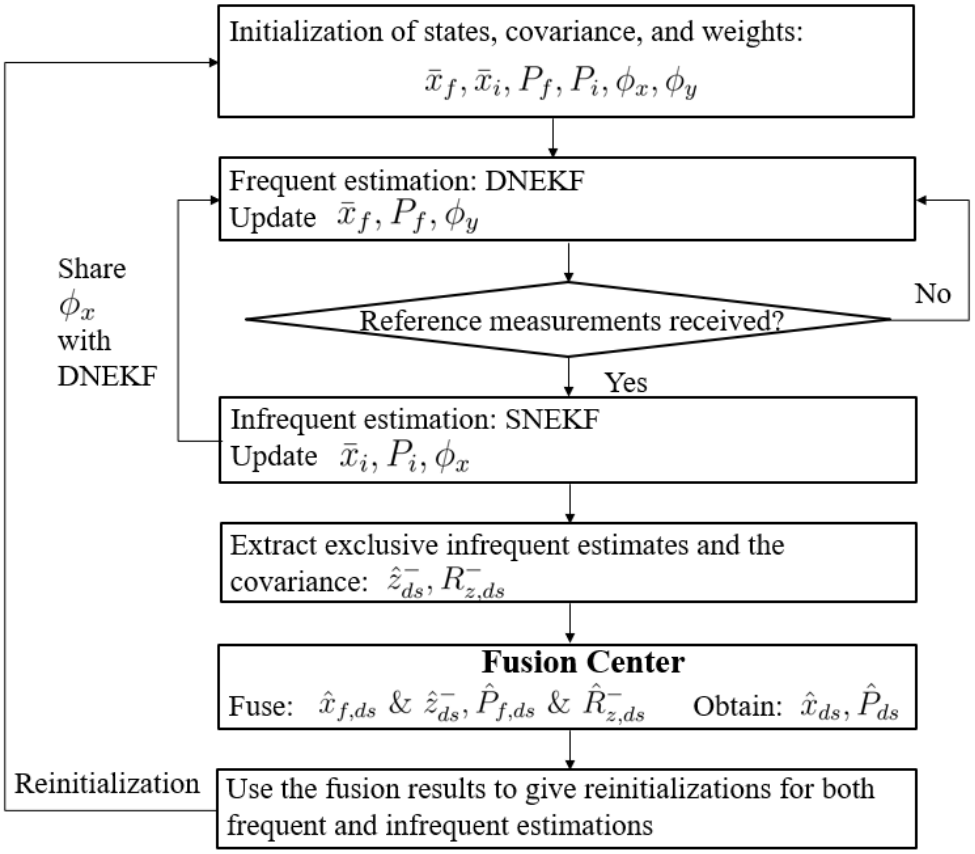

Figure 3.6: Flow chart of the DNEKF and SNEKF synchronization approach for multirate sensor fusion in presence of irregular and infrequent sampling rate and time-varying time delays.

3.4 Case Studies

In this section, two numerical examples as well as one industrial solvent recovery unit (SRU) product stream concentration estimation are provided to show advantages of the proposed approach. In the first numerical example, the state and frequent output

models deviate from the true ones. Next, colored state and measurement noises are applied to the process. Last, in the industrial case study, random walk models are applied, and the DNEKF and SNEKF synchronization approach is applied to improve accuracy of the SRU product stream concentration estimation.

3.4.1 Numerical Examples

3.4.1.1 Model Inaccuracies Compensation

In this numerical example, both state model and frequent output model are inaccurate. The infrequent accurate measurements are available at an irregular sampling rate with time-varying time delays over the 400 simulated frequent sampling instants. Infrequent sampling interval randomly varies between 35 and 45 times of frequent rate sampling intervals. The time delay, d, varies from 15 to 25 times of frequent sampling intervals following a uniform distribution. In this simulation, true state and frequent output models are

$$\begin{aligned} x_t &= f_{true}(x_{t-1}) + w_{t-1} \\ &= \sqrt{x_{t-1}} + sin(x_{t-1}) + w_{t-1} \end{aligned} \tag{3.32}$$

and

$$\begin{aligned} y_{f,t} &= h_{true}(x_{f,t}) + v_{f,t} \\ &= 0.8x_{f,t}^2 + v_{f,t} \end{aligned} \tag{3.33}$$

where $w_t \sim N(0, 0.1)$ and $v_{f,t} \sim N(0, 1)$. The irregular infrequent measurements are considered as accurate output measurements. Therefore, infrequent output model is given below:

$$y_{i,s} = x_{i,s} + v_{i,s} \tag{3.34}$$

where $v_{i,s} \sim N(0, 0.1)$. In this simulation, assume neither the true state model nor the true frequent output model is known. The following defective models are applied for estimation:

$$\begin{aligned} \hat{x}_t^- &= f(\hat{x}_{t-1}) \\ &= 0.9\hat{x}_{t-1} + sin(\hat{x}_{t-1}) \end{aligned} \tag{3.35}$$

and

$$\begin{aligned}\hat{y}_{f,t} &= h(\hat{x}^{-}_{f,t}) \\ &= \hat{x}^{2}_{f,t}{}^{-}\end{aligned} \tag{3.36}$$

Applying the DNEKF procedure to frequent estimation process and choosing 1-2-1 as neural network structure for both SNN and MNN, then state and output predictions are

$$\hat{\bar{x}}^{-}_{f,t} = \begin{bmatrix} 0.9\hat{x}_{f,t-1} + sin(\hat{x}_{f,t-1}) + NN_x(\hat{x}_{f,t-1}, \hat{\phi}_{x,t-1}) \\ \hat{\phi}_{x,t-1} \\ \hat{\phi}_{y,t-1} \end{bmatrix} \tag{3.37}$$

and

$$\hat{y}_{f,t} = \hat{x}^{2}_{f,t}{}^{-} + NN_y(\hat{x}^{-}_{f,t}, \hat{\phi}^{-}_{y,t}) \tag{3.38}$$

With above structure, both neural networks have 7 parameters. For a single quality variable problem, the augmented state vector contains 15 elements. The frequent Jacobian matrices, $\bar{F}_{f,t-1}$ and $\bar{H}_{f,t}$, are computed as:

$$\bar{F}_{f,t-1} = \begin{bmatrix} 0.9 + cos(\hat{x}^{-}_{f,t-1}) + \frac{\partial NN_x}{\partial x}\Big|_{\hat{x}_{f,t-1}} & \mathbf{0} & \mathbf{0} \\ \mathbf{0} & I_{\phi_x} & \mathbf{0} \\ \mathbf{0} & \mathbf{0} & I_{\phi_y} \end{bmatrix}_{15\times 15} \tag{3.39}$$

and

$$\bar{H}_{f,t} = \begin{bmatrix} 2\hat{x}^{-}_{f,t} + \frac{\partial NN_y}{\partial x}\Big|_{\hat{x}^{-}_{f,t}} & \mathbf{0} & \frac{\partial NN_y}{\partial \phi_y}\Big|_{\hat{\phi}^{-}_{y,t}} \end{bmatrix} \tag{3.40}$$

The SNEKF algorithm is applied to infrequent estimation process. Infrequent state and output predictions are

$$\hat{\bar{x}}^{-}_{i,s} = \begin{bmatrix} 0.9\hat{x}_{i,s-1} + sin(\hat{x}_{i,s-1}) + NN_x(\hat{x}_{i,s-1}, \hat{\phi}_{x,s-1}) \\ \hat{\phi}_{x,s-1} \end{bmatrix} \tag{3.41}$$

$$\hat{y}_{i,s} = \hat{x}^{-}_{i,s} \tag{3.42}$$

The infrequent Jacobian matrices, $\bar{F}_{i,s-1}$ and $\bar{H}_{i,s}$, are computed as:

$$\bar{F}_{i,s-1} = \begin{bmatrix} 0.9 + cos(\hat{x}_{i,s-1}) + \frac{\partial NN_x}{\partial x}\Big|_{\hat{x}_{i,s-1}} & \frac{\partial NN_x}{\partial \phi_x}\Big|_{\hat{\phi}_{x,s-1}} \\ \mathbf{0} & I_{\phi_x} \end{bmatrix}_{8\times 8} \tag{3.43}$$

and

$$\bar{H}_{i,s} = \begin{bmatrix} 1 & \mathbf{0} \end{bmatrix} \tag{3.44}$$

State predictions over time delay period from time s to ds are needed for fusion activity. Following the fusion algorithm introduced in section 3.3.2, in order to extract exclusive infrequent state estimate, mutual infrequent state estimates from time s to ds are computed as:

$$\begin{aligned} \hat{x}^-_{s+1} &= 0.9\hat{x}^-_{i,s} + sin(\hat{x}^-_{i,s}) + NN_{x,s} \\ \hat{x}^-_{s+2} &= 0.9\hat{x}^-_{s+1} + sin(\hat{x}^-_{s+1}) + NN_{x,s+1} \\ &\vdots \\ \hat{x}^-_{ds} &= 0.9\hat{x}^-_{ds-1} + sin(\hat{x}^-_{ds-1}) + NN_{x,ds-1} \end{aligned} \tag{3.45}$$

where $\hat{x}^-_{i,s}$ is prior infrequent state estimate at time s. The estimation error covariance of mutual infrequent state estimate is calculated as:

$$\begin{aligned} \hat{P}^-_{ds} = &\prod_{j=1}^{d-1} \left(0.9 + cos(\hat{x}^-_{s+j}) + \frac{\partial NN_x}{\partial x}\Big|_{\hat{x}^-_{s+j}}\right) \left(0.9 + cos(\hat{x}^-_{i,s}) + \frac{\partial NN_x}{\partial x}\Big|_{\hat{x}^-_{i,s}}\right) \hat{P}^-_{i,s} \\ &\cdot \left(0.9 + cos(\hat{x}^-_{i,s}) + \frac{\partial NN_x}{\partial x}\Big|_{\hat{x}^-_{i,s}}\right)^T \left(\prod_{j=1}^{d-1} \left(0.9 + cos(\hat{x}^-_{s+j}) + \frac{\partial NN_x}{\partial x}\Big|_{\hat{x}^-_{s+j}}\right)\right)^T + Q^-_{ds,s} \end{aligned} \tag{3.46}$$

where $\hat{P}^-_{i,s}$ is prior state estimation error covariance at time s, and $Q^-_{ds,s}$ can be computed as:

$$\begin{aligned} Q^-_{ds,s} = &\sum_{j=1}^{d-1} \prod_{l=1}^{d-j} \left(0.9 + cos(\hat{x}^-_{s+l}) + \frac{\partial NN_x}{\partial x}\Big|_{\hat{x}^-_{s+l}}\right) \hat{Q} \left(\prod_{l=1}^{d-j} \left(0.9 + cos(\hat{x}^-_{s+l}) + \frac{\partial NN_x}{\partial x}\Big|_{\hat{x}^-_{s+l}}\right)\right)^T \\ &+ \left(0.9 + cos(\hat{x}^-_{i,s}) + \frac{\partial NN_x}{\partial x}\Big|_{\hat{x}^-_{i,s}}\right) \hat{Q} \left(0.9 + cos(\hat{x}^-_{i,s}) + \frac{\partial NN_x}{\partial x}\Big|_{\hat{x}^-_{i,s}}\right)^T \end{aligned} \tag{3.47}$$

The infrequent state estimate, $\hat{x}^{-}_{i,ds}$, from time s to ds is calculated as following:

$$\begin{aligned}
\hat{x}^{-}_{i,s+1} &= 0.9\hat{x}_{i,s} + sin(\hat{x}_{i,s}) + NN_{x,s} \\
\hat{x}^{-}_{i,s+2} &= 0.9\hat{x}^{-}_{i,s+1} + sin(\hat{x}^{-}_{i,s+1}) + NN_{x,s+1} \\
&\vdots \\
\hat{x}^{-}_{i,ds} &= 0.9\hat{x}^{-}_{i,ds-1} + sin(\hat{x}^{-}_{i,ds-1}) + NN_{x,ds-1}
\end{aligned} \tag{3.48}$$

where $\hat{x}_{i,s}$ is posterior infrequent state estimate for time s. Its corresponding estimation error covariance, $\hat{P}^{-}_{i,ds}$, is

$$\begin{aligned}
\hat{P}^{-}_{i,ds} = &\prod_{j=1}^{d-1}\left(0.9 + cos(\hat{x}^{-}_{i,s+j}) + \frac{\partial NN_x}{\partial x}\Big|_{\hat{x}^{-}_{i,s+j}}\right)\left(0.9 + cos(\hat{x}_{i,s}) + \frac{\partial NN_x}{\partial x}\Big|_{\hat{x}_{i,s}}\right)\hat{P}_{i,s} \\
&\cdot\left(0.9 + cos(\hat{x}_{i,s}) + \frac{\partial NN_x}{\partial x}\Big|_{\hat{x}_{i,s}}\right)^T\left(\prod_{j=1}^{d-1}\left(0.9 + cos(\hat{x}^{-}_{i,s+j}) + \frac{\partial NN_x}{\partial x}\Big|_{\hat{x}^{-}_{i,s+j}}\right)\right)^T + Q_{ds,s}
\end{aligned} \tag{3.49}$$

where $\hat{P}_{i,s}$ is corrected state estimation error covariance, and $Q_{ds,s}$ can be obtained as:

$$\begin{aligned}
Q_{ds,s} = &\sum_{j=1}^{d-1}\prod_{l=1}^{d-j}\left(0.9 + cos(\hat{x}^{-}_{i,s+l}) + \frac{\partial NN_x}{\partial x}\Big|_{\hat{x}^{-}_{i,s+l}}\right)\hat{Q}\left(\prod_{l=1}^{d-j}\left(0.9 + cos(\hat{x}^{-}_{i,s+l}) + \frac{\partial NN_x}{\partial x}\Big|_{\hat{x}^{-}_{i,s+l}}\right)\right)^T \\
&+\left(0.9 + cos(\hat{x}_{i,s}) + \frac{\partial NN_x}{\partial x}\Big|_{\hat{x}_{i,s}}\right)\hat{Q}\left(0.9 + cos(\hat{x}_{i,s}) + \frac{\partial NN_x}{\partial x}\Big|_{\hat{x}_{i,s}}\right)^T
\end{aligned} \tag{3.50}$$

After obtaining $\hat{x}^{-}_{ds}$, $\hat{P}^{-}_{ds}$, $\hat{x}^{-}_{i,ds}$, and $\hat{P}_{i,ds}$ through equation (3.45), (3.46), (3.48) and (3.49), exclusive infrequent state estimate at time ds, $\hat{z}^{-}_{ds}$, and its corresponding estimation error covariance, $\hat{R}^{-}_{z,ds}$, are obtained through equation (3.26) and equation (3.24). Then the fused state estimate and corresponding estimation error covariance are obtained from equation (3.31) and equation (3.30). Figure 3.5 illustrates the standard EKF estimation results and fusion results from the proposed DNEKF and SNEKF synchronization approach. As shown in this figure, inaccurate models lead to biases between the EKF estimates and actual process states. With compensation of model inaccuracies, the MSE of the proposed approach is calculated as 0.10945, which is smaller than 0.86271 from the EKF estimates, indicating that the proposed method has improved the estimation performance.

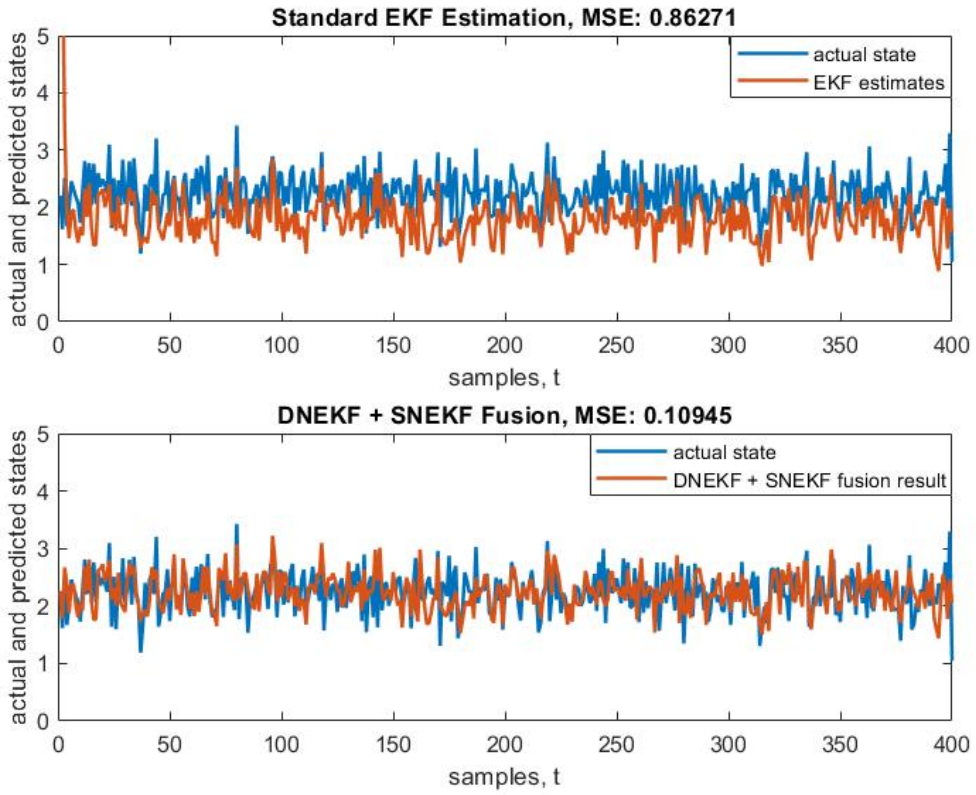

Figure 3.7: The EKF estimation results vs. the DNEKF and SNEKF synchronization fusion results for numerical example with model inaccuracies.

3.4.1.2 Colored Noises Compensation

In this example, accurate models in equation (3.32) and (3.33) are available. However, colored noises instead of white noises are considered. Red noises with correlation along time as 0.5 are generated through equation (2.48) and applied to the process state and output measurements. The frequent Jacobian matrices, $\bar{F}_{f,t-1}$ and $\bar{H}_{f,t}$, in the DNEKF process, are

$$\bar{F}_{f,t-1} = \begin{bmatrix} \frac{1}{2\sqrt{\hat{x}^-_{f,t-1}}} + cos(\hat{x}^-_{f,t-1}) + \frac{\partial NN_x}{\partial x}\Big|_{\hat{x}_{f,t-1}} & \mathbf{0} & \mathbf{0} \\ \mathbf{0} & I_{\phi_x} & \mathbf{0} \\ \mathbf{0} & \mathbf{0} & I_{\phi_y} \end{bmatrix}_{15\times 15} \tag{3.51}$$

and

$$\bar{H}_{f,t} = \begin{bmatrix} 1.6\hat{x}^-_{f,t} + \frac{\partial NN_y}{\partial x}\Big|_{\hat{x}^-_{f,t}} & \mathbf{0} & \frac{\partial NN_y}{\partial \phi_y}\Big|_{\hat{\phi}^-_{y,t}} \end{bmatrix} \tag{3.52}$$

In terms of infrequent SNEKF process, the infrequent Jacobian matrices, $\bar{F}_{i,s-1}$ and $\bar{H}_{i,s}$, are

$$\bar{F}_{i,s-1} = \begin{bmatrix} \frac{1}{2\sqrt{\hat{x}_{i,s-1}^{-}}} + cos(\hat{x}_{i,s-1}) + \frac{\partial NN_x}{\partial x}\Big|_{\hat{x}_{i,s-1}} & \frac{\partial NN_x}{\partial \phi_x}\Big|_{\hat{\phi}_{x,s-1}} \\ \mathbf{0} & I_{\phi_x} \end{bmatrix}_{8\times 8} \tag{3.53}$$

and

$$\bar{H}_{i,s} = \begin{bmatrix} 1 & \mathbf{0} \end{bmatrix} \tag{3.54}$$

As shown in Figure 3.8 and 3.9, violations of noise assumption degrade the EKF estimation results, and even lead to EKF estimation divergence. Through compensation of violations of noise assumption, the DNEKF and SNEKF synchronization method can prevent the estimation from divergence and improve the estimation accuracy in terms of MSE.

3.4.2 SRU Product Stream Concentration Estimation

Bitumen produced from oil sands mainly consists of long-chain hydrocarbon molecules and it is extra heavy and highly viscous. The sticky, viscous bitumen is almost in solid state at room temperatures, which makes it difficult to transport [47]. To solve this problem, diluent is added to make it possible to ship bitumen through pipelines. After transportation, the diluent is recovered in SRU through heating and stripping processes. After diluent recovery, SRU product stream concentration is estimated at a frequent sampling rate through a soft sensor. The product stream samples are also analyzed in the lab to provide accurate concentration measurements at an irregular and infrequent rate [48]. In this case study, all the industrial data has been normalized for proprietary reason. The soft sensor estimation results are available in every 10 minutes without time delay. Meanwhile, the lab measurements are available two or three times per day to provide references for product stream concentrations. Usually, the delay is 18 to 30 frequent sampling intervals, following a uniform distribution.

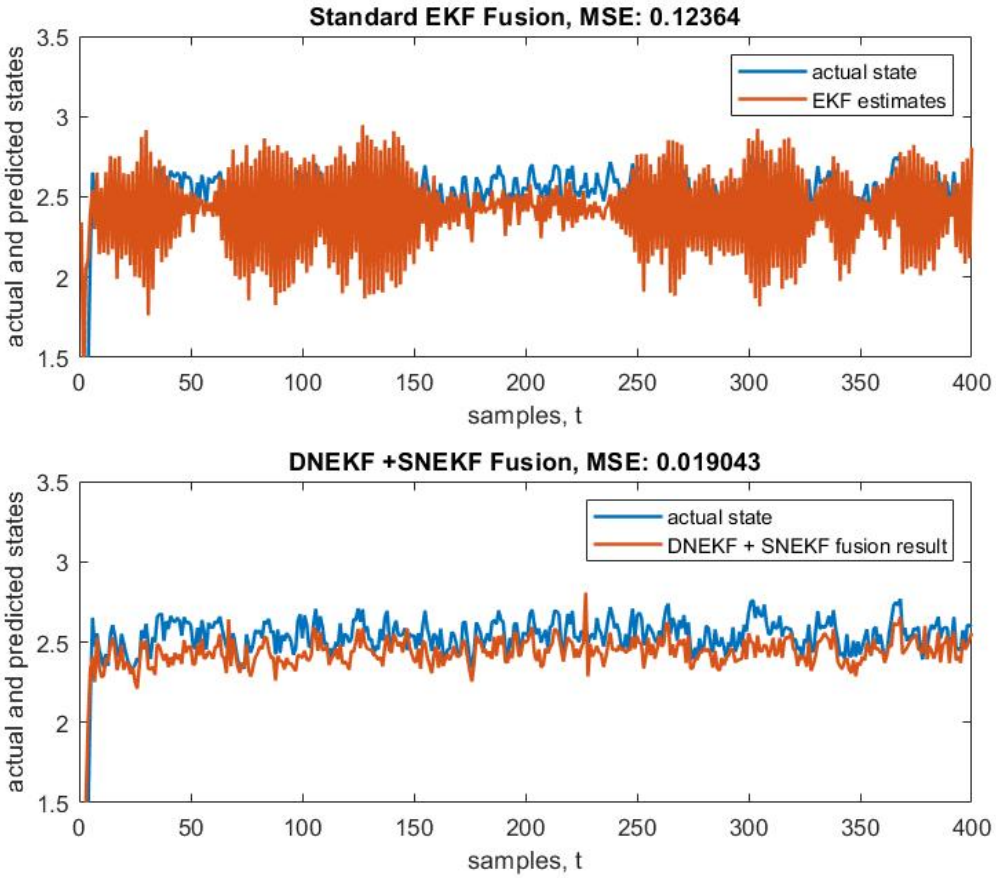

Figure 3.8: The EKF estimation results vs. the DNEKF and SNEKF synchronization fusion results for numerical example with colored noise.

Industrial data from two separate time periods with a gap of three months is analyzed in this case study.

The DNEKF approach is applied to frequent estimation process using soft sensor measurements with random walk models, and state and output predictions are

$$\hat{\bar{x}}_{f,t}^{-} = \begin{bmatrix} \hat{x}_{f,t-1} + NN_x(\hat{x}_{f,t-1}, \hat{\phi}_{x,t-1}) \\ \hat{\phi}_{x,t-1} \\ \hat{\phi}_{y,t-1} \end{bmatrix} \tag{3.55}$$

$$\hat{y}_{f,t} = \hat{x}_{f,t}^{-} + NN_y(\hat{x}_{f,t}^{-}, \hat{\phi}_{y,t}^{-}) \tag{3.56}$$

Structures of SNN and MNN are both 1-2-1, then the Jacobian matrices for the

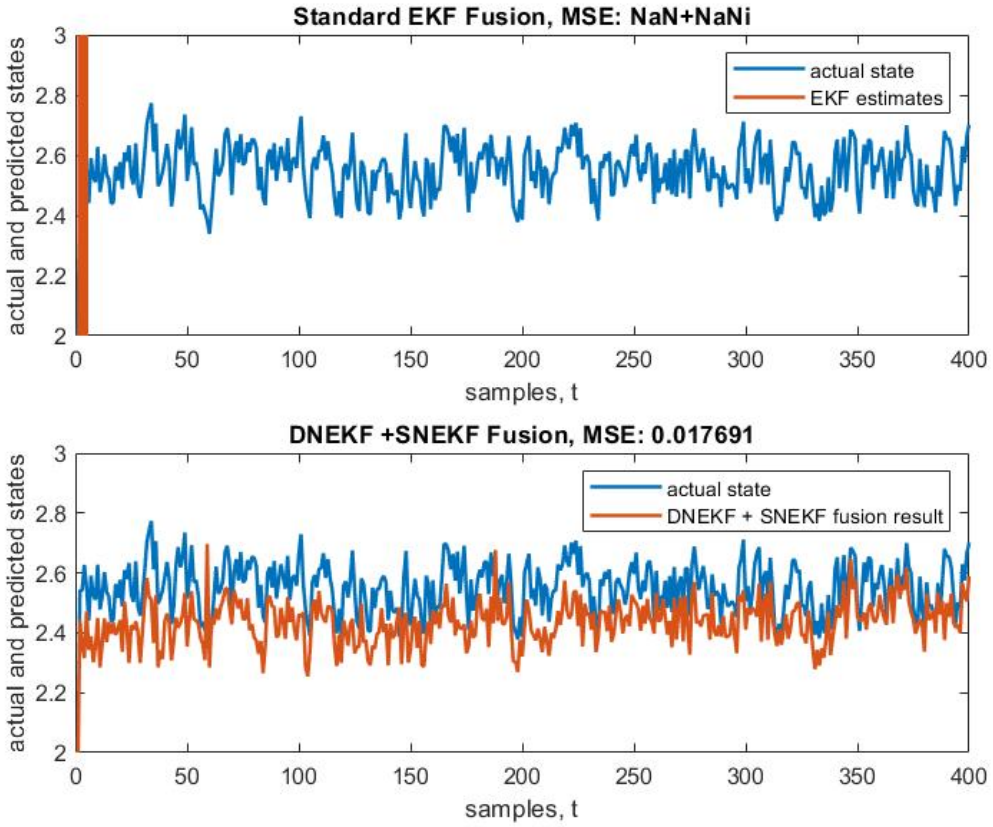

Figure 3.9: The EKF estimation results vs. the DNEKF and SNEKF synchronization fusion results for numerical example with colored noise.

frequent estimation are

$$\bar{F}_{f,t-1} = \begin{bmatrix} 1 + \frac{\partial NN_x}{\partial x}\Big|_{\hat{x}_{t-1}} & \mathbf{0} & \mathbf{0} \\ \mathbf{0} & I_{\phi_x} & \mathbf{0} \\ \mathbf{0} & \mathbf{0} & I_{\phi_y} \end{bmatrix}_{15\times 15} \tag{3.57}$$

and

$$\bar{H}_{f,t} = \begin{bmatrix} 1 + \frac{\partial NN_y}{\partial x}\Big|_{\hat{x}^-_{f,t}} & \mathbf{0} & \frac{\partial NN_y}{\partial \phi_y}\Big|_{\hat{\phi}^-_{y,t}} \end{bmatrix} \tag{3.58}$$

The SNEKF approach is applied to infrequent estimation, and state and output predictions are

$$\hat{\bar{x}}^-_{i,s} = \begin{bmatrix} \hat{x}_{i,s-1} + NN_x(\hat{x}_{i,s-1}, \hat{\phi}_{x,s-1}) \\ \hat{\phi}_{x,s-1} \end{bmatrix} \tag{3.59}$$

$$\hat{y}_{i,s} = \hat{x}^{-}_{i,s} \tag{3.60}$$

The infrequent Jacobian matrices are

$$\bar{F}_{i,s-1} = \begin{bmatrix} 1 + \frac{\partial NN_x}{\partial x}\Big|_{\hat{x}_{i,s-1}} & \frac{\partial NN_x}{\partial \phi_x}\Big|_{\hat{\phi}_{x,s-1}} \\ \mathbf{0} & I_{\phi_x} \end{bmatrix}_{8\times 8} \tag{3.61}$$

and

$$\bar{H}_{i,s} = \begin{bmatrix} 1 & \mathbf{0} \end{bmatrix} \tag{3.62}$$

After extracting exclusive infrequent state estimate and corresponding covariance, fusion is performed when lab measurements become available. Figures 3.10 and Figure 3.11 show frequent soft sensor measurements and the proposed DNEKF and SNEKF synchronization fusion results using lab measurements as references for two time periods. The comparison of estimation accuracies for soft sensor predictions, the EIFKF estimation, and the proposed method fusion results in terms of MSE is presented in Table 3.1, with lab measurements as references. From the MSE comparison, the proposed synchronization method improves estimation accuracy from frequent soft sensor measurements as well as from the EIFKF estimation by compensating the model deficiencies.

Table 3.1: MSE from different methods for the SRU product stream concentration estimation case study.

	Methods	**MSE**
Period 1	Soft sensor measurement	0.1295
	EIFKF	0.1057
	DNEKF + SNEKF fusion result	0.0934
Period 2	Soft sensor measurement	0.5298
	EIFKF	0.4948
	DNEKF + SNEKF fusion result	0.3741

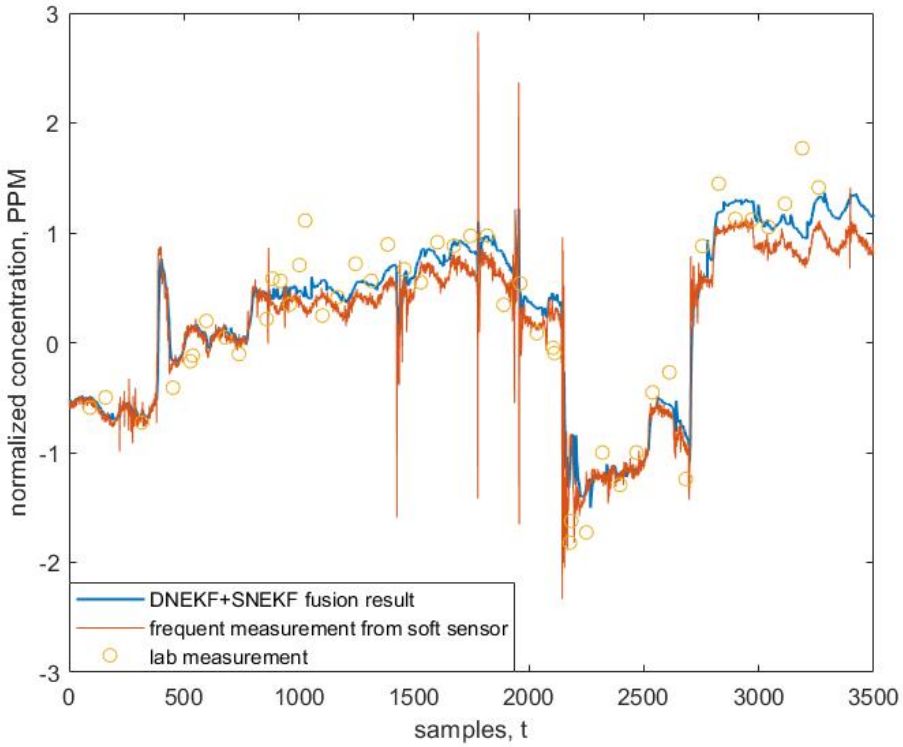

Figure 3.10: Frequent soft sensor measurements vs. the DNEKF and SNEKF synchronization fusion results for SRU product stream concentration estimation during period 1.

3.5 Conclusions

In this chapter, the DNEKF and SNEKF synchronization approach is proposed for multirate sensor fusion in presence of irregular and infrequent measurements with time-varying time delays. With the objective of compensating model inaccuracies and violations of noise assumption, the proposed method uses the DNEKF and the SNEKF to improve frequent and infrequent estimations, respectively, while sharing the parameters of SNN between them. The regular frequent state estimate and irregular infrequent state estimate as well as their corresponding covariances are fused in the fusion center when infrequent accurate measurements arrive, and exact delay is unknown in advance. Through two numerical examples and one industrial case study, the proposed approach is shown to have advantages of compensating for model inaccuracies and violations of noise assumption while handling the measurement ir-

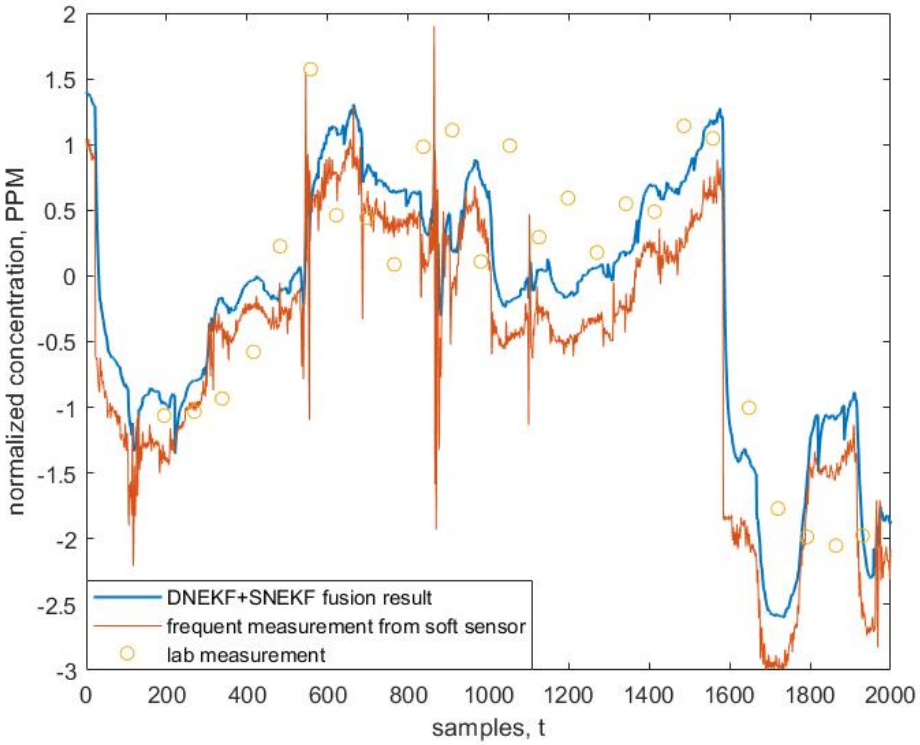

Figure 3.11: Frequent soft sensor measurement vs. the DNEKF and SNEKF synchronization fusion results for SRU product stream concentration estimation during period 2.

regularity and time-varying time delays.

Chapter 4

Sensor Fusion and Computer Vision Integrated System for Primary Separation Cell Interface Level Estimation

4.1 Introduction

Primary Separation Cell (PSC) is used to separate bitumen from oil sands slurry through a water-based gravity separation process. General structure of PSC is a large open separation vessel, and a typical cross-sectional view of PSC is shown in Figure 2.6. It is the key step of bitumen extraction, where up to 90% of the bitumen is recovered [49]. Oil sands slurry is pumped to the PSC for extraction through inlet pipeline. Then the slurry is divided into three layers due to gravity: the froth layer, middlings layer, and tailings layer, from top to bottom. The froth layer has the lowest density and contains majority of bitumen. Inside the PSC, bitumen froth floats towards the top and is recovered in the overflow launder. The middlings zone sits underneath the froth layer and mainly consists of clay particles that are difficult to separate. The tailings layer sits at the bottom of the PSC. It is mostly comprised of coarse tails and is withdrawn from the bottom of cone via underflow pumps. The exact location of the froth-middlings interface is a critical control parameter. If the interface is too high, middlings will get pulled into the overflow launder and thus

reduce bitumen recover quality. If the interface is too low, bitumen will get pulled into the middlings zone, which can reduce bitumen recovery. In oil sands industry, the froth-middlings interface level is measured using various sensors: nuclear density profiler, differential pressure (DP) cell, integrated sensor, and image processing based computer vision system. The profiler measures the interface level based on point density measurements. DP cells estimate the interface level through pressure measurements. The integrated sensor combines density and pressure transmitters to give interface level estimation. The computer vision system uses a camera that is installed on the sight glasses to capture sight glass visions and then transmits video frames to the application computer, which then converts the image frames to interface level estimation. In recent years, cost of camera installation has dropped, and accuracy of digital imaging software has improved significantly, making image processing technique increasingly popular in the oil sands industry. However, this approach highly relies on sight glass vision qualities. When camera is not able to capture a clear movement of the interface level, the computer vision will freeze itself by holding on to the last reading of interface level until the visions become reliable again. The objective of this chapter is to design a sensor fusion strategy which can be integrated with the image processing based computer vision system to improve online interface level estimation accuracy and robustness for PSCs.

The remainder of this chapter is organized as follows. Section 4.2 introduces the image processing based computer vision system and discusses about the problems that exist. Section 4.3 explains the sensor fusion approach, which recursively updates fusion parameters to continuously providing reliable interface level estimation when computer vision results are unreliable. The integration strategy of sensor fusion with computer vision system is also introduced in this section. Real industrial environment simulations are conducted at the computer process control (CPC) industrial research chair (IRC) lab at the University of Alberta to show effectiveness of the proposed approach. Finally, section 4.4 concludes this chapter.

4.2 Image Processing based Computer Vision System and Problem Statement

The image processing based computer vision system for froth-middlings interface level detection in PSC [33] was developed to increase the interface level estimation accuracy. This approach combines static and dynamic image processing techniques, and provides indications when the results are not reliable. The image processing procedure relies on visions of the PSC sight glasses. Figure 4.1 illustrates a sample sight glass vision captured by the installed camera. Typically, three sight glasses are installed on the PSC, named as upper, middle, and lower sight glass, respectively. The red line is the computer vision estimation result for froth-middlings interface level, and the yellow ellipses indicate transition regions among the three sight glasses.

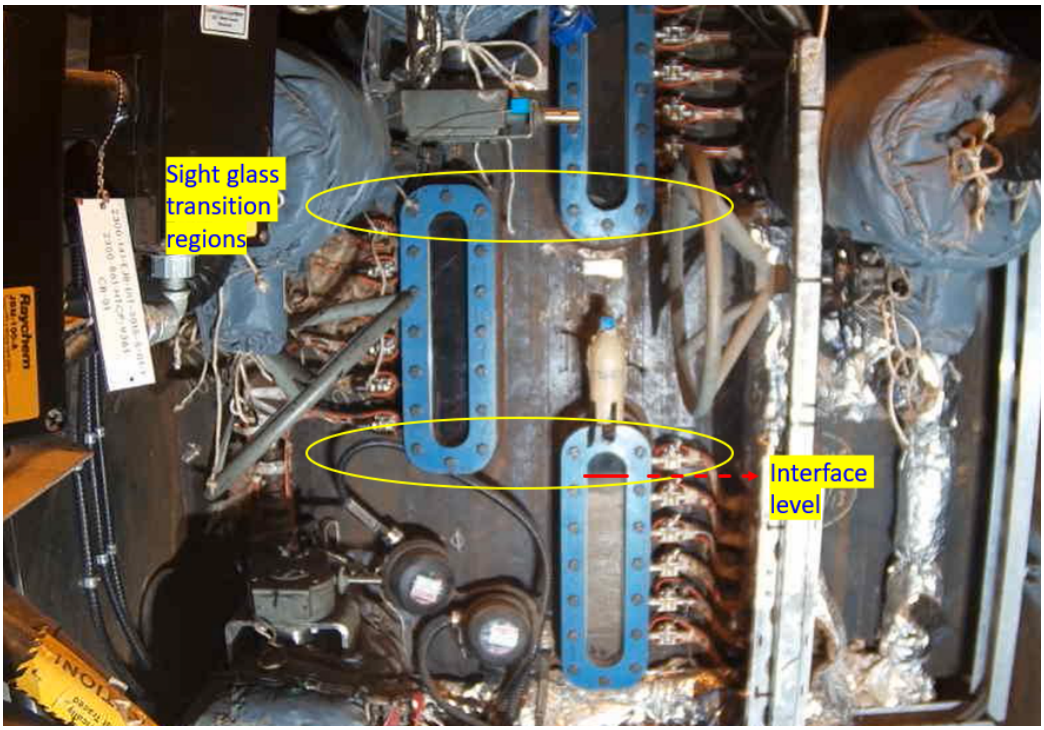

Figure 4.1: Sample sight glass visions of PSC.

The vision qualities are affected by several abnormalities. Sticky oil and sticky sands will lower the visibility of the interface level [50]. Besides, when the interface

level crosses sight glass transition regions, dynamic movement of the interface level is difficult to be captured by camera. In this case, dynamic image processing is not able to provide accurate estimates [51]. The above two scenarios are defined as low-quality conditions in the computer vision system. Additionally, operators occasionally need to do maintenance on the PSC and will block the camera visions. Then the sight glass regions are not visible and calculation of interface level is not reliable [52]. This situation is called low-reliability condition in the computer vision system. Figure 4.2a and 4.2b show the stains on the sight glass and operator blocking the sight glass visions, respectively. During normal conditions, the computer vision results are considered to be the most accurate among various sensor estimations. Figure 4.3

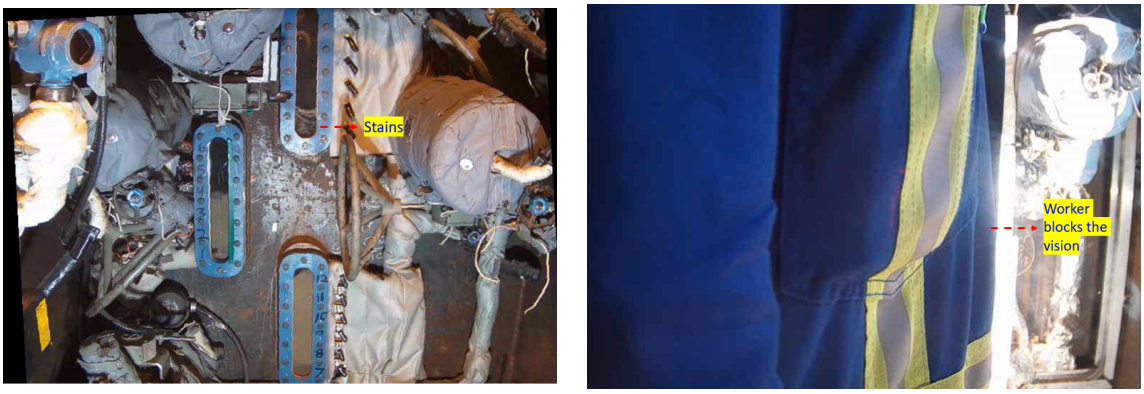

(a) (b)

Figure 4.2: Illustration of sight glass stains and operator blocking condition.

shows sample graphical user interface (GUI) for the image processing based computer vision system [33]. The red ellipse marks the quality and reliability status. Both indication indices range from 0 to 1, and larger value means higher reliability. If either indication index value is lower than its threshold, the computer vision results will remain unchanged until the condition becomes normal again, and the threshold values are adjusted according to the operational environments. Figure 4.4 shows one-month computer vision interface level estimation results with sampling interval of 10s. All data in this chapter has been normalized for proprietary reason. The red dashed lines mark the computer vision results corresponding to the two sight

glass transition regions. During transition regions, the camera is not able to capture clear movement of the interface level, and the quality index falls below its threshold. Then the computer vision freezes interface estimation until the quality index higher than the threshold. The objective of this work is to provide reliable dynamic interface level estimation during low-quality and low-reliability scenarios of the computer vision system.

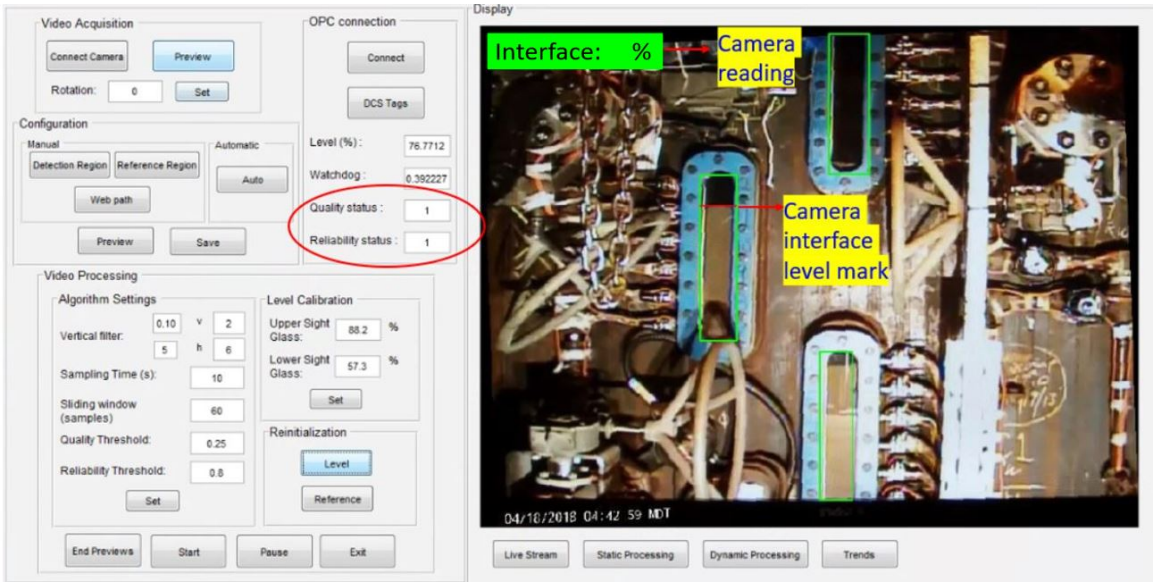

Figure 4.3: GUI for image processing based computer vision system for interface level estimation.

4.3 Sensor Fusion Approach

4.3.1 Fusion Application with Quality and Reliability Status

In the PSC interface level estimation case study of Chapter 2, the computer vision results are considered as equivalence to accurate measurements. However, if the computer vision results are in a low-quality or low-reliability condition, these readings should not be used as accurate measurements to be fused with other measurements. The sensor fusion using measurements from other sensors is more reliable under abnormal scenarios. In this chapter, a simplified version of sensor fusion approaches for the computer vision system is proposed for industrial application, where the ex-

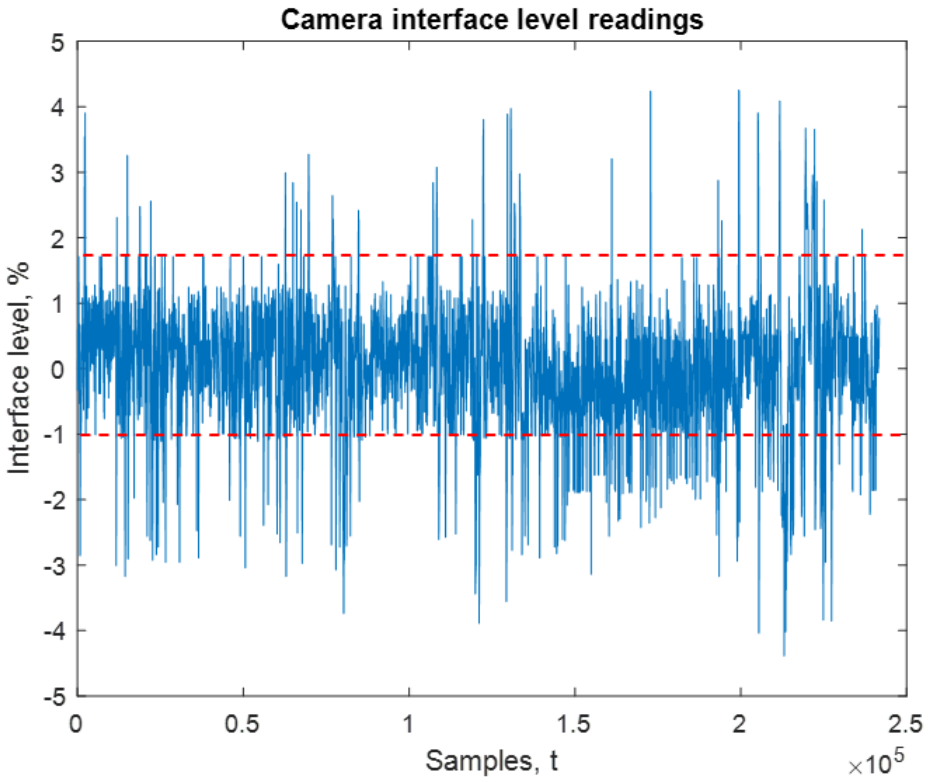

Figure 4.4: Sample one-month computer vision results.

isting distributed control system (DCS) limits how complex the algorithm can be. Under normal conditions, reliable computer vision results are used as references to adaptively calibrate the fusion parameters of other sensors using the recursive least square (RLS) algorithm. Once the quality index or reliability index falls below their thresholds, the latest trained fusion model parameters and bias remain unchanged to continuously providing interface level estimation. The linear fusion model can be written as:

$$y_t = \alpha_t x_{1,t} + \beta_t x_{2,t} + \gamma_t x_{3,t} + bias_t \tag{4.1}$$

where y_t is the interface level measurement from computer vision system under reliable conditions, $x_{1,t}$, $x_{2,t}$, and $x_{3,t}$ represent the measurements from DP cell, profiler, and integrated sensor, respectively. The fusion parameters, α_t, β_t, γ_t, and the bias term, $bias_t$, are updated whenever computer vision result is available and reliable. Similar

to the Kalman filter algorithm, in the RLS algorithm, the estimated fusion parameters are calibrated using the measurement residuals as [53, 54]:

$$\hat{\theta}_t = \hat{\theta}_{t-1} + K_t(y_t - X_t^T \hat{\theta}_{t-1}) \tag{4.2}$$

where $X = \begin{bmatrix} x_1 & x_2 & x_3 & 1 \end{bmatrix}^T$, and $\theta = \begin{bmatrix} \alpha & \beta & \gamma & bias \end{bmatrix}^T$. The Kalman gain matrix K_t is calculated as:

$$K_t = \frac{\lambda^{-1} P_{t-1} X_t}{1 + \lambda^{-1} X_t^T P_{t-1} X_t} \tag{4.3}$$

where λ is forgetting factor with value between 0 and 1. Smaller forgetting factor will make the model more sensitive to recent samples [55]. The estimation error covariance is denoted as P_t, and it is updated as [56]:

$$P_t = \lambda^{-1} P_{t-1} - \lambda^{-1} K_t X_t^T P_{t-1} \tag{4.4}$$

In this study, update of fusion parameters is according to the computer vision quality and reliability status. Only when both reliability and quality indices are higher than their respective threshold, the fusion parameters and biases are updated. The updating rule is defined as:

$$\hat{\theta}_t = \begin{cases} \hat{\theta}_{t-1}, & \text{if quality index or reliability index} < \text{threshold} \\ \hat{\theta}_{t-1} + K_t(y_t - X_t^T \hat{\theta}_{t-1}), & \text{if quality index and reliability index} \geqslant \text{threshold} \end{cases} \tag{4.5}$$

To test the reliability of the sensor fusion results, 10-hour predictions are made using one-month industrial data. The correlations between results directly from computer vision system under reliable conditions and estimations from sensor fusion and individual sensors are presented in Table 4.1. The sensor fusion interface level estimation has higher consistency with the computer vision results than each individual sensor in terms of correlation. Figure 4.5 and 4.6 demonstrate sample 10-hour sensor fusion results. The computer vision results, which use a camera to capture the sight

glass visions, are plot as references, but they are not utilized to update fusion parameters during the 10-hour sensor fusion period. Red dashed ellipses mark the sight glass transition regions, where the computer vision results remain unchanged. As shown in Figure 4.5 and 4.6, the sensor fusion results do not suffer from this problem. Therefore, the sensor fusion can address the low-quality and low-reliability problems form computer vision system and preserve estimation accuracy. Usually, abnormal conditions will not last for more than several hours, so the 10-hour estimation tests prove the effectiveness of using sensor fusion in presence of abnormalities.

Table 4.1: Correlations between the computer vision results and estimations from sensor fusion and individual sensors.

Sensors	**Correlation**
DP cell	0.7445
Profiler	0.3428
Integrated sensor	0.4772
Sensor fusion	0.7977

4.3.2 Sensor Fusion Integration with Computer Vision System

In section 4.3.1, the sensor fusion results are proved to be robust and reliable to provide alternative estimates under abnormal scenarios. Then sensor fusion is integrated with the computer vision interface level estimation system, which was developed previously, and the integrated system has been implemented in the industry. Previously, the computer vision system uses quality and reliability indices to determine when to freeze the interface level estimation. To handle the abnormalities and continuously providing estimation values, a simplified version of sensor fusion approaches is utilized, which uses the quality and reliability indices to determine when to update fusion parameters, and thus provide dynamic interface level estimation when computer vision results are unreliable. An improved GUI for industry is shown in Figure

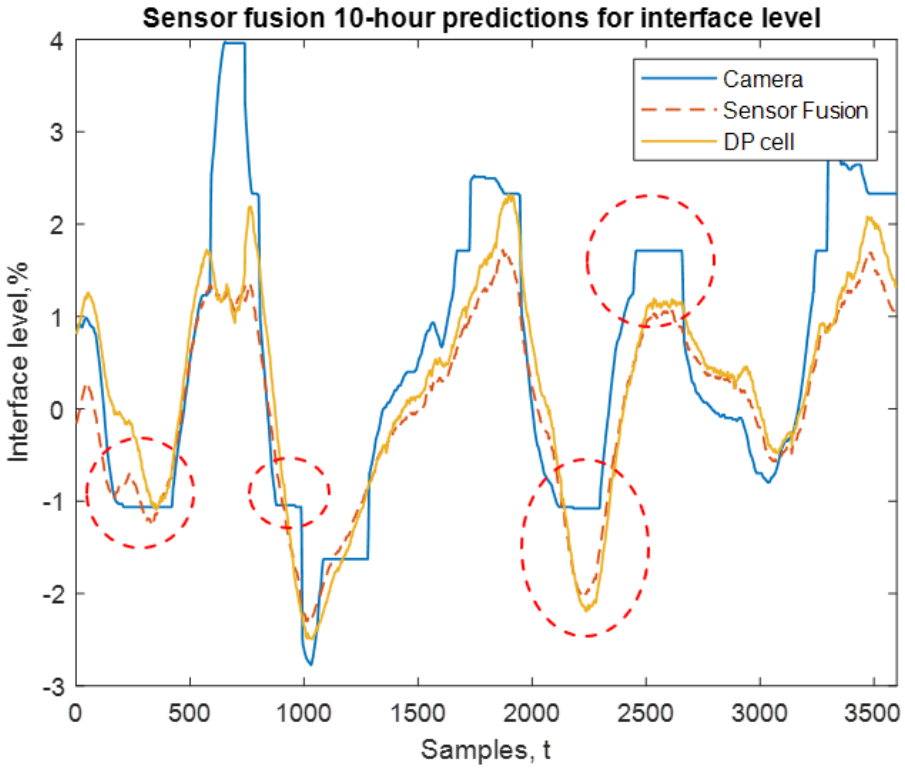

Figure 4.5: Sample 10-hour sensor fusion interface level estimation with corresponding computer vision and DP cell results.

4.7. In this GUI, two boxes showing interface level readings are provided, and the exact values are hided for proprietary reason. The background color of the computer vision box changes from green to yellow under the low-quality conditions and changes from green to red under low-reliability conditions. The red line is the computer vision result, and the blue line indicates the sensor fusion result. The updated software has been implemented in the industry for field tests, where both sensor fusion and computer vision results are indicated on the GUI. In the computer vision system [33], a camera is used to capture and transmit visions of the sight glasses to the application computer, meanwhile a video processing application runs in the background to infer the level from video frames. On the basis of the previous computer vision system implementation architecture, measurements from DP cell, profiler, and integrated sensor are inputs to the fusion algorithm through open protocol communication (OPC). The

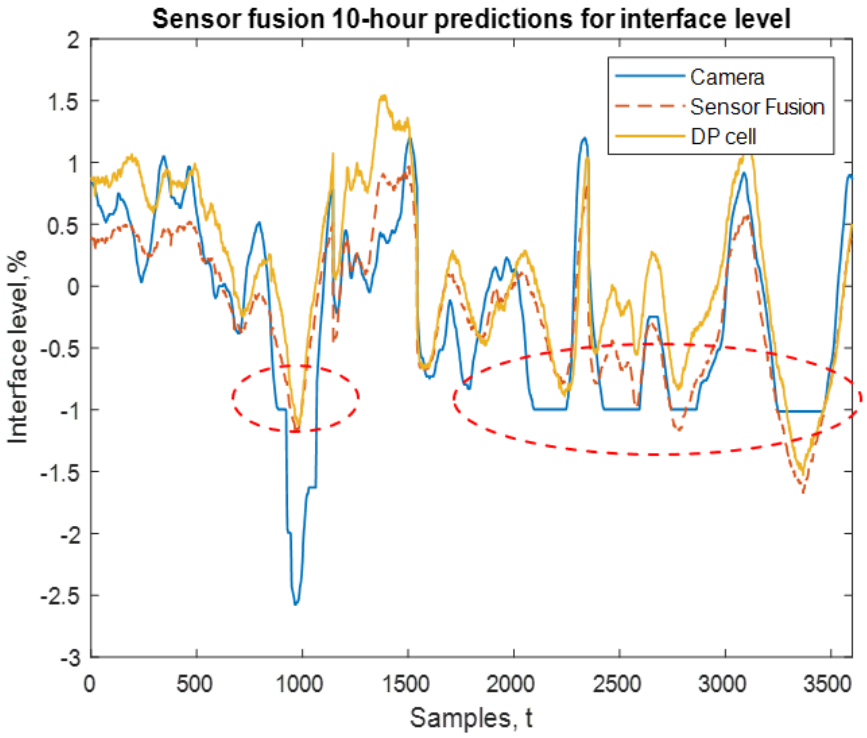

Figure 4.6: Sample 10-hour sensor fusion interface level estimation with corresponding computer vision and DP cell results.

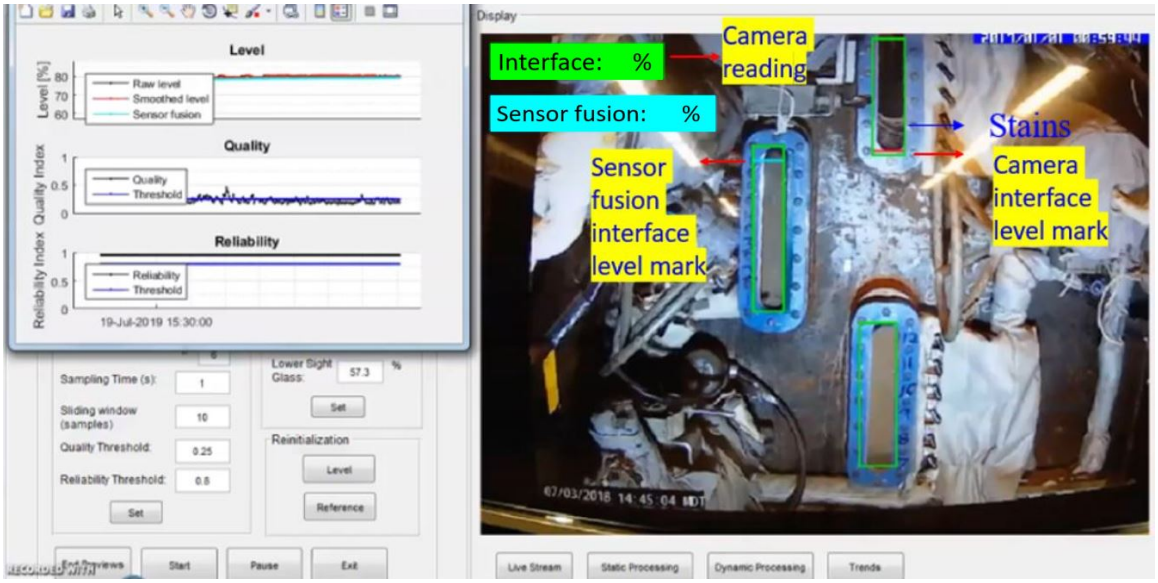

Figure 4.7: Sample sensor fusion and computer vision integrated system GUI.

integrated algorithm computes both the sensor fusion and computer vision results at the application computer. Then two types of estimations are communicated through

OPC to the DCS in industry. The video stream with two level indicators (red line and blue line) is transmitted to a web server that can be visualized from the control room. In the initial stage of implementation, only DP cell measurements are imported through OPC. Thus, in this section, sensor fusion simulations using only industrial DP cell measurements and computer vision results are reported, and the updated implementation architecture of sensor fusion and computer vision integrated system is shown in Figure 4.8. The computer vision results when they are reliable are used to recursively calibrate the DP cell parameters. The following equation is applied to provide interface level estimates:

$$y_t = \alpha_t x_{1,t} + bias_t \tag{4.6}$$

The factory acceptance test (FAT) was performed in the CPC IRC lab at the Uni-

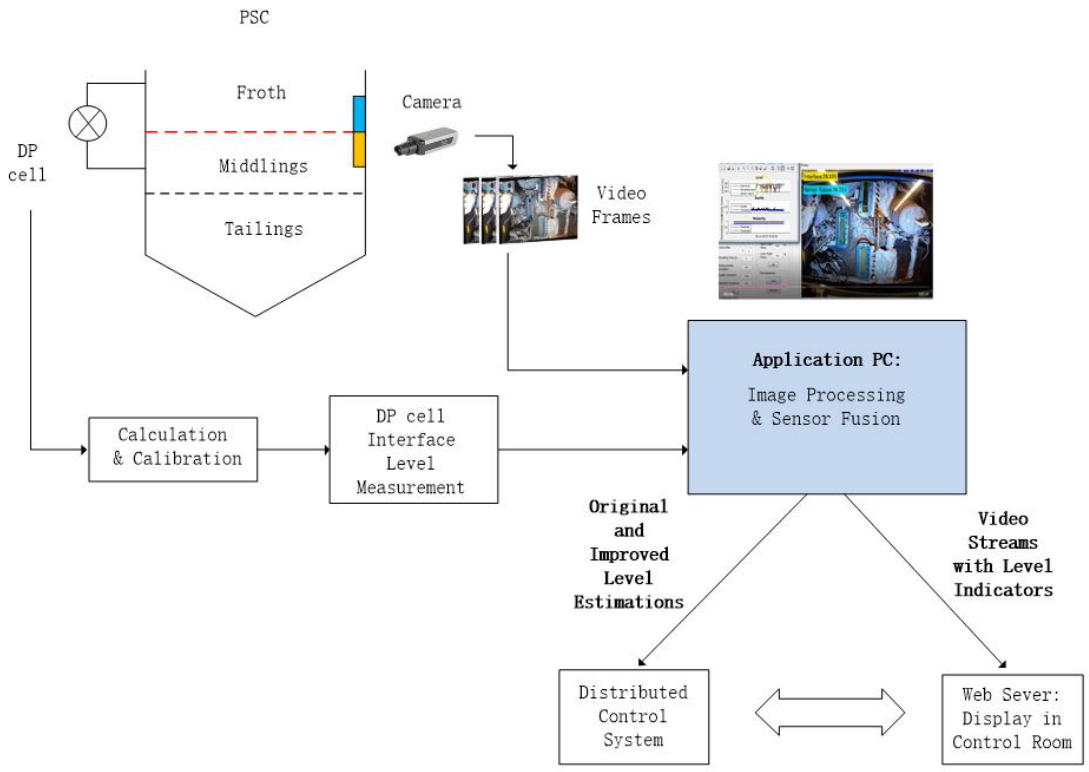

Figure 4.8: The updated implementation architecture of sensor fusion and computer vision integrated system.

versity of Alberta using industrial data. The lab experimental set up is illustrated in

Figure 4.9. The monitor is used to display real industrial sight glass vision videos. The camera is utilized to capture video frames, which are sent to the application computer, where the updated software calculates both original computer vision results and sensor fusion estimation reults of the interface level.

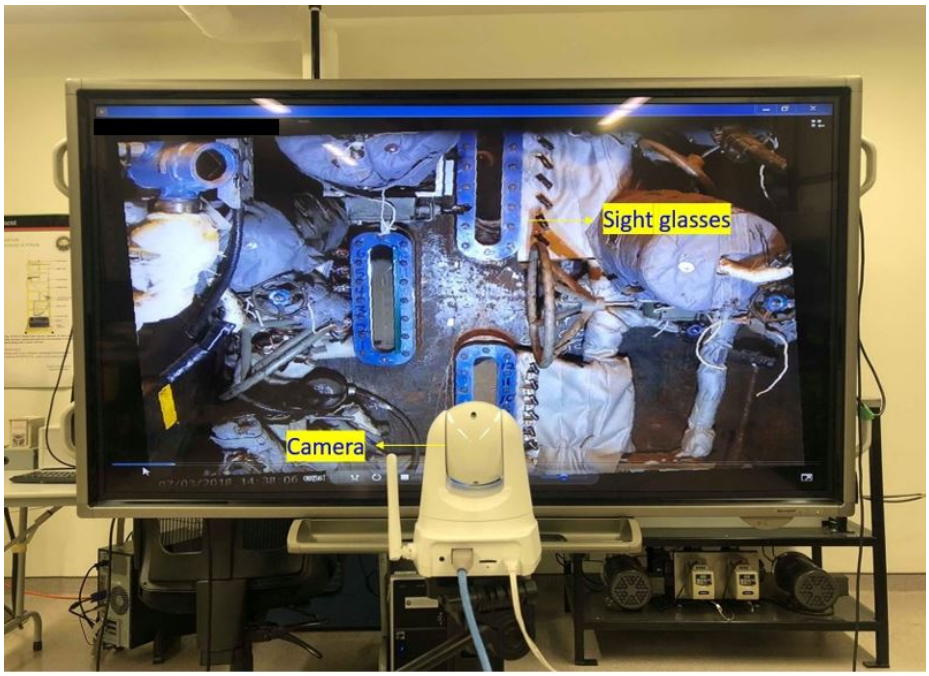

Figure 4.9: Industrial environment simulation setup in the CPC IRC lab at the University of Alberta.

Figure 4.10 shows a two-hour simulation with industrial data. The first subplot shows the original computer vision results, DP cell measurements, and the sensor fusion results. The second and third subplots indicate the corresponding quality and reliability indices of computer vision estimation. The red dashed ellipses indicate the low-quality condition, which is mainly due to interface crossing sight glasses. Over this period, the quality index falls below the threshold for around half an hour, and the computer vision freezes itself by holding on the last reading of the interface. Instead of holding the last reading as computer vision does, the sensor fusion approach uses the latest calibrated fusion parameters as well as DP cell measurements to continuously providing interface level estimation. The corresponding video images are

illustrated in Figure 4.11. From Figure 4.11a to 4.11c, the computer vision results

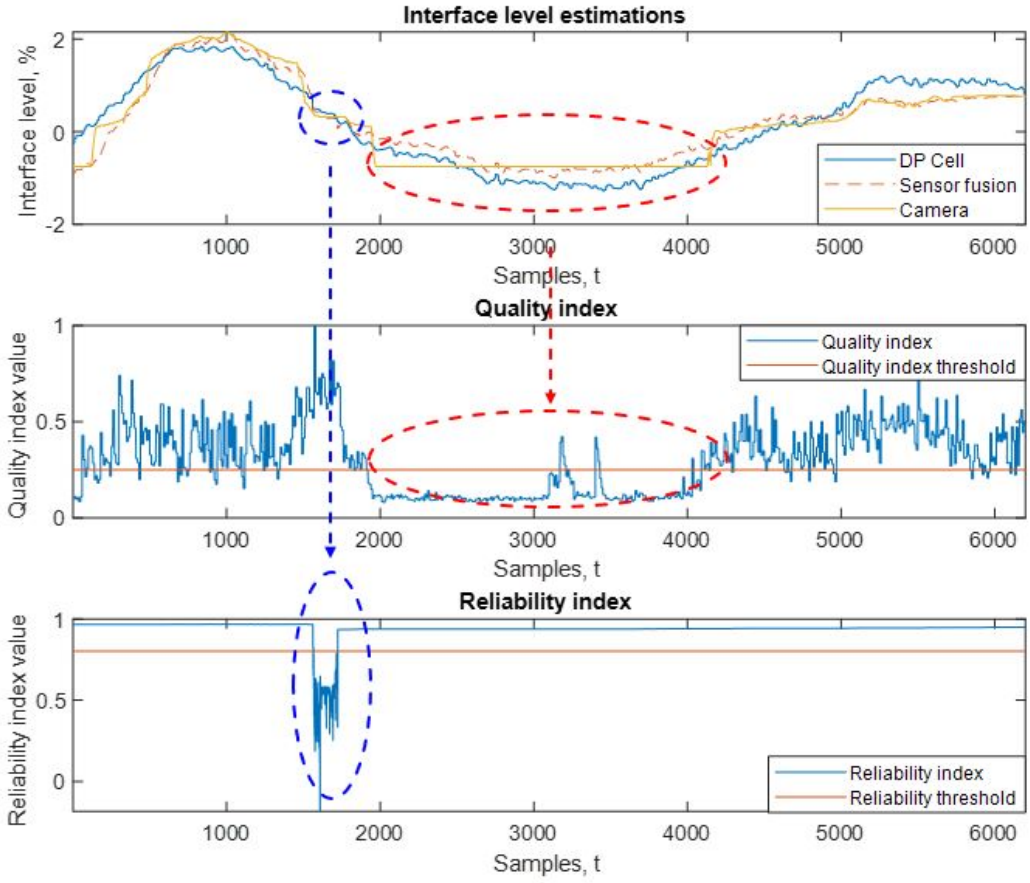

Figure 4.10: Simulation example with sight glass blocking and transition region problems.

keep as a constant, and background color of estimation value becomes yellow, indicating low-quality condition. During this period, the sensor fusion takes over to provide dynamic interface level estimation. In Figure 4.11d, the background color of the computer vision results change back to green, indicating high quality index, and the computer vision estimation becomes reliable again. Then the fusion parameters will start updating according to the reliable computer vision results. In Figure 4.10, the blue dashed ellipse indicates the low-reliability condition, which is caused by maintenance activities. The corresponding scenarios are shown in Figure 4.12. From Figure 4.12a to 4.12d, the operator was doing check and maintenance on the

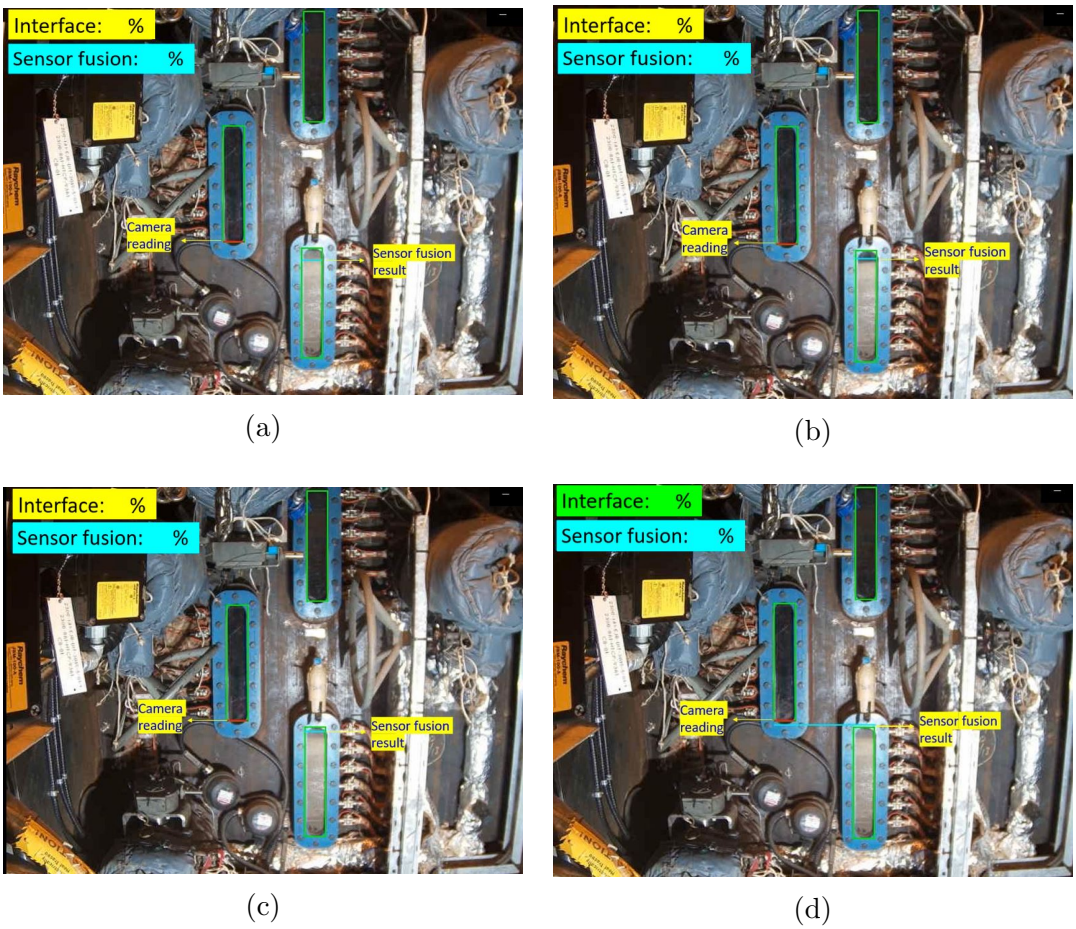

Figure 4.11: Sensor fusion and computer vision integrated system GUI displays under the low-quality (transition region) condition.

PSC, and the sight glass visions are completely or partially blocked. In this case, the camera fails to capture informative images and computer vision system is not able to perform calculations normally. The background color of computer vision results becomes red indicating low-reliability condition and the estimated interface level remains unchanged. Over this period, the sensor fusion continuously providing reliable estimation of interface level.

Another two-hour industrial environment simulation, which corresponds to the sight glass stains, is performed. The result is shown in Figure 4.13, in which the red dashed ellipse marks the low-quality period due to stains on the upper sight glass. The corresponding video images are shown in Figure 4.14. From Figure 4.14a to 4.14d,

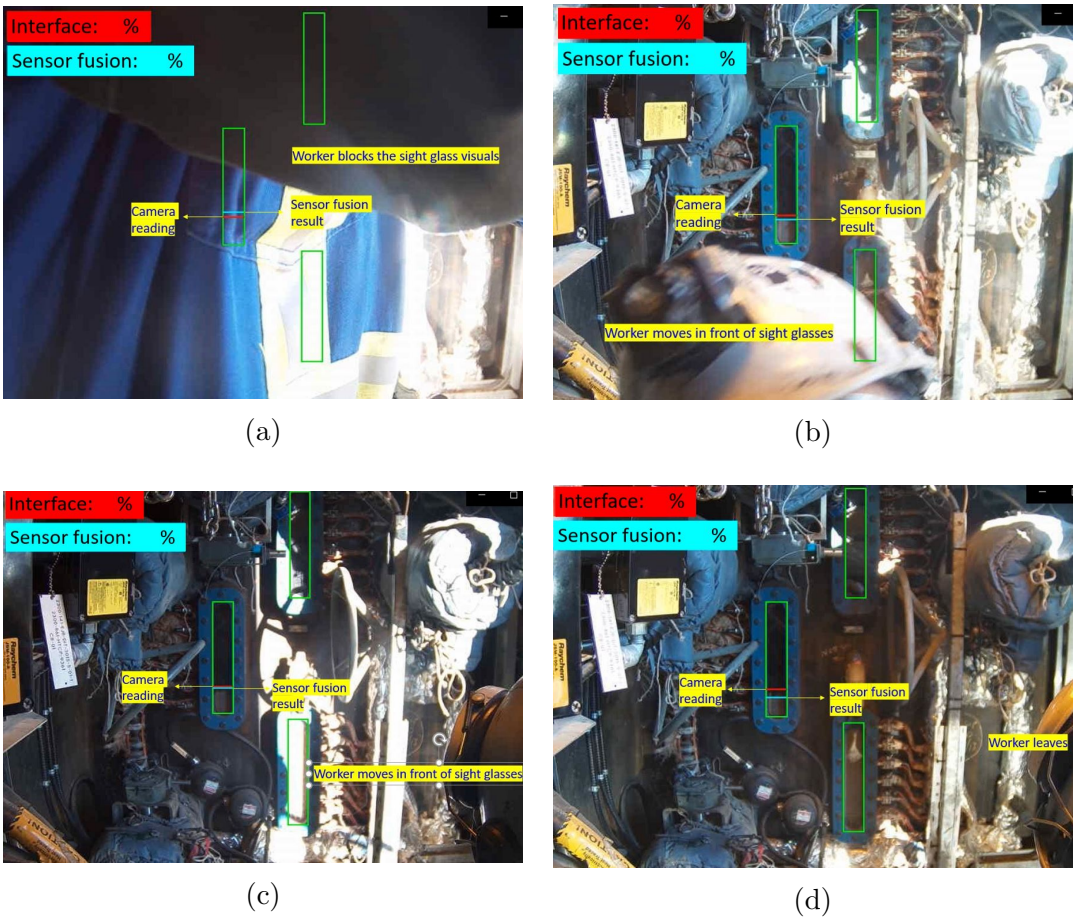

Figure 4.12: Sensor fusion and computer vision integrated system GUI displays under the low-reliability (operator maintenance) condition.

the interface level increases from the middle sight glass to the upper sight glass, where the vision is partially blocked by stains. In this condition, the camera cannot capture clear movement of the interface, and hence gives low-quality indication and result in constant estimation value. However, the sensor fusion results move smoothly across the two sight glasses without being affected by the stains and provide reliable estimation of the interface level.

4.4 Conclusion

A sensor fusion strategy is proposed and integrated with the image processing based computer vision system for froth-middlings interface level estimation. Under normal

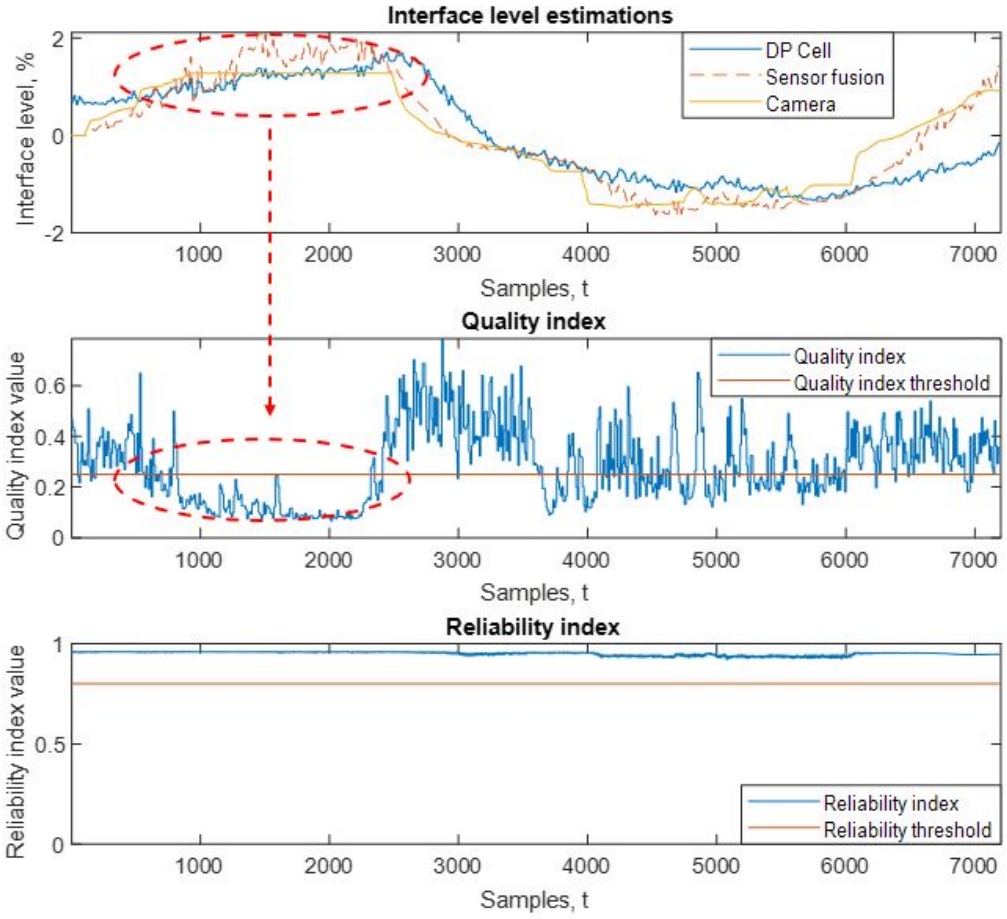

Figure 4.13: Simulation example with sight glass stains.

conditions, the reliable computer vision results are used as references to recursively calibrate the fusion parameters of other sensors. Under abnormal scenarios, instead of freezing interface level estimation, the latest calibrated fusion parameters are used to provide reliable interface level estimation results. Through a number of prediction tests, the sensor fusion results are demonstrated to be reliable alternative estimates in abnormal conditions of computer vision system. The FAT concludes that the sensor fusion and computer vision integrated system is able to provide more robust and reliable interface level estimation.

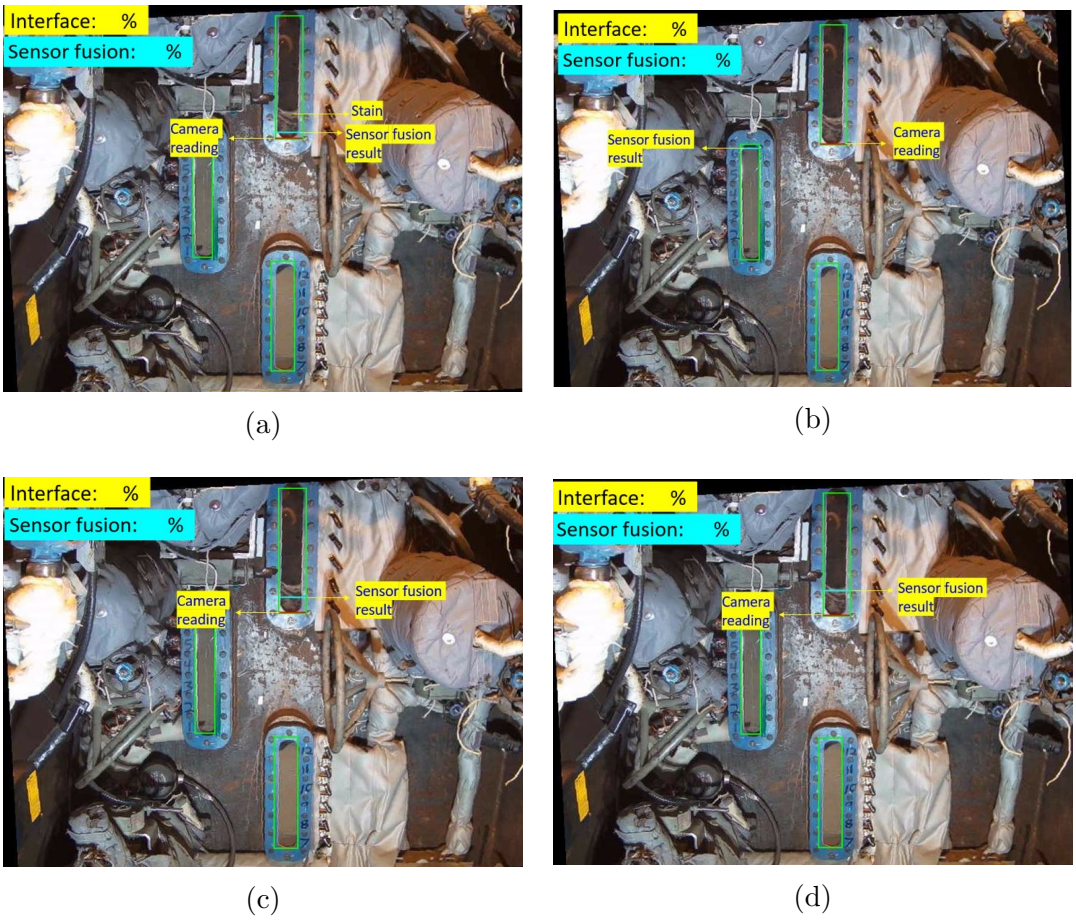

Figure 4.14: Sensor fusion and computer vision integrated system GUI displays under the low-quality (stains) condition.

Chapter 5

Conclusions

5.1 Summary of Thesis

In this thesis, multirate sensor data fusion problem in presence of model inaccuracies and violations of noise assumption is considered. The DNEKF approach is proposed, which utilizes two neural networks to compensate for inadequate process knowledge through simultaneous state and parameter estimations. In the DNEKF, the neural network outputs are used to improve state estimation and output predictions, while the neural network parameters are trained through state vector augmentation. By fusing frequent but less accurate measurements and infrequent but accurate measurements, the DNEKF provides a multirate neural network parameter update strategy to achieve more accurate sensor fusion results. Numerical examples and an industrial case study prove that the DNEKF method is able to compensate for model deficiencies and deviations from noise assumption effectively and provide more reliable fusion results.

Additionally, infrequent measurements are usually sampled irregularly and are available after time-varying time delays. The EKF based parallel fusion that is utilized in the DNEKF is no longer applicable due to measurement time delays. To address irregularity and time-varying time delays while preserving fusion performance, the DNEKF and SNEKF synchronization fusion approach is proposed. In this proposed approach, the DNEKF algorithm is applied to regular frequent estimation to improve

state and output predictions, and the SNEKF is applied to irregular infrequent estimation. The two estimates are then fused in the fusion center when irregular infrequent measurements become available. It is worth noticing that the proposed method does not require to know the delay time in advance. Numerical examples and an industrial case study demonstrate that the proposed synchronization fusion approach provides more reliable state estimation at a frequent sampling rate in presence of model errors, violations of noise assumption, and delayed infrequent measurements.

The froth-middlings interface level of PSC is a critical quality variable to oil sands extraction operation and can be measured in several ways. Among them, the computer vision system, which uses a camera to track interface level through sight glass visions, is considered the most accurate. However, abnormalities such as sight glass vision blocking and sight glass transition regions will prevent the camera from capturing the clear interface level. Under such conditions, the computer vision system will hold the last estimate until clear interface level is tracked again. To solve this problem, a simplified version of sensor fusion approaches, which recursively updates fusion parameters using reliable computer vision results, is proposed for implementation. Industrial environment simulations demonstrate the advantages of the sensor fusion and computer vision integrated system, and the implementation strategy is proved to be effective through FAT.

5.2 Recommendations for Future Work

In this section, a few recommendations about directions that are worthy of future investigation based on current results are listed.

- In Chapter 2, combination of the simple feed-forward neural network and the EKF are made to improve multirate sensor fusion performance. In the future, combinations of the recurrent neural network (RNN) and the convolutional neural network (CNN) with other nonlinear filters such as the unscented Kalman

filter (UKF) and the particle filter (PF) can also be used to further improve fusion accuracy and robustness.

- In chapter 3, random time delays following uniform distributions are considered. Delay with other distributions such as the Poisson distribution and the Dirichlet distribution can be considered for general applications. In addition, the weights and biases of employed neural networks for the DNEKF and the SNEKF are estimated through state vector augmentations. Other parameter estimation methods such as gradient decent can be applied to estimate the neural network parameters as well.

- In chapter 4, the initial industrial implementation test is performed. In the future, profiler and integrated sensor readings can also be imported to the industrial system through OPC to perform a more comprehensive sensor fusion. Finally, after tests, the sensor fusion and computer vision results can be integrated into one single estimate to give a more robust and accurate interface level estimation.

Bibliography

[1] J. J. Wang, J. Wang, D. Sinclair, and L. Watts, "A neural network and kalman filter hybrid approach for gps / ins integration," 2006.

[2] S. C. Stubberud, R. N. Lobbia, and M. Owen, "An adaptive extended kalman filter using artificial neural networks," in *Proceedings of 1995 34th IEEE Conference on Decision and Control*, vol. 2, 1995, 1852–1856 vol.2.

[3] S.-L. Sun and Z.-L. Deng, "Multi-sensor optimal information fusion kalman filter," *Automatica*, vol. 40, no. 6, pp. 1017–1023, 2004.

[4] C. B. Chang and K. P. Dunn, "Kalman filter compensation for a special class of systems," *IEEE Transactions on Aerospace and Electronic Systems*, vol. AES-13, no. 6, pp. 700–706, 1977.

[5] J. Z. Sasiadek and P. Hartana, "Sensor data fusion using kalman filter," in *Proceedings of the Third International Conference on Information Fusion*, vol. 2, 2000, WED5/19–WED5/25 vol.2.

[6] M. Mombeini and H. Khaloozadeh, "State and parameter estimation of the lorenz system in existence of colored noise," *arXiv preprint arXiv:1211.4228*, 2012.

[7] M. A. Akram, P. Liu, M. O. Tahir, W. Ali, and Y. Wang, "A state optimization model based on kalman filtering and robust estimation theory for fusion of multi-source information in highly non-linear systems," *Sensors (Basel, Switzerland)*, vol. 19, 2019.

[8] Shuli Sun, "Multi-sensor optimal information fusion kalman filter for discrete multichannel arma signals," in *Proceedings of the 2003 IEEE International Symposium on Intelligent Control*, 2003, pp. 377–382.

[9] T. H. Xu, Y. P. Chen, and Q. X. Wang, "Kalman filter-based orbit determination with dynamic model compensation for a maneuvered geo satellite," in *Advanced Materials Research*, Trans Tech Publ, vol. 383, 2012, pp. 5626–5631.

[10] J. Sasiadek and P. Hartana, "Sensor data fusion using kalman filter," vol. 2, Aug. 2000, WED5/19 –WED5/25 vol.2, ISBN: 2-7257-0000-0. DOI: 10.1109/IFIC.2000.859866.

[11] K. Lee and E. N. Johnson, "State estimation using gaussian process regression for colored noise systems," in *2017 IEEE Aerospace Conference*, IEEE, 2017, pp. 1–8.

[12] Y. Hao, A. Xu, X. Sui, and Y. Wang, "A modified extended kalman filter for a two-antenna gps/ins vehicular navigation system," *Sensors*, vol. 18, p. 3809, Nov. 2018. DOI: 10.3390/s18113809.

[13] M. Choi, R. Sakthivel, and W. K. Chung, "Neural network-aided extended kalman filter for slam problem," in *Proceedings 2007 IEEE International Conference on Robotics and Automation*, 2007, pp. 1686–1690.

[14] M. W. Owen and A. R. Stubberud, "A neural extended kalman filter multiple model tracker," in *Oceans 2003. Celebrating the Past Teaming Toward the Future (IEEE Cat. No.03CH37492)*, vol. 4, 2003, 2111–2119 Vol.4.

[15] S. C. Stubberud and K. A. Kramer, "A 2-d intercept problem using the neural extended kalman filter for tracking and linear predictions," in *Proceedings of the Thirty-Seventh Southeastern Symposium on System Theory, 2005. SSST '05.*, 2005, pp. 367–372.

[16] K. A. Kramer, S. C. Stubberud, and J. A. Geremia, "Sensor calibration using the neural extended kalman filter in a control loop," pp. 19–24, 2007.

[17] S. C. Stubberud, K. A. Kramer, and J. A. Geremia, "Online sensor modeling using a neural kalman filter," *IEEE Transactions on Instrumentation and Measurement*, vol. 56, no. 4, pp. 1451–1458, 2007.

[18] Dong-Jun Lee and M. Tomizuka, "Multirate optimal state estimation with sensor fusion," in *Proceedings of the 2003 American Control Conference, 2003.*, vol. 4, 2003, 2887–2892 vol.4.

[19] S. Safari, F. Shabani, and D. Simon, "Multirate multisensor data fusion for linear systems using kalman filters and a neural network," *Aerospace Science and Technology*, vol. 39, pp. 465–471, 2014.

[20] M. K. Kalandros, L. Trailovic, L. Y. Pao, and Y. Bar-Shalom, "Tutorial on multisensor management and fusion algorithms for target tracking," in *Proceedings of the 2004 American Control Conference*, vol. 5, 2004, 4734–4748 vol.5.

[21] S. Canan, R. Akkaya, and S. Ergintav, "Extended kalman filter sensor fusion and application to mobile robot," in *Proceedings of the IEEE 12th Signal Processing and Communications Applications Conference, 2004.*, 2004, pp. 771–774.

[22] D. Simon, *Optimal state estimation: Kalman, H Infinity, and Nonlinear Approaches*. John Wiley & Sons, 2006.

[23] N. Shivashankarappa, S. Adiga, R. A. Avinash, and H. R. Janardhan, "Kalman filter based multiple sensor data fusion in systems with time delayed state," in *2016 3rd International Conference on Signal Processing and Integrated Networks (SPIN)*, 2016, pp. 375–382.

[24] A. Gopalakrishnan, N. Kaisare, and S. Narasimhan, "Incorporating delayed and infrequent measurements in extended kalman filter based nonlinear state estimation," *Journal of Process Control*, vol. 21, pp. 119–129, Jan. 2011. DOI: 10.1016/j.jprocont.2010.10.013.

[25] Y. Guo, Y. Zhao, and B. Huang, "Development of soft sensor by incorporating the delayed infrequent and irregular measurements," *Journal of Process Control*, vol. 24, no. 11, pp. 1733–1739, 2014.

[26] B. M. Wilamowski, N. J. Cotton, O. Kaynak, and G. Dundar, "Computing gradient vector and jacobian matrix in arbitrarily connected neural networks," *IEEE Transactions on Industrial Electronics*, vol. 55, no. 10, pp. 3784–3790, 2008.

[27] I. Aizenberg and C. Moraga, "Multi-layered neural network based on multi-valued neurons (mlmvn) and a backpropagation learning algorithm," Jul. 2004. DOI: 10.17877/DE290R-8012.

[28] M. Nielsen, *Neural networks and deep learning*, 2019. [Online]. Available: http://neuralnetworksanddeeplearning.com/.

[29] D. L. Hartmann, *Atm s 552 notes*, 2014. [Online]. Available: https://atmos.washington.edu/~dennis/552_Notes_ftp.html.

[30] Y Tu, J. O'Carroll, L. Kotlyar, B. Sparks, S Ng, K. Chung, and G Cuddy, "Recovery of bitumen from oilsands: Gelation of ultra-fine clay in the primary separation vessel," *Fuel*, vol. 84, no. 6, pp. 653–660, 2005.

[31] B. Li, F. Xu, Z. Ren, and A. Espejo, "Extended abstract: Primary separation vessel interface control," in *2011 International Symposium on Advanced Control of Industrial Processes (ADCONIP)*, 2011, pp. 262–264.

[32] P. Jampana, S. L. Shah, and R. Kadali, "Computer vision based interface level control in separation cells," *Control Engineering Practice*, vol. 18, no. 4, pp. 349–357, 2010.

[33] A. Vicente, R. Raveendran, B. Huang, S. Sedghi, A. Narang, H. Jiang, and W. Mitchell, "Computer vision system for froth-middlings interface level detection in the primary separation vessels," *Computers Chemical Engineering*, vol. 123, Apr. 2019. DOI: 10.1016/j.compchemeng.2019.01.017.

[34] J. Sansana, R. Rendall, Z. Wang, L. Chiang, and M. Reis, "Sensor fusion with irregular sampling and varying measurement delays," *Industrial Engineering Chemistry Research*, Jan. 2020. DOI: 10.1021/acs.iecr.9b05105.

[35] T. Shimada, K. Toda, and K. Nishida, "Real-time parallel architecture for sensor fusion," *Journal of Parallel and Distributed Computing*, vol. 15, no. 2, pp. 143–152, 1992.

[36] Huimin Chen, T. Kirubarajan, and Y. Bar-Shalom, "Performance limits of track-to-track fusion versus centralized estimation: Theory and application [sensor fusion]," *IEEE Transactions on Aerospace and Electronic Systems*, vol. 39, no. 2, pp. 386–400, 2003.

[37] K. H. Kim, "Development of track to track fusion algorithms," in *Proceedings of 1994 American Control Conference - ACC '94*, vol. 1, 1994, 1037–1041 vol.1.

[38] X. Tian and Y. Bar-Shalom, "Track-to-track fusion architectures - a review," 2012.

[39] C. Harris and J. Gao, "Some remarks on kalman filters for the multisensor fusion," 191–201, Aug. 2001.

[40] M. Aeberhard, S. Schlichtharle, N. Kaempchen, and T. Bertram, "Track-to-track fusion with asynchronous sensors using information matrix fusion for surround environment perception," *IEEE Transactions on Intelligent Transportation Systems*, vol. 13, no. 4, pp. 1717–1726, 2012.

[41] Q. Xiangdong and W. Baoshu, "A modified adaptive track fusion approach," in *Proceedings of the Fifth International Conference on Information Fusion. FUSION 2002. (IEEE Cat.No.02EX5997)*, vol. 2, 2002, 1535–1541 vol.2.

[42] T. D. Larsen, N. A. Andersen, O. Ravn, and N. K. Poulsen, "Incorporation of time delayed measurements in a discrete-time kalman filter," in *Proceedings of the 37th IEEE Conference on Decision and Control (Cat. No.98CH36171)*, vol. 4, 1998, 3972–3977 vol.4.

[43] R. Merwe and E. Wan, "Sigma-point kalman filters for probabilistic inference in dynamic state-space models (ph.d. thesis)," *OGI School of Science Engineering, Oregon Health Science University, USA*, pp. 192–206, Jun. 2003.

[44] A. Fatehi and B. Huang, "Kalman filtering approach to multi-rate information fusion in the presence of irregular sampling rate and variable measurement delay," *Journal of Process Control*, vol. 53, pp. 15–25, 2017.

[45] Y. Zhu, J. Zhou, X. Shen, E. Song, and Y. Luo, *Networked multisensor decision and estimation fusion: based on advanced mathematical methods*. CRC Press, 2012, pp. 191–209.

[46] H. R. Hashemipour, S. Roy, and A. J. Laub, "Decentralized structures for parallel kalman filtering," *IEEE Transactions on Automatic Control*, vol. 33, no. 1, pp. 88–94, 1988.

[47] *Oil sands magazine*, 2019. [Online]. Available: https://www.oilsandsmagazine.com/news/2019/3/5/cenovus-bets-on-partial-upgrading-fractal-systems-pipeline-constraints?rq=dilbit.

[48] J. Chea, A. Lehr, J. Stengel, M. Savelski, C. S. Slater, and K. Yenkie, "Evaluation of solvent recovery options for economic feasibility through a superstructure-based optimization framework," *Industrial Engineering Chemistry Research*, Mar. 2020. DOI: 10.1021/acs.iecr.9b06725.

[49] *Oil sands magazine*, 2018. [Online]. Available: https://www.oilsandsmagazine.com/technical/mining/extraction/psc-primary-separation-cell.

[50] R. T. Behrens and L. L. Scharf, "Signal processing applications of oblique projection operators," *IEEE Transactions on Signal Processing*, vol. 42, no. 6, pp. 1413–1424, 1994.

[51] R. Szeliski, *Computer vision: algorithms and applications*. Springer Science & Business Media, 2010.

[52] K. J. Pithadiya, C. K. Modi, and J. D. Chauhan, "Comparison of optimal edge detection algorithms for liquid level inspection in bottles," in *2009 Second International Conference on Emerging Trends in Engineering & Technology*, IEEE, 2009, pp. 447–452.

[53] T. F. Edgar, *Recursive least squares parameter estimation for linear steady state and dynamic models*, 2010.

[54] J. Fox, *Applied regression analysis and generalized linear models*. Sage Publications, 2015.

[55] C. Paleologu, J. Benesty, and S. Ciochina, "A robust variable forgetting factor recursive least-squares algorithm for system identification," *IEEE Signal Processing Letters*, vol. 15, pp. 597–600, 2008.

[56] G. C. Goodwin and K. S. Sin, *Adaptive filtering prediction and control*. Courier Corporation, 2014.